

INVESTIGATING THE EFFECTS OF NANOSTRUCTURED DIELECTRIC LITHIUM
FLUORIDE AND PLASMONIC GOLD INTERLAYERS IN ORGANIC
PHOTOVOLTAICS, INCLUDING THE USE OF *IN-SITU* IMPEDANCE
SPECTROSCOPY

by

HASAN KURT

Submitted to the Graduate School of Engineering and Natural Sciences
in partial fulfillment of
the requirements for the degree of
Doctor of Philosophy

Sabancı University

Spring 2016

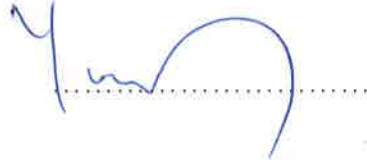
INVESTIGATING THE EFFECTS OF NANOSTRUCTURED DIELECTRIC LITHIUM
FLUORIDE AND PLASMONIC GOLD INTERLAYERS IN ORGANIC
PHOTOVOLTAICS, INCLUDING THE USE OF *IN-SITU* IMPEDANCE
SPECTROSCOPY

APPROVED BY:

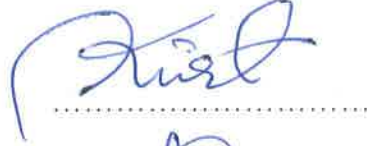
Assoc. Prof. Cleva W. Ow-Yang
(Dissertation Supervisor)



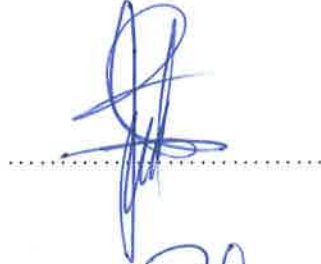
Prof. Yusuf Z. Menceloğlu
(Jury Member)



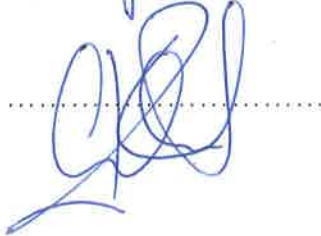
Assoc. Prof. Kürşat Şendur
(Jury Member)



Prof. Mustafa M. Demir
(Jury Member)



Asst. Prof. Çınar Öncel
(Jury Member)



DATE OF APPROVAL: 01.08.2016

© Hasan Kurt 2016

All Rights Reserved

Abstract

INVESTIGATING THE EFFECTS OF NANOSTRUCTURED DIELECTRIC LITHIUM FLUORIDE AND PLASMONIC GOLD INTERLAYERS IN ORGANIC PHOTOVOLTAICS, INCLUDING THE USE OF *IN-SITU* IMPEDANCE SPECTROSCOPY

HASAN KURT

PhD Dissertation, August 2016

Dissertation Supervisor: Assoc. Prof. Clewa W. Ow-Yang

Keywords: organic photovoltaics, interface engineering, impedance spectroscopy, charge carrier dynamics, functional interfaces, plasmonic field enhancement

Organic solar cell performance can be limited by the problematic organic-inorganic interfaces between the active layer and the electrodes. One solution is the incorporation of nanostructured functional interlayers, which enable additional engineering control of these interfaces to improve photovoltaic performance. Herein we demonstrated that solution-processed dielectric LiF (sol-LiF) and plasmonic Au (sol-Au) nanostructuring on the indium tin oxide (ITO) anode can be used to improve bulk heterojunction (BHJ) organic photovoltaic (OPV) device performance. We show that the surface work function of ITO thin film anodes can be tuned via the areal density of sol-LiF nanoparticles and enables the optimization of energy level alignment between the organic layers and ITO. In addition, we show that the electric field component of incident light is strongly enhanced at the edges of sol-Au nanoparticles, due to the excitation of localized surface plasmon resonances

(LSPR). When incorporated into BHJ OPV devices, these sol-Au nanoparticles improved the efficiency of BHJ absorption by acting like antennas, enhancing charge carrier generation. Each of these interlayer types contribute to increased photocurrent generation. In order to distinguish the root cause of improvement, impedance spectroscopy (IS) analysis was applied to the modified OPVs *in-operando*. In the case of sol-LiF, more favorable energy level alignment engenders better charge collection. In the case of sol-Au, the improved charge generation rate occurs without perturbing the carrier extraction. Thus instead of tracking the multivariate OPV device characteristics, IS enables more detailed analysis of the underlying operating mechanisms to elucidate the specific contributions of nanostructured interlayers.

Özet

NANOYAPILANDIRILMIŞ DİELEKTRİK LİTYUM FLURÜR VE PLAZMONİK
ALTIN ARATABAKALARIN ORGANİK FOTOVOLTAİKLER ÜZERİNDEKİ
ETKİLERİNİN İN-SİTU İMPEDANS SPEKTROSKOPİSİ DE DAHİL İNCELENMESİ

HASAN KURT

Doktora Tezi, Ağustos 2016

Tez Danışmanı: Doç. Dr. Clewa W. Ow-Yang

Anahtar Kelimeler: organic fotovoltaiik, arayüzey mühendisliđi, impedans spektroskopisi, yük taşıyıcı dinamikleri, fonksiyonel yüzeyler, plazmonik alan arttırılması

Organik güneş hücrelerinin verimleri, aktif tabaka ve elektrotlar arasında yer alan organik-inorganik ara tabakadaki sorunlar nedeniyle kısıtlıdır. Bu ara tabakalara, nano ölçekte yapılandırılmış fonksiyonel ara tabakaların entegrasyonu fotovoltaiik verimin arttırılmasına yönelik bir çözüm sunmaktadır. Sunulan çalışmada, solüsyon prosesli dielektrik LiF (sol-LiF) ve plazmonik altın (sol-Au) nanoyapılarla dekore edilmiş indiyum kalay oksit (İTO) anot yüzeylerin, “bulk heteroeklem” (BHJ) tipi organik fotovoltaiiklerin (OPV) performansını arttırdığı görülmüştür. İnce film İTO anotun yüzey iş fonksiyonunun, organik tabakalar ile İTO anot arasındaki enerji düzeyi uyumunu iyileştirmeye olanak sağlayacak şekilde, sol-LiF nanoparçacıklarının yüzeyde kapladığı alana bađlı olarak kontrollü bir şekilde ayarlanabildiđi gözlemlenmiştir. Bunlara ilaveten; gelen ışığın elektrik alan komponenti, lokalize yüzey plazmon rezonansların (LSPR) uyarılması sebebiyle sol-Au nanoparçacıkların kenarlarında güçlü bir şekilde yoğunlaşmıştır. Bu ara tabakalar BHJ OPV güneş hücrelerine entegre edildiklerinde, sol-Au nanoparçacıklar anten

gibi davranarak BHJ'nin ışık emilimini arttırmış ve bu suretle yük taşıyıcıların oluşturulmasını güçlendirmiştir.

Sonuç olarak kullanılan her iki çeşit nanaoparçacık ara tabakası da, fotoakım üretiminin artmasına katkıda bulunmuştur. Bu artışın altında yatan nedenleri araştırmak üzere, nanoyapılandırılmış anotlara sahip OPV güneş hücreleri çalışır durumda iken, impedans spektroskopisi (IS) kullanılarak analiz edilmişlerdir. Elde edilen bulgulara göre; sol-LiF nanoparçacıklar enerji düzeyi uyumunun iyileştirilmesi sayesinde yük toplama verimini arttırmışlardır. Sol-Au nanoparçacıkların ise, yük toplama proseslerini etkilemeden yük oluşum verimini yükselttikleri görülmüştür. IS çalışmaları; çok değişkenli OPV aygıt karakteristikleri yerine, kullanılan spesifik nano yüzeylerden kaynaklı performans artışının altında yatan mekanizmaların detaylı bir şekilde tanımlanmasına olanak sağlamıştır.

Acknowledgements

Firstly, I would like to express my deepest gratitude to my thesis advisor Prof. Cleva W. Ow-Yang for the continuous support of my academic career and scientific research, for her bottomless patience, motivation, and wisdom. Since I started working in her lab in Summer of 2003, she enabled me to pursue my scientific curiosity without any restrictions. Her support helped me in all the time of research and writing of this thesis. I could not have imagined having a better advisor and mentor for my Ph.D study.

Besides my advisor, I would like to thank the rest of my thesis committee: Prof. Yusuf Z. Mencelođlu, Assoc. Prof. Kürşat Şendur, Prof. Mustafa M. Demir and Assist. Prof. Çınar Öncel for their insightful comments, but also for the intriguing questions which motivated me to diversify my research field with even broader perspective. Even though he was not officially in my thesis committee, I would like to express my sincere gratitude to Prof. Mehmet Ali Gülgün for insightful courses and unique perspectives.

Also I would like to thank other professors of materials science and engineering department; Prof. Canan Atılgan, Assist. Prof. Melih Papila, Prof. Mehmet Yıldız, Prof. Yuda Yürüm; for their contributions to my scientific education.

Also, I would like to thank Asst. Prof. Dr. Cem Öztürk for his insightful classes on semiconductors and microfabrication, Prof. Cihan Saçlıođlu for providing me an excellent physics education, Assoc. Prof. Kürşat Şendur for his deep knowledge in nano-optics and finally Asst. Prof. Ayşe Turak for directing me to organic photovoltaics and support in the problems I faced during my thesis work.

Furthermore, I would like to thank Dr. Meral Yüce for introducing biotechnology into my scientific repertoire and our fruitful collaborative work on nanobiotechnology.

I also would like to thank Melike Mercan Yıldızhan, Mustafa Baysal, Dr. Güliz İnan, and rest of my graduate student friends for their friendship and support.

I would like to acknowledge the support of the Scientific and Technological Research Council of Turkey (TÜBİTAK) for BİDEB 2211A fellowship.

Finally, I would like to express my sincerest gratitude to my family for their eternal support.

Table of Contents

Abstract.....	iv
Acknowledgements.....	iv
List of Figures.....	xi
List of Tables.....	xxiv
List of Abbreviations.....	xxvi
List of Symbols and Notations.....	xxviii
Chapter 1: Introduction.....	1
Chapter 2: Nanostructured Indium Tin Oxide Transparent Conductors.....	4
2.1. Introduction.....	4
2.2. Experimental.....	5
2.2.1. Materials.....	5
2.2.2. Synthesis of Lithium Fluoride Nanoparticles in PS-b-P2VP copolymer.....	6
2.2.3. Synthesis of Gold Nanoparticles in PS-b-P2VP and PS-b-P4VP copolymers.....	7
2.2.4. Deposition of sol-LiF and sol-Au and etching of polymeric micelles.....	8
2.2.5. Finite Difference Time Domain (FDTD) Simulations.....	10
2.3. Results.....	13
2.3.1. SEM micrographs and image analysis.....	13
2.3.2. AFM images and image analysis.....	18
2.3.3. PESA measurements of sol-LiF modified ITO surfaces.....	24
2.3.4. Sheet resistance measurements of sol-LiF and sol-Au modified ITO surfaces.....	28
2.3.5. Contact angle measurements of sol-LiF and sol-Au modified ITO surfaces.....	29
2.3.6. FDTD Simulations of sol-Au nanostructures.....	31
2.4. Discussion.....	35
2.5. Summary and Concluding Remarks.....	37
Chapter 3: Incorporation of Nanostructured ITO Electrodes into Organic Photovoltaics.....	39
3.1. Introduction.....	39
3.2. Experimental.....	41

3.2.1 Materials.....	41
3.2.2. Fabrication and device characterization of P3HT:PC ₆₀ BM solar cells	43
3.2.3. Fabrication and device characterization of PCDTBT:PC ₇₀ BM Solar Cells	44
3.2.4. FDTD Simulations of P3HT:PC ₆₀ BM and PCDTBT:PC ₇₀ BM Solar Cells: with and without sol-Au interlayers.....	45
3.3. Results	49
3.3.1. P3HT:PC ₆₀ BM and PCDTBT:PC ₇₀ BM BHJ OPV devices with and without sol-Au interlayers.....	49
3.3.2. P3HT:PC ₆₀ BM and PCDTBT:PC ₇₀ BM BHJ OPV devices with and without sol-LiF interlayers.....	54
3.4. Discussion	62
3.5. Conclusion.....	65
Chapter 4: Impedance Spectroscopy of OPVs with nanostructured interlayers.....	67
4.1. Introduction	67
4.2. Experimental	72
4.3. Results & Discussion	73
4.3.1. Recombination Lifetime.....	75
4.3.2. Charge Carrier Density	80
4.3.3. Recombination Rate and Order	81
4.3.4. Charge Transport Kinetics and Mobility.....	83
4.3.5. Charge Recombination Probability	86
4.4. Conclusion.....	88
Chapter 5: Summary	90
References.....	92
Appendix.....	97
VITA	114

List of Figures

Figure 1. Poly(styrene-b-2-vinyl pyridine) copolymer.....	5
Figure 2. Poly(styrene-b-4-vinyl pyridine) copolymer.....	5
Figure 3. Loading and reduction of LiOH and H ₂ AuCl ₄ in diblock copolymer micelles. ^[31] Reprinted from <i>Thin Solid Films</i> , 559, Ow-Yang, C.W., Jia, J., Aytun, T., Zamboni, M., Turak, A., Saritas, K., and Shigesato Y. Work function tuning of tin-doped indium oxide electrodes with solution-processed lithium fluoride, 58–63, Copyright 2014, with permission from Elsevier.	7
Figure 4. Deposition and etching of loaded micelles on surfaces. ^[31] Reprinted from <i>Thin Solid Films</i> , 559, Ow-Yang, C.W., Jia, J., Aytun, T., Zamboni, M., Turak, A., Saritas, K., & Shigesato Y. Work function tuning of tin-doped indium oxide electrodes with solution- processed lithium fluoride, 58–63, Copyright 2014, with permission from Elsevier.....	8
Figure 5. Etching of polymeric micelles. ^[29] Reprinted with permission from Aytun, T., Turak, A., Baikie, I., Halek, G. & Ow-Yang, C. W. <i>Nano Lett.</i> 12, 39–44 (2012). Copyright 2012 American Chemical Society.	9
Figure 6. Growth of gold precursor loaded polymeric micelles. The scale bar represents length of 30 nm. Adapted with permission from Aytun, T., Turak, A., Baikie, I., Halek, G. & Ow-Yang, C. W. <i>Nano Lett.</i> 12, 39–44 (2012). Copyright 2012 American Chemical Society.	10
Figure 7. The FDTD model of gold used in the study.	11
Figure 8. FDTD model of the gold hemisphere array in vacuum. The excitation source was placed beneath the base of the sol-Au hemispheres, simulating the illumination configuration of the nanostructured OPVs. The propagation direction of excitation is indicated by the magenta arrow. The polarization of the excitation is represented by the blue arrows.....	12
Figure 9. FDTD model of the gold hemisphere array on soda lime glass (teal-colored layer). The excitation source was position at the base of the sol-Au hemispheres. The propagation direction of excitation is indicated by the purple arrow. The polarization of the excitation is represented by the blue arrows.	12

Figure 10. Raw and processed SEM micrograph of 1x sol-LiF deposition, 2% surface coverage.^[37] The scale bar represents 200 nm. Reprinted from *J. Mater. Sci. Mater. Electron.* Tuning hole charge collection efficiency in polymer photovoltaics by optimizing the work function of indium tin oxide electrodes with solution-processed LiF nanoparticles 2015, 9205–9212, Kurt, H., Jia, J., Shigesato, Y. & Ow-Yang, C. W. with permission of Springer.....13

Figure 11. Raw and processed SEM micrograph of 1x sol-LiF deposition, 5.6% surface coverage.^[37] The scale bar represents 200 nm. Reprinted from *J. Mater. Sci. Mater. Electron.* Tuning hole charge collection efficiency in polymer photovoltaics by optimizing the work function of indium tin oxide electrodes with solution-processed LiF nanoparticles 2015, 9205–9212, Kurt, H., Jia, J., Shigesato, Y. & Ow-Yang, C. W. with permission of Springer.....13

Figure 12. Raw and processed SEM micrograph of 5x sol-LiF deposition, 8.7% surface coverage.^[37] The scale bar represents 200 nm. Reprinted from *J. Mater. Sci. Mater. Electron.* Tuning hole charge collection efficiency in polymer photovoltaics by optimizing the work function of indium tin oxide electrodes with solution-processed LiF nanoparticles 2015, 9205–9212, Kurt, H., Jia, J., Shigesato, Y. & Ow-Yang, C. W. with permission of Springer.....14

Figure 13. Raw and processed SEM micrograph of 7x sol-LiF deposition, 10.1% surface coverage.^[37] The scale bar represents 200 nm. Reprinted from *J. Mater. Sci. Mater. Electron.* Tuning hole charge collection efficiency in polymer photovoltaics by optimizing the work function of indium tin oxide electrodes with solution-processed LiF nanoparticles 2015, 9205–9212, Kurt, H., Jia, J., Shigesato, Y. & Ow-Yang, C. W. with permission of Springer.....14

Figure 14. Raw and processed SEM micrograph of 10x sol-LiF deposition, 13.2% surface coverage.^[37] The scale bar represents 200 nm. Reprinted from *J. Mater. Sci. Mater. Electron.* Tuning hole charge collection efficiency in polymer photovoltaics by optimizing the work function of indium tin oxide electrodes with solution-processed LiF nanoparticles 2015, 9205–9212, Kurt, H., Jia, J., Shigesato, Y. & Ow-Yang, C. W. with permission of Springer.....15

Figure 15. Single deposition, sol-LiF nanoparticle size histogram (a), normalized autocorrelation function between centers of the sol-LiF nanoparticles (b), normalized radial distribution function of sol-LiF nanoparticles (c). Reprinted from *J. Mater. Sci. Mater. Electron.* Tuning hole charge collection efficiency in polymer photovoltaics by optimizing the work function of indium tin oxide electrodes with solution-processed LiF nanoparticles 2015, 9205–9212, Kurt, H., Jia, J., Shigesato, Y. & Ow-Yang, C. W. with permission of Springer.....15

Figure 16. Number of sequential spin-coating versus LiF surface coverage. Reproduced from *J. Mater. Sci. Mater. Electron.* Tuning hole charge collection efficiency in polymer photovoltaics by optimizing the work function of indium tin oxide electrodes with solution-processed LiF nanoparticles 2015, 9205–9212, Kurt, H., Jia, J., Shigesato, Y. & Ow-Yang, C. W. with permission of Springer.16

Figure 17. SEM micrographs of sol-Au nanoparticles on Si wafer (left) and sol-Au nanoparticles on ITO coated glass (right) after a single deposition. The scale bar represents 200 nm. H. Kurt & C.W. Ow-Yang, Impedance Spectroscopy Analysis of the photophysical dynamics due to the nanostructuring of anode interlayers in organic photovoltaics. *Physica Status Solidi A*. Copyright Wiley-VCH Verlag GmbH & Co. KGaA. Reproduced with permission.17

Figure 18. Single deposition, sol-Au nanoparticle size histogram (a), normalized autocorrelation function between centers of the sol-Au nanoparticles (b), normalized radial distribution function of sol-Au nanoparticles (c).....17

Figure 19. AFM line profile of bare ITO substrate. Reprinted from *J. Mater. Sci. Mater. Electron.* Tuning hole charge collection efficiency in polymer photovoltaics by optimizing the work function of indium tin oxide electrodes with solution-processed LiF nanoparticles 2015, 9205–9212, Kurt, H., Jia, J., Shigesato, Y. & Ow-Yang, C. W. with permission of Springer.....18

Figure 20. 3D AFM image of 1x sol-LiF deposition on ITO, with 2% surface coverage. Reprinted from *J. Mater. Sci. Mater. Electron.* Tuning hole charge collection efficiency in polymer photovoltaics by optimizing the work function of indium tin oxide electrodes with solution-processed LiF nanoparticles 2015, 9205–9212, Kurt, H., Jia, J., Shigesato, Y. & Ow-Yang, C. W. with permission of Springer.18

Figure 21. AFM line profile of 1x sol-LiF deposition on ITO, with 2% surface coverage. Reprinted from *J. Mater. Sci. Mater. Electron.* Tuning hole charge collection efficiency in polymer photovoltaics by optimizing the work function of indium tin oxide electrodes with solution-processed LiF nanoparticles 2015, 9205–9212, Kurt, H., Jia, J., Shigesato, Y. & Ow-Yang, C. W. with permission of Springer.19

Figure 22. 3D AFM image of 3x sol-LiF deposition on ITO, with 5.6% surface coverage. Reprinted from *J. Mater. Sci. Mater. Electron.* Tuning hole charge collection efficiency in polymer photovoltaics by optimizing the work function of indium tin oxide electrodes with solution-processed LiF nanoparticles 2015, 9205–9212, Kurt, H., Jia, J., Shigesato, Y. & Ow-Yang, C. W. with permission of Springer.19

Figure 23. AFM line profile of 3x sol-LiF deposition on ITO, with 5.6% surface coverage. Reprinted from *J. Mater. Sci. Mater. Electron.* Tuning hole charge collection efficiency in polymer photovoltaics by optimizing the work function of indium tin oxide electrodes with solution-processed LiF nanoparticles 2015, 9205–9212, Kurt, H., Jia, J., Shigesato, Y. & Ow-Yang, C. W. with permission of Springer.20

Figure 24. 3D AFM image of 5x sol-LiF deposition on ITO, with 8.7% surface coverage. Reprinted from *J. Mater. Sci. Mater. Electron.* Tuning hole charge collection efficiency in polymer photovoltaics by optimizing the work function of indium tin oxide electrodes with solution-processed LiF nanoparticles 2015, 9205–9212, Kurt, H., Jia, J., Shigesato, Y. & Ow-Yang, C. W. with permission of Springer.20

Figure 25. AFM line profile of 5x sol-LiF deposition on ITO, with 8.7% surface coverage. Reprinted from *J. Mater. Sci. Mater. Electron.* Tuning hole charge collection efficiency in polymer photovoltaics by optimizing the work function of indium tin oxide electrodes with solution-processed LiF nanoparticles 2015, 9205–9212, Kurt, H., Jia, J., Shigesato, Y. & Ow-Yang, C. W. with permission of Springer.21

Figure 26. 3D AFM image of 7x sol-LiF deposition on ITO, with 10.1% surface coverage. Reprinted from *J. Mater. Sci. Mater. Electron.* Tuning hole charge collection efficiency in polymer photovoltaics by optimizing the work function of indium tin oxide electrodes with solution-processed LiF nanoparticles 2015, 9205–9212, Kurt, H., Jia, J., Shigesato, Y. & Ow-Yang, C. W. with permission of Springer.21

Figure 27. AFM line profile of 7x sol-LiF deposition on ITO, with 10.1% surface coverage. Reprinted from <i>J. Mater. Sci. Mater. Electron.</i> Tuning hole charge collection efficiency in polymer photovoltaics by optimizing the work function of indium tin oxide electrodes with solution-processed LiF nanoparticles 2015, 9205–9212, Kurt, H., Jia, J., Shigesato, Y. & Ow-Yang, C. W. with permission of Springer.	22
Figure 28. 3D AFM image of 10x sol-LiF deposition on ITO, with 13.2% surface coverage. Reprinted from <i>J. Mater. Sci. Mater. Electron.</i> Tuning hole charge collection efficiency in polymer photovoltaics by optimizing the work function of indium tin oxide electrodes with solution-processed LiF nanoparticles 2015, 9205–9212, Kurt, H., Jia, J., Shigesato, Y. & Ow-Yang, C. W. with permission of Springer.	22
Figure 29. AFM line profile of 10x sol-LiF deposition on ITO, with 13.2% surface coverage. Reprinted from <i>J. Mater. Sci. Mater. Electron.</i> Tuning hole charge collection efficiency in polymer photovoltaics by optimizing the work function of indium tin oxide electrodes with solution-processed LiF nanoparticles 2015, 9205–9212, Kurt, H., Jia, J., Shigesato, Y. & Ow-Yang, C. W. with permission of Springer.	23
Figure 30. RMS Roughness of the sol-LiF modified ITO-coated glass versus the number of sequential spin-coating of sol-LiF dispersion. Reproduced from <i>J. Mater. Sci. Mater. Electron.</i> Tuning hole charge collection efficiency in polymer photovoltaics by optimizing the work function of indium tin oxide electrodes with solution-processed LiF nanoparticles 2015, 9205–9212, Kurt, H., Jia, J., Shigesato, Y. & Ow-Yang, C. W. with permission of Springer.	23
Figure 31. AFM image of sol-Au deposition on Si.	24
Figure 32. Photoelectron emission yield vs energy diagram for bare ITO surface. Reproduced from <i>J. Mater. Sci. Mater. Electron.</i> Tuning hole charge collection efficiency in polymer photovoltaics by optimizing the work function of indium tin oxide electrodes with solution-processed LiF nanoparticles 2015, 9205–9212, Kurt, H., Jia, J., Shigesato, Y. & Ow-Yang, C. W. with permission of Springer.	25
Figure 33. Photoelectron emission yield vs energy diagram for 1x sol-LiF (2% surface coverage) modified ITO surface. Reproduced from <i>J. Mater. Sci. Mater. Electron.</i> Tuning hole charge collection efficiency in polymer photovoltaics by optimizing the work function	25

of indium tin oxide electrodes with solution-processed LiF nanoparticles 2015, 9205–9212, Kurt, H., Jia, J., Shigesato, Y. & Ow-Yang, C. W. with permission of Springer.....	26
Figure 34. Photoelectron emission yield vs energy diagram for 3x sol-LiF (5.6% surface coverage) modified ITO surface. Reproduced from <i>J. Mater. Sci. Mater. Electron.</i> Tuning hole charge collection efficiency in polymer photovoltaics by optimizing the work function of indium tin oxide electrodes with solution-processed LiF nanoparticles 2015, 9205–9212, Kurt, H., Jia, J., Shigesato, Y. & Ow-Yang, C. W. with permission of Springer.....	26
Figure 35. Photoelectron emission yield vs energy diagram for 5x sol-LiF (8.7% surface coverage) modified ITO surface. Reproduced from <i>J. Mater. Sci. Mater. Electron.</i> Tuning hole charge collection efficiency in polymer photovoltaics by optimizing the work function of indium tin oxide electrodes with solution-processed LiF nanoparticles 2015, 9205–9212, Kurt, H., Jia, J., Shigesato, Y. & Ow-Yang, C. W. with permission of Springer.....	27
Figure 36. Photoelectron emission yield vs energy diagram for 7x sol-LiF (10.1% surface coverage) modified ITO surface. Reproduced from <i>J. Mater. Sci. Mater. Electron.</i> Tuning hole charge collection efficiency in polymer photovoltaics by optimizing the work function of indium tin oxide electrodes with solution-processed LiF nanoparticles 2015, 9205–9212, Kurt, H., Jia, J., Shigesato, Y. & Ow-Yang, C. W. with permission of Springer.....	27
Figure 37. Photoelectron emission yield vs energy diagram for 10x sol-LiF (13.2% surface coverage) modified ITO surface. Reproduced from <i>J. Mater. Sci. Mater. Electron.</i> Tuning hole charge collection efficiency in polymer photovoltaics by optimizing the work function of indium tin oxide electrodes with solution-processed LiF nanoparticles 2015, 9205–9212, Kurt, H., Jia, J., Shigesato, Y. & Ow-Yang, C. W. with permission of Springer.....	28
Figure 38. Electric field intensity, $ E $, profile of sol-Au nanoparticle array at $x = 0$ (1 st column), $y = 0$ (2 nd column) and $z = -5$ planes (3 rd column) under p -polarized (1 st row), s -polarized (2 nd row) and unpolarized (3 rd row) 532 nm plane wave illumination in vacuum.	32
Figure 39. Extinction cross section, Q_{ext} , profile of sol-Au nanoparticle array under s -polarized (left), p -polarized (middle) and unpolarized (right) plane wave illumination in vacuum.....	32
Figure 40. Electric field intensity, $ E $, profile of sol-Au nanoparticle array at $x = 0$ (1 st column), $y = 0$ (2 nd column) and $z = -5$ planes (3 rd column) under p -polarized (1 st row), s -	

polarized (2 nd row) and unpolarized (3 rd row) 532 nm plane wave illumination on soda-lime glass.	33
Figure 41. Extinction cross section, Q_{ext} , profile of sol-Au nanoparticle array under <i>s</i> -polarized (left), <i>p</i> -polarized (middle) and unpolarized (right) plane wave illumination on soda-lime glass substrate.	34
Figure 42. Absorption spectra showing the sol-Au nanoparticle response on soda lime glass substrate. H. Kurt & C.W. Ow-Yang, Impedance Spectroscopy Analysis of the photophysical dynamics due to the nanostructuring of anode interlayers in organic photovoltaics. <i>Physica Status Solidi A</i> . Copyright Wiley-VCH Verlag GmbH & Co. KGaA. Reproduced with permission.	34
Figure 43. Correlation between sol-LiF surface coverage and surface roughness of sol-LiF modified ITO with sequential spin-coating steps. Reproduced from <i>J. Mater. Sci. Mater. Electron</i> . Tuning hole charge collection efficiency in polymer photovoltaics by optimizing the work function of indium tin oxide electrodes with solution-processed LiF nanoparticles 2015, 9205–9212, Kurt, H., Jia, J., Shigesato, Y. & Ow-Yang, C. W. with permission of Springer.....	35
Figure 44. Correlation between surface work function of ITO, Φ , and surface coverage of sol-LiF nanostructures on ITO. Reproduced from <i>J. Mater. Sci. Mater. Electron</i> . Tuning hole charge collection efficiency in polymer photovoltaics by optimizing the work function of indium tin oxide electrodes with solution-processed LiF nanoparticles 2015, 9205–9212, Kurt, H., Jia, J., Shigesato, Y. & Ow-Yang, C. W. with permission of Springer.....	36
Figure 45. ITO coated pixelated anode glass substrates (left) and relevant dimensions (right)	41
Figure 46. Aluminum cathode deposition mask.	41
Figure 47. Chemical representation of PEDOT (left) and PSS (right) components of hole transport layer.	42
Figure 48. Chemical structure of P3HT (left) and PC ₆₀ BM (right)	42
Figure 49. Chemical structure of PCDTBT (left) and PC ₇₀ BM (right)	43
Figure 50. The FDTD model of aluminum back electrode used in the study.....	46
Figure 51. The FDTD model of ITO transparent electrode used in the study.....	46

Figure 52. The FDTD model of P3HT:PC₆₀BM bulk heterojunction active layer used in the study.....47

Figure 53. The FDTD model of PCDTBT:PC₇₀BM bulk heterojunction active layer used in the study.....47

Figure 54. The FDTD model of PEDOT:PSS hole transport layer used in the study.47

Figure 55. The FDTD simulation model used for P3HT:PC₆₀BM BHJ OPVs with sol-Au nanostructures on ITO surface. Black background represents the soda-lime glass, 100 nm thick grey layer represents the ITO anode, 40 nm thick teal layer represents the PEDOT:PSS HTL, 90 nm thick yellow layer represents the active layer, P3HT:PC₆₀BM and finally 100 nm thick blue layer represents Al cathode.48

Figure 56. The FDTD simulation model used for PCDTBT:PC₇₀BM BHJ OPVs with sol-Au nanostructures on ITO surface. Black background represents the soda-lime glass, 100 nm thick grey layer represents the ITO anode, 30 nm thick teal layer represents the PEDOT:PSS HTL, 70 nm thick yellow layer represents the active layer, PCDTBT:PC₇₀BM and finally 120 nm thick blue layer represents Al cathode.....48

Figure 57. Electric field intensity, $|E|$, profile of propagating light in a P3HT:PC₆₀BM BHJ OPV device with a sol-Au interlayer, through the thickness from $z = -100$ nm to $z = 200$ nm and over the wavelength range between 400 nm and 700 nm. The active layer is positioned between $z = 35$ nm and $z = 125$ nm. H. Kurt & C.W. Ow-Yang, Impedance Spectroscopy Analysis of the photophysical dynamics due to the nanostructuring of anode interlayers in organic photovoltaics. *Physica Status Solidi A*. Copyright Wiley-VCH Verlag GmbH & Co. KGaA. Reproduced with permission.49

Figure 58. The induced response electric field intensity, $|E|$, profile of the propagating light in a P3HT:PC₆₀BM OPV device with sol-Au interlayer, through the thickness from $z = -100$ nm to $z = 200$ nm at the wavelength of 610 nm. The active layer is positioned between $z = 35$ nm and $z = 125$ nm and represented as shaded. H. Kurt & C.W. Ow-Yang, Impedance Spectroscopy Analysis of the photophysical dynamics due to the nanostructuring of anode interlayers in organic photovoltaics. *Physica Status Solidi A*. Copyright Wiley-VCH Verlag GmbH & Co. KGaA. Reproduced with permission.50

Figure 59. The normalized power absorption, P_{abs} , profile of a P3HT:PC₆₀BM BHJ active layer with a sol-Au interlayer at the ITO/PEDOT:PSS interface. H. Kurt & C.W. Ow-Yang,

Impedance Spectroscopy Analysis of the photophysical dynamics due to the nanostructuring of anode interlayers in organic photovoltaics. *Physica Status Solidi A*. Copyright Wiley-VCH Verlag GmbH & Co. KGaA. Reproduced with permission.....51

Figure 60. The difference between the normalized power absorption, ΔP_{abs} , profile of a P3HT:PC₆₀BM BHJ active layer with a sol-Au interlayer at the ITO/PEDOT:PSS interface and the reference P3HT:PC₆₀BM BHJ active layer. H. Kurt & C.W. Ow-Yang, Impedance Spectroscopy Analysis of the photophysical dynamics due to the nanostructuring of anode interlayers in organic photovoltaics. *Physica Status Solidi A*. Copyright Wiley-VCH Verlag GmbH & Co. KGaA. Reproduced with permission.51

Figure 61. The induced response electric field intensity, $|E|$, profile as propagating light in a PCDTBT:PC₇₀BM(1:4) OPV device with sol-Au interlayer, through the thickness from $z = -100$ nm to $z = 200$ nm and over the wavelength range between 300 nm and 800 nm. The active layer is positioned between $z = 25$ nm and $z = 95$ nm. H. Kurt & C.W. Ow-Yang, Impedance Spectroscopy Analysis of the photophysical dynamics due to the nanostructuring of anode interlayers in organic photovoltaics. *Physica Status Solidi A*. Copyright Wiley-VCH Verlag GmbH & Co. KGaA. Reproduced with permission.....52

Figure 62. The response electric field intensity, $|E|$, profile as propagating light in a PCDTBT:PC₇₀BM OPV device with sol-Au interlayer, through the thickness from $z = -100$ nm to $z = 200$ nm at the wavelength of 633 nm. The active layer is positioned between $z = 25$ nm and $z = 95$ nm and represented as shaded. H. Kurt & C.W. Ow-Yang, Impedance Spectroscopy Analysis of the photophysical dynamics due to the nanostructuring of anode interlayers in organic photovoltaics. *Physica Status Solidi A*. Copyright Wiley-VCH Verlag GmbH & Co. KGaA. Reproduced with permission.53

Figure 63. The normalized power absorption, P_{abs} , profile of a PCDTBT:PC₇₀BM BHJ active layer with a sol-Au interlayer at the ITO/PEDOT:PSS interface, compared with the profile of a control device without the sol-Au layer. H. Kurt & C.W. Ow-Yang, Impedance Spectroscopy Analysis of the photophysical dynamics due to the nanostructuring of anode interlayers in organic photovoltaics. *Physica Status Solidi A*. Copyright Wiley-VCH Verlag GmbH & Co. KGaA. Reproduced with permission.53

Figure 64. The difference between the normalized power absorption, ΔP_{abs} , profile of a PCDTBT:PC₇₀BM BHJ active layer with a sol-Au interlayer at the ITO/PEDOT:PSS

interface and the reference PCDTBT:PC₇₀BM BHJ active layer. H. Kurt & C.W. Ow-Yang, Impedance Spectroscopy Analysis of the photophysical dynamics due to the nanostructuring of anode interlayers in organic photovoltaics. *Physica Status Solidi A*. Copyright Wiley-VCH Verlag GmbH & Co. KGaA. Reproduced with permission.....54

Figure 65. Current density–voltage characteristic curves of P3HT:PC₆₀BM solar cells with ITO anodes modified by different sol-LiF surface coverages, a) under AM1.5G illumination; b) in the dark. Reprinted from *J. Mater. Sci. Mater. Electron*. Tuning hole charge collection efficiency in polymer photovoltaics by optimizing the work function of indium tin oxide electrodes with solution-processed LiF nanoparticles 2015, 9205–9212, Kurt, H., Jia, J., Shigesato, Y. & Ow-Yang, C. W. with permission of Springer.....55

Figure 66. Current density–voltage characteristic curves of PCDTBT:PC₇₀BM solar cells with ITO anodes modified by different sol-LiF surface coverages under AM1.5G illumination.....57

Figure 67. Current–voltage characteristic curves of PCDTBT:PC₇₀BM solar cells with ITO anodes modified by different sol-LiF surface coverages under dark conditions.57

Figure 68. Current density–voltage characteristic curves of P3HT:PC₆₀BM solar cells with and without sol-Au modified ITO anodes under AM1.5G illumination. H. Kurt & C.W. Ow-Yang, Impedance Spectroscopy Analysis of the photophysical dynamics due to the nanostructuring of anode interlayers in organic photovoltaics. *Physica Status Solidi A*. Copyright Wiley-VCH Verlag GmbH & Co. KGaA. Reproduced with permission.....59

Figure 69. Current density–voltage characteristic curves of PCDTBT:PC₇₀BM solar cells with and without sol-Au modified ITO anodes under AM1.5G illumination. H. Kurt & C.W. Ow-Yang, Impedance Spectroscopy Analysis of the photophysical dynamics due to the nanostructuring of anode interlayers in organic photovoltaics. *Physica Status Solidi A*. Copyright Wiley-VCH Verlag GmbH & Co. KGaA. Reproduced with permission.....59

Figure 70. EQE of P3HT:PC₆₀BM control device, compared to ones with either a sol-LiF interlayer with surface coverage of 7.6% (red circles) or a sol-Au interlayer (blue triangles). H. Kurt & C.W. Ow-Yang, Impedance Spectroscopy Analysis of the photophysical dynamics due to the nanostructuring of anode interlayers in organic photovoltaics. *Physica Status Solidi A*. Copyright Wiley-VCH Verlag GmbH & Co. KGaA. Reproduced with permission.....61

Figure 71. EQE of PCDTBT:PC₇₀BM control device, compared to ones with either a sol-LiF interlayer with a surface coverage of 10.8% (red circles) or a sol-Au interlayer (blue triangles). H. Kurt & C.W. Ow-Yang, Impedance Spectroscopy Analysis of the photophysical dynamics due to the nanostructuring of anode interlayers in organic photovoltaics. *Physica Status Solidi A*. Copyright Wiley-VCH Verlag GmbH & Co. KGaA. Reproduced with permission.62

Figure 72. SEM micrographs of sol-Au nanoparticles (left) and sol-LiF nanoparticles (right) after a single deposition on a silicon wafer. The scale bar represents 200 nm. H. Kurt & C.W. Ow-Yang, Impedance Spectroscopy Analysis of the photophysical dynamics due to the nanostructuring of anode interlayers in organic photovoltaics. *Physica Status Solidi A*. Copyright Wiley-VCH Verlag GmbH & Co. KGaA. Reproduced with permission.....69

Figure 73. SEM micrographs of sol-Au nanoparticles (left) and sol-LiF nanoparticles (right) after a single deposition on ITO coated glass. The scale bar represents 200 nm. H. Kurt & C.W. Ow-Yang, Impedance Spectroscopy Analysis of the photophysical dynamics due to the nanostructuring of anode interlayers in organic photovoltaics. *Physica Status Solidi A*. Copyright Wiley-VCH Verlag GmbH & Co. KGaA. Reproduced with permission.....69

Figure 74. The equivalent circuit model used for our IS analysis. H. Kurt & C.W. Ow-Yang, Impedance Spectroscopy Analysis of the photophysical dynamics due to the nanostructuring of anode interlayers in organic photovoltaics. *Physica Status Solidi A*. Copyright Wiley-VCH Verlag GmbH & Co. KGaA. Reproduced with permission.....71

Figure 75. a) Absorption spectra showing the colloidal gold nanoparticle response, compared to the EQE of b) P3HT:PC₆₀BM control device, compared to ones with either a sol-LiF interlayer (red circles) or a sol-Au interlayer (blue triangles) and c) PCDTBT:PC₇₀BM. H. Kurt & C.W. Ow-Yang, Impedance Spectroscopy Analysis of the photophysical dynamics due to the nanostructuring of anode interlayers in organic photovoltaics. *Physica Status Solidi A*. Copyright Wiley-VCH Verlag GmbH & Co. KGaA. Reproduced with permission.75

Figure 76. The impedance response of the reference (Ref) device, the sol-LiF device (sol-LiF, red circles), and the plasmonic gold enhanced device (sol-Au, blue triangles) a) Cole-Cole plot of resistance (Z') and reactance (Z'') b) Frequency dependence of reactance (Z''). No DC bias applied. H. Kurt & C.W. Ow-Yang, Impedance Spectroscopy Analysis of the

photophysical dynamics due to the nanostructuring of anode interlayers in organic photovoltaics. *Physica Status Solidi A*. Copyright Wiley-VCH Verlag GmbH & Co. KGaA. Reproduced with permission.76

Figure 77. Recombination resistance (R_{rec}), chemical capacitance (C_{μ}) and recombination lifetime (τ_{rec}) vs. applied bias (V_{app}) for the P3HT:PC₆₀BM devices (a, c, and e respectively) and PCDTBT:PC₇₀BM devices (b, d, and f respectively). H. Kurt & C.W. Ow-Yang, Impedance Spectroscopy Analysis of the photophysical dynamics due to the nanostructuring of anode interlayers in organic photovoltaics. *Physica Status Solidi A*. Copyright Wiley-VCH Verlag GmbH & Co. KGaA. Reproduced with permission.....77

Figure 78. Mobile charge carrier density (n) vs applied bias (V_{app}) for the a) P3HT:PC₆₀BM devices and b) PCDTBT:PC₇₀BM devices. Recombination lifetime (τ_{rec}) vs. mobile charge carrier density (n) for the c) P3HT:PC₆₀BM devices and d) PCDTBT:PC₇₀BM devices. H. Kurt & C.W. Ow-Yang, Impedance Spectroscopy Analysis of the photophysical dynamics due to the nanostructuring of anode interlayers in organic photovoltaics. *Physica Status Solidi A*. Copyright Wiley-VCH Verlag GmbH & Co. KGaA. Reproduced with permission.79

Figure 79. Recombination rate vs. applied bias for the a) P3HT:PC₆₀BM devices and b) PCDTBT:PC₇₀BM devices. Recombination order vs. applied bias for the c) P3HT:PC₆₀BM devices and d) PCDTBT:PC₇₀BM devices. H. Kurt & C.W. Ow-Yang, Impedance Spectroscopy Analysis of the photophysical dynamics due to the nanostructuring of anode interlayers in organic photovoltaics. *Physica Status Solidi A*. Copyright Wiley-VCH Verlag GmbH & Co. KGaA. Reproduced with permission.82

Figure 80. Transport resistance (R_{tr}), transport capacitance (C_{tr}) and transport lifetime (τ_{tr}) vs. applied bias (V_{app}) for the P3HT:PC₆₀BM devices (a, c, and d respectively) and PCDTBT:PC₇₀BM devices (b, d, and f respectively). H. Kurt & C.W. Ow-Yang, Impedance Spectroscopy Analysis of the photophysical dynamics due to the nanostructuring of anode interlayers in organic photovoltaics. *Physica Status Solidi A*. Copyright Wiley-VCH Verlag GmbH & Co. KGaA. Reproduced with permission.....84

Figure 81. Fill factor (FF) of the photovoltaic cells vs. the estimated probability of charge recombination, γ , for each reference and interlayer-modified device. H. Kurt & C.W. Ow-Yang, Impedance Spectroscopy Analysis of the photophysical dynamics due to the

nanostructuring of anode interlayers in organic photovoltaics. *Physica Status Solidi A*.
Copyright Wiley-VCH Verlag GmbH & Co. KGaA. Reproduced with permission.....87

List of Tables

Table 1. List of copolymers used in this study.	5
Table 2. Sheet Resistance of sol-LiF and sol-Au modified ITO surfaces. Reprinted from <i>J. Mater. Sci. Mater. Electron.</i> Tuning hole charge collection efficiency in polymer photovoltaics by optimizing the work function of indium tin oxide electrodes with solution-processed LiF nanoparticles 2015, 9205–9212, Kurt, H., Jia, J., Shigesato, Y. & Ow-Yang, C. W. with permission of Springer.	29
Table 3. Water Droplet Contact Angle of sol-LiF and sol-Au nanostructured ITO surfaces before and after 30 minute of UV-ozone treatment. Reprinted from <i>J. Mater. Sci. Mater. Electron.</i> Tuning hole charge collection efficiency in polymer photovoltaics by optimizing the work function of indium tin oxide electrodes with solution-processed LiF nanoparticles 2015, 9205–9212, Kurt, H., Jia, J., Shigesato, Y. & Ow-Yang, C. W. with permission of Springer.	30
Table 4. The device parameters of P3HT:PC ₆₀ BM BHJ OPVs with different levels of LiF nanostructured ITO anodes under AM1.5G illumination. Average PCE was obtained from measurements of the best six performing devices. Reproduced from <i>J. Mater. Sci. Mater. Electron.</i> Tuning hole charge collection efficiency in polymer photovoltaics by optimizing the work function of indium tin oxide electrodes with solution-processed LiF nanoparticles 2015, 9205–9212, Kurt, H., Jia, J., Shigesato, Y. & Ow-Yang, C. W. with permission of Springer.	55
Table 5. The device parameters of PCDTBT:PC ₇₀ BM BHJ OPVs with different levels of LiF nanostructured ITO anodes under AM1.5G illumination.	58
Table 6. The device characteristics of sol-Au modified and reference P3HT:PC ₆₀ BM and PCDTBT:PC ₇₀ BM OPVs under AM1.5G illumination. H. Kurt & C.W. Ow-Yang, Impedance Spectroscopy Analysis of the photophysical dynamics due to the nanostructuring of anode interlayers in organic photovoltaics. <i>Physica Status Solidi A</i> . Copyright Wiley-VCH Verlag GmbH & Co. KGaA. Reproduced with permission.	60
Table 7. The device characteristics of interlayer-modified and reference P3HT:PC ₆₀ BM and PCDTBT:PC ₇₀ BM OPVs under AM1.5G illumination. H. Kurt & C.W. Ow-Yang, Impedance Spectroscopy Analysis of the photophysical dynamics due to the	

nanostructuring of anode interlayers in organic photovoltaics. *Physica Status Solidi A*. Copyright Wiley-VCH Verlag GmbH & Co. KGaA. Reproduced with permission.....74

Table 8. The estimated mobility of interlayer-modified and reference devices at open circuit condition under AM1.5G illumination from Equation (8). H. Kurt & C.W. Ow-Yang, Impedance Spectroscopy Analysis of the photophysical dynamics due to the nanostructuring of anode interlayers in organic photovoltaics. *Physica Status Solidi A*. Copyright Wiley-VCH Verlag GmbH & Co. KGaA. Reproduced with permission.....85

List of Abbreviations

2-D	two dimensional
AC	alternating current
AM 1.5G	global air mass coefficient at 1.5 atmosphere thickness
BHJ	bulk heterojunction
DC	direct current
EQE	external quantum efficiency
FDTD	finite-difference time-domain
HOMO	highest occupied molecular orbital
HTL	hole transport layer
IE	interface engineering
IS	impedance spectroscopy
ITO	indium tin oxide
LSPR	localized surface plasmon resonance
MPP	maximum power point
OPV	organic photovoltaic
P3HT	poly(3-hexylthiophene-2,5-diyl)
PC ₆₀ BM	[6,6]-phenyl-C61-butyric acid methyl ester
PC ₇₀ BM	[6,6]-phenyl-C71-butyric acid methyl ester
PCDTBT	poly[N-9'-heptadecanyl-2,7-carbazole-alt-5,5-(4',7'-di-2-thienyl-2',1',3'-benzothiadiazole)]
PCE	power conversion efficiency
PDI	polydispersity index
PEDOT:PSS	poly(3,4-ethylenedioxythiophene):polystyrene sulfonate
PESA	photoelectron spectroscopy in air
PML	perfectly matched layer
PS-b-P2VP	poly(styrene-b-2-vinyl pyridine)
PS-b-P4VP	poly(styrene-b-4-vinyl pyridine)
PTFE	polytetrafluoroethylene
RDF	radial distribution function

RMS	root mean square
RT	room temperature
SEM	scanning electron microscopy
sol-Au	solution-processed gold nanostructures
sol-LiF	solution-processed lithium fluoride nanostructures
THF	tetrahydrofuran
UV	ultraviolet

List of Symbols and Notations

μm	micrometer
μs	microsecond
C_g	geometrical capacitance
cm^2	centimeter square
C_{tr}	transport capacitance
C_μ	chemical capacitance
E	electric field
E_F	Fermi energy
eV	electronvolt
FF	fill factor
J	current density
J_{sat}	reverse saturation current
J_{sc}	short circuit current
k_{ext}	extraction rate
k_{rec}	recombination rate
M	molar
mA	milliampere
mbar	millibar
mg	milligram
min.	minutes
ml	milliliter
mm	millimeter
mM	millimolar
mTorr	milliTorr
mV	millivolt
mW	milliwatt
M_w	molecular weight
n	mobile charge density
n_0	initial charge carrier density at short circuit condition

nm	nanometer
°C	Celsius degrees
p	parallel – transverse magnetic
q	unit electronic charge
Q_{ext}	extinction cross section
rpm	rotation per minute
R_{rec}	recombination resistance
R_s	series resistance
R_{sh}	shunt resistance
R_{tr}	transport resistance
s	senkrecht – transverse electric
V	voltage
V_{oc}	open circuit voltage
W	watt
wt.%	weight percent
Z'	alternating current resistance
Z''	reactance
μl	microliter
Φ	work function
Ω	Ohm
Ω/\square	Ohm-square
$\Omega\text{-cm}^{-2}$	ohm per centimeter square
α	proportionality constant between bias and shift in the quasi-Fermi level
δ	recombination order
ϵ_0	permittivity of vacuum
ϵ_r	relative permittivity
γ	probability of charge recombination
μ	global charge mobility
τ_{rec}	recombination lifetime
τ_{tr}	transport lifetime

CHAPTER 1: INTRODUCTION

Organic photovoltaics (OPV) remain a competitive niche alternative for solar harvesting, based on their adaptability for low-cost roll-to-roll production and suitability for lightweight portable devices.^[1,2] The targets set for the commercialization of polymer-based bulk heterojunction (BHJ) OPV devices have been met recently by the development of new active layers^[3,4] and device architectures.^[5] However further performance enhancement and stability can still be realized by engineering the interfaces between the different functional layers, such as at the electrode,^[6] for reduced trap state density, better energy level alignment, improved charge collection, superior wettability, interfacial compatibility and light management.^[7] While considerable effort has been exerted into the development of state-of-art OPV devices, their success heavily depends on expanding our understanding of *i)* the operational dynamics of the devices and *ii)* how functional interlayers affect device operation in particular.

Owing to the limited compatibility between OPV constituent interlayers of intrinsically different structures at the molecular level, organic-inorganic interfaces often result in poor device performance through recombination losses, which result in low charge collection efficiency, inefficient charge separation and poor light management within the devices.^[8] By improving the compatibility of the electronic structure at the low work function (Φ) electrode interfaces, mobile hole extraction efficiency and charge separation efficiency can be increased, thereby lowering recombination losses and enhancing the electronic hole contribution to the current density. In this context, the surface energy and Φ of the electrode, typically of tin-doped indium oxide (ITO) in conventional BHJ OPV device architectures, are key factors determining the overall device performance. By engineering these physical properties of the ITO film surface, one can amplify the level of interaction between the incident light and the active layer, consequently increasing the internal quantum efficiency and hence the charge generation rate. In this perspective, plasmonic nanostructures that can manipulate light below sub-wavelength regime are under the spot light since the active layer thicknesses are well below wavelength of the solar radiation spectrum.

To tune the properties of the electrode/active layer interface, a panoply of approaches have been adopted^[9]—self-assembled monolayers,^[10–12] and chlorine surface modification;^[13] organic layers;^[14–16] carbon-based nanomaterials;^[17,18] transition-metal oxides;^[19–23] and alkali halides such as CsF and LiF.^[24] Interlayer engineering (IE) enables not only the tuning of charge collection efficiency and charge selectivity on both electrodes, but also control over OPV stability and durability. An additional parameter for tuning at the high Φ electrode is PEDOT:PSS, which is commonly used as an electronic hole transport/electron-blocking layer. Considering the low electronic homogeneity^[25] and the low-pH nature of PEDOT:PSS, the interface it forms with ITO offers limited electron-blocking capability,^[26] as well as chemical instability leading to Indium diffusion into active layers.^[27] In the light management perspective, noble metal nanostructures^[7] between the interlayers of OPV devices were employed^[28] unfortunately the effects of them were not thoroughly investigated.

The hypothesis that forms the premise of this dissertation study was that solution-processed nanostructured interlayers at the low work function electrode can be used to optimize the performance of BHJ OPVs. More specifically we investigated two different strategies in parallel. Firstly, solution processed dielectric LiF (sol-LiF) nanostructuring on the ITO anode can be used to increase hole charge collection, by allowing tuning the energy level alignment between the ITO anode and the organic interlayers. Secondly, solution-processed plasmonic Au (sol-Au) nanostructuring on the ITO anode can enable increasing the generation rate, by enhancing light absorption and consequently photoconversion rates within the active layers.

In order to test our hypothesis, we had to obtain uniform dispersions of LiF and Au nanoparticles. We have used the reverse diblock copolymer micelle reactor method to obtain size monodisperse sol-LiF and sol-Au nanoparticles that can be deposited with controllable areal density. We then prepared sol-LiF and sol-Au nanostructured ITO anodes using spin coating. The surface physical properties were analyzed by scanning electron microscopy, atomic force microscopy, wetting contact angle measurements, absorption spectroscopy, and photoelectron spectroscopy in air (PESA). In order to evaluate the performance of these nanostructured ITO anodes, we have incorporated them into BHJ

OPVs consisting of two different types of BHJ polymer blends, chosen due to their significantly dissimilar highest occupied molecular orbital (HOMO) levels. The J-V device characteristics were measured, and the device parameters were extracted and compared. To rule out optical effects of sol-LiF and confirm the sol-Au interlayer induced field enhancement, the external quantum efficiency (EQE) profiles were evaluated. Additionally, we had investigated the induced electric field enhancement by LSPR in sol-Au investigated by implementing finite difference time domain (FDTD) simulations, and compared the results with the experimentally obtained EQE profiles for both types of BHJ polymer blends. Finally, to elucidate the underlying mechanisms for improving device performance in sol-LiF and sol-Au interlayers in the both types of BHJ polymer blends, in-situ impedance spectroscopy was implemented. This work was the first in-depth IS analysis targeting the role of the anode interface and was developed in this dissertation to provide more detailed insight on photophysical BHJ OPV dynamics of buried interfaces, well beyond what can be obtained from analyzing J-V characteristics. Herein we have used IS to distinguish the effects of two different nanostructured interlayers—quasi 2-D arrays of sol-LiF and sol-Au nanostructures—on the charge generation/recombination and charge transport/collection kinetics in bulk heterojunction organic solar cells in detail.

CHAPTER 2: NANOSTRUCTURED INDIUM TIN OXIDE TRANSPARENT CONDUCTORS

2.1. Introduction

The hypothesis that we had addressed in the focused study in this chapter was the tunability afforded by modifying the ITO anode surface with size monodisperse nanostructures. To this end, we produce 2-D dispersions of sol-LiF and sol-Au of different surface coverages. The nanostructuring enables tuning of the surface work function, in the case of sol-LiF, and tuning the overlap between the spectral region of LSPR response to BHJ absorption, in the case of sol-Au.

We used the reverse diblock copolymer micelle technique to deposit on ITO surfaces,^[29] a 2-D dispersion of solution-processed, size mono-disperse nanoparticles; of these we considered separately either dielectric LiF (sol-LiF) or plasmonic Au nanoparticles (sol-Au). The solution-processed nanoparticle dispersions are compatible with roll-to-roll fabrication techniques and provide a low-cost alternative to vacuum-based deposition techniques. Reverse diblock copolymer micelles were used in apolar solvents to load the hydrophilic precursor chemicals into the micelle nanoreactor in a controlled manner. The resulting nanoparticle dispersion was deposited on substrates by spin coating. We investigated the surface morphology of the nanostructured surfaces with scanning electron microscopy. For sol-LiF nanoparticles, the change in the surface work-function of the modified ITO surface was tracked with photoelectron emission spectroscopy in air (PESA) and correlated with surface coverage obtained by quantitative analysis of processed SEM images. For sol-Au nanoparticles, finite difference time domain simulations and UV-visible absorption spectroscopy were used to evaluate the plasmonic response.

This chapter of the thesis is mainly based on our previously published work.^[30] Reprinted and adapted from *J. Mater. Sci. Mater. Electron.* Tuning hole charge collection efficiency in polymer photovoltaics by optimizing the work function of indium tin oxide electrodes with solution-processed LiF nanoparticles 2015, 9205–9212, Kurt, H., Jia, J., Shigesato, Y. & Ow-Yang, C. W. with permission of Springer.

2.2. Experimental

2.2.1. Materials

Poly(styrene-*b*-2-vinyl pyridine) (PS-*b*-P2VP) and poly(styrene-*b*-4-vinyl pyridine) (PS-*b*-P4VP) diblock copolymers were purchased from Polymer Source Inc. (Montreal, Quebec, Canada). The chemical structure of diblock copolymers were shown in Figure 1 and Figure 2. The molecular weight (M_w) and the polydispersity index (PDI) of polymers used are listed in Table 1.

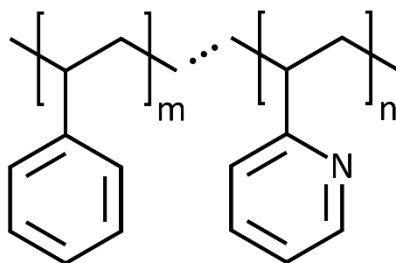


Figure 1. Poly(styrene-*b*-2-vinyl pyridine) copolymer

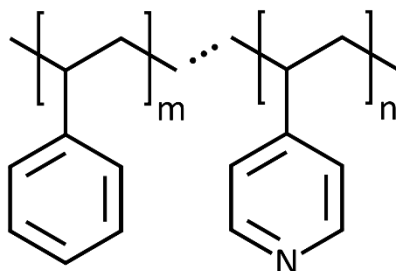


Figure 2. Poly(styrene-*b*-4-vinyl pyridine) copolymer

Table 1. List of copolymers used in this study.

Polymer	Product ID	M_w	PDI
PS- <i>b</i> -P2VP	P1330-S2VP	48500- <i>b</i> -70000	1.13
PS- <i>b</i> -P2VP	P10491-S2VP	183000- <i>b</i> -52000	1.13
PS- <i>b</i> -P2VP	P4556-S2VP	180000- <i>b</i> -77000	1.09
PS- <i>b</i> -P4VP	P3910-S4VP	109000- <i>b</i> -27000	1.12

Lithium hydroxide (LiOH, 99.9%, Merck), hydrogen fluoride (HF, 40%, Merck), gold chloride hydrate ($\text{HAuCl}_4 \cdot x\text{H}_2\text{O}$, 99.999%, Aldrich), hydrazine monohydrate ($\text{NH}_2\text{NH}_2 \cdot \text{H}_2\text{O}$, 99.9%, Merck), hydroxylamine hydrochloride ($\text{NH}_2\text{OH} \cdot \text{HCl}$, 98.0%, Aldrich), toluene (99.9%, Merck), tetrahydrofuran (THF, 99.9%, Merck), hexane (99.9%, Merck), acetone (99.8%, Sigma), methanol (99.8%, Sigma) and ethanol (99.8%, Sigma) were used as received.

Occasionally inconsistent high polydisperse micelles formed, indicating that the PS-b-P2VP copolymer has aged and requires purification by the following procedure:

1. 200 mg of the PS-b-P2VP copolymer was dissolved in 6 ml THF using an ultrasonication bath.
2. The PS-b-P2VP copolymer was poured into glass wool-filled glass pipette.
3. 100 ml of hexane was vigorously mixed in a beaker underneath the glass pipette.
4. The PS-b-P2VP copolymer was precipitated dropwise in its non-solvent hexane.
5. The precipitated copolymer was collected and dried by vacuum filtration, using a porcelain Büchner funnel, Grade 2 filter paper with 8 μm pore size, and a suction flask.
6. The precipitated copolymer was further rinsed in hexane on the funnel filter.
7. The PS-b-P2VP copolymer was collected on a filter paper and dried in furnace overnight at 70°C

Indium tin oxide (ITO) thin film-coated substrates (ultrasmooth, 1 cm \times 1 cm, $\sim 40 \Omega/\square$) were purchased from TFD Inc (Thin Film Devices Eagle XG, Anaheim, CA, USA). Si substrates were purchased from University Wafer (#444, University Wafer, Boston, MA, USA).

2.2.2. Synthesis of Lithium Fluoride Nanoparticles in PS-b-P2VP copolymer

The following reaction amounts are optimized values in the experiments.

- 15 mg of PS(48500)-b-P2VP(70000) was dissolved in 5 ml of toluene under vigorous stirring for 24 hours at RT.

- 1.2 mg of LiOH was added to the micelle solution under vigorous stirring for 94 hours at RT.
- The solution was centrifuged at 4500 rpm for 40 minutes, in order to allow the undissolved LiOH crystals to sediment.
- Undissolved crystals were precipitated to bottom of the falcon tube. The supernatant solution was extracted for further reaction.
- 2.8 μ l of HF was added to the LiOH loaded micellar solution under continuous stirring for 24 hours at room temperature (RT).

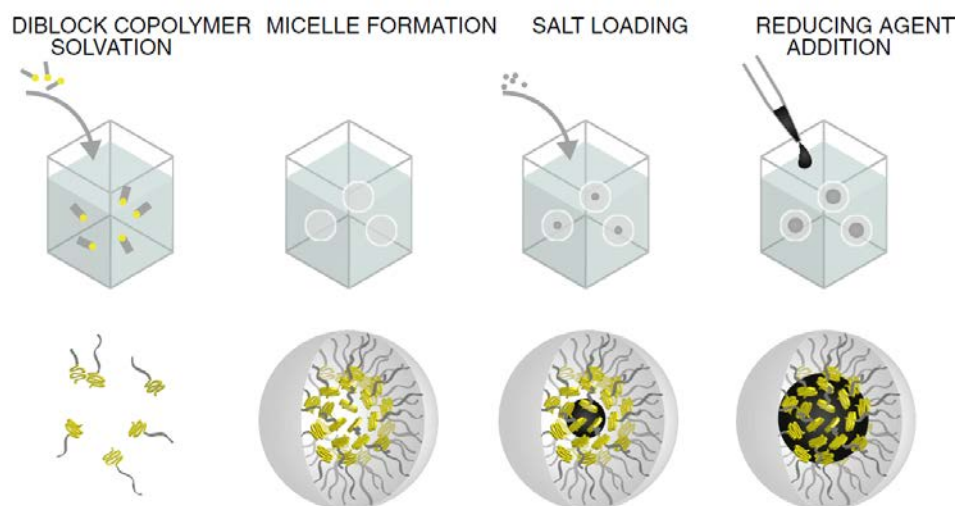


Figure 3. Loading and reduction of LiOH and HAuCl₄ in diblock copolymer micelles.^[31] Reprinted from *Thin Solid Films*, 559, Ow-Yang, C.W., Jia, J., Aytun, T., Zamboni, M., Turak, A., Saritas, K., and Shigesato Y. Work function tuning of tin-doped indium oxide electrodes with solution-processed lithium fluoride, 58–63, Copyright 2014, with permission from Elsevier.

2.2.3. Synthesis of Gold Nanoparticles in PS-b-P2VP and PS-b-P4VP copolymers

The following reaction amounts are optimized values and reagents in the experiments. Three different diblock copolymers were used for gold precursor-loaded diblock copolymer micelles as listed in Table 1.

- 25 mg of PS(180000)-b-P2VP(77000) was dissolved in 5 ml of toluene under vigorous stirring for 24 hours at RT.

- HAuCl_4 gold precursor was added to the micelle solution with loading ratio of 0.5 (molar ratio of gold precursor to 2-pyridine in PS-b-P2VP under vigorous stirring for 48 hours at RT.
- Centrifugation was not used since the gold precursor had dissolved completely
- Reduction of gold precursor was realized by either oxygen plasma processing after depositing a monolayer of the loaded micelles onto surfaces or using hydrazine in solution.

2.2.4. Deposition of sol-LiF and sol-Au and etching of polymeric micelles

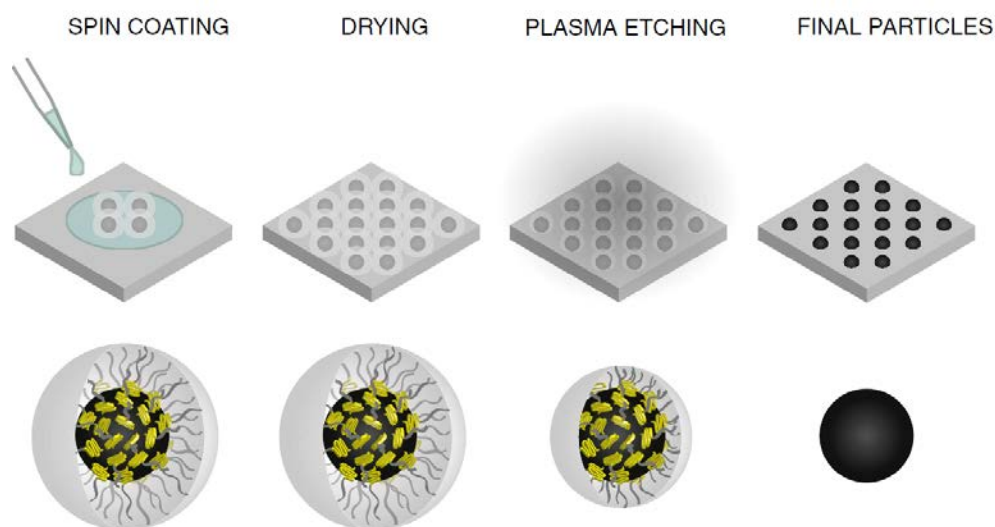


Figure 4. Deposition and etching of loaded micelles on surfaces.^[31] Reprinted from *Thin Solid Films*, 559, Ow-Yang, C.W., Jia, J., Aytun, T., Zamboni, M., Turak, A., Saritas, K., & Shigesato Y. Work function tuning of tin-doped indium oxide electrodes with solution-processed lithium fluoride, 58–63, Copyright 2014, with permission from Elsevier.

Silicon and ITO-coated glass substrates were used in the formation of nanoparticle arrays. Prior to usage, the substrates were cleaned with acetone, methanol and ethanol successively in an ultrasonication bath 15 minutes each at RT. Substrates were dried using a N_2 stream initially and further dried at 70°C in a furnace for 4+ hours. In the cleaning procedure, the substrates were placed in substrate racks to prevent surface damage.

10-15 μl of LiF and gold precursor-loaded micelle solutions were spin-coated on $1.0 \times 1.0 \text{ cm}^2$ substrates at 2000 and 5000 rpm respectively for 40 seconds. The spin coating speed was optimized for ensuring a close-packed monolayer coverage of micelles on the substrates. Gold precursor loaded micelle coated substrates were further annealed under a toluene vapor at RT for 24 hours in a desiccator, in order to improve the ordering of micelles, i.e., to achieve close-packing. Gold precursor-loaded micelle coated substrates were exposed to 6 W UV-light (365 nm) for 30, 60 and 90 minutes prior to oxygen plasma etching procedure.

In order to remove the polymeric micelles surrounding the nanoparticles, an O_2 plasma etch was used. The oxygen plasma etching parameters were optimized to ensure complete removal of polymeric matter and complete reduction of gold precursor to elemental gold. In order to prevent physical etching of LiF and Au nanoparticles, relatively high pressure and low power plasma conditions yielded optimal results. Specifically, for both nanoparticle species, plasma etching was performed using a Harrick Plasma PDC-002 with parameters of 29.6 W and 900 mTorr O_2 gas pressure for 90 minutes.

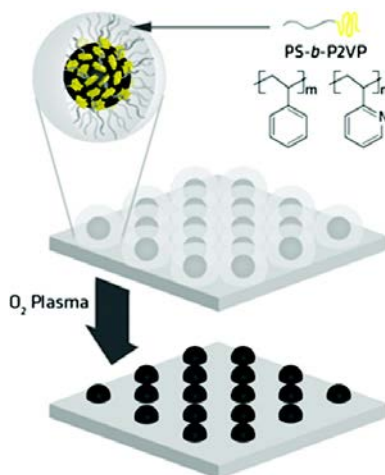


Figure 5. Etching of polymeric micelles.^[29] Reprinted with permission from Aytun, T., Turak, A., Baikie, I., Halek, G. & Ow-Yang, C. W. *Nano Lett.* 12, 39–44 (2012). Copyright 2012 American Chemical Society.

The gold precursor-loaded micelles were spin-coated on the substrates with previously defined parameters. The substrates were exposed to O₂ plasma etching for 45 minutes (half of the usual duration). While the oxygen plasma procedure removed a portion of the polymeric content, the lower part of the micelles had remained intact.

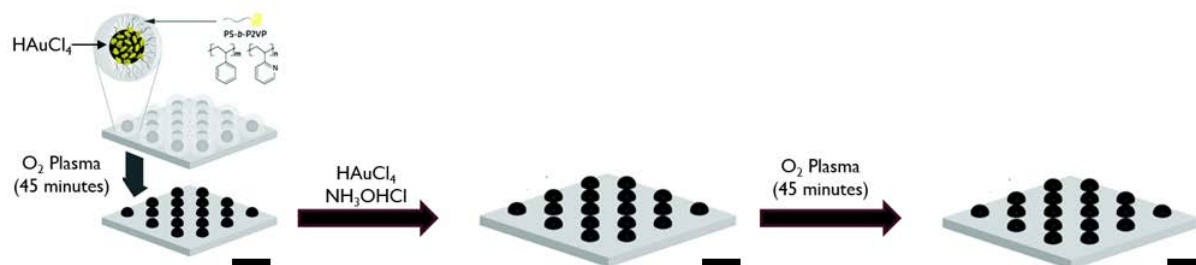


Figure 6. Growth of gold precursor loaded polymeric micelles. The scale bar represents length of 30 nm. Adapted with permission from Aytun, T., Turak, A., Baikie, I., Halek, G. & Ow-Yang, C. W. *Nano Lett.* 12, 39–44 (2012). Copyright 2012 American Chemical Society.

2 M hydroxylamine stock solution and 1 wt. % of H_{AuCl₄} were prepared in milli-Q water. The plasma treated spin-coated substrates were immersed into 1 wt. % of H_{AuCl₄} / 0.4 mM hydroxylamine mixture for 15, 30, 45 and 60 seconds. The substrates were rinsed after the procedure using Milli-Q water and dried with slow N₂ stream. The remaining polymeric content was completely removed upon expose to oxygen plasma etching for 45 minutes.

LiF and Au NP deposited substrates were cleaned with acetone, methanol and ethanol successively 10 minutes each in an ultrasonication bath at RT for device fabrication.

2.2.5. Finite Difference Time Domain (FDTD) Simulations

In order to evaluate the plasmonic field of the gold nanoparticle interlayers when excited by incident solar irradiation, full-field electromagnetic simulations were implemented using a commercial FDTD software (Lumerical FDTD Solutions). The array of sol-Au nanoparticles were simulated as hemispheres with a radius of 10 nm and in 2-D hexagonal ordering with an interparticle distance of 60 nm. In order to evaluate the substrate effects,

the array of sol-Au nanoparticles were also simulated on a soda-lime glass substrate. The optical constants of other components—soda lime glass,^[32] ITO,^[33] LiF,^[34] Al,^[35] and Au^[36]—were obtained through the website, <http://refractiveindex.info>. The material data was prefitted into the FDTD model prior to implementation in the simulations in Lumerical Material Explorer, as shown Figure 7.

The simulated light source was *s* and *p* polarized plane wave in the 300-900 nm wavelength range with a pulse length of 1.9947 femtoseconds and positioned in $z = 10$ nm and propagating in the $-z$ direction. In order to simulate the unpolarized nature of solar irradiance, the simulations with *s* and *p* polarized excitations were averaged. The *x-y* cross-sectional simulation area was set to $60 \text{ nm} \times 103.923 \text{ nm}$ with a depth of 60 nm in the *z* direction, as shown in **Error! Reference source not found.** and Figure 9; the hexagonal array was defined with an interparticle distance of 60 nm and angle of 60° between the axis. The array was positioned in the plane of $z = 5$ nm. The boundary conditions used were perfectly matched layers (PML) along the propagation axis, *z*, and periodic boundary conditions in the *x* and *y* directions in order to simulate a collective response of the surface. A maximum mesh size of 0.5 nm was set in all spatial directions of the simulation region to ensure the highest resolution for the simulation.

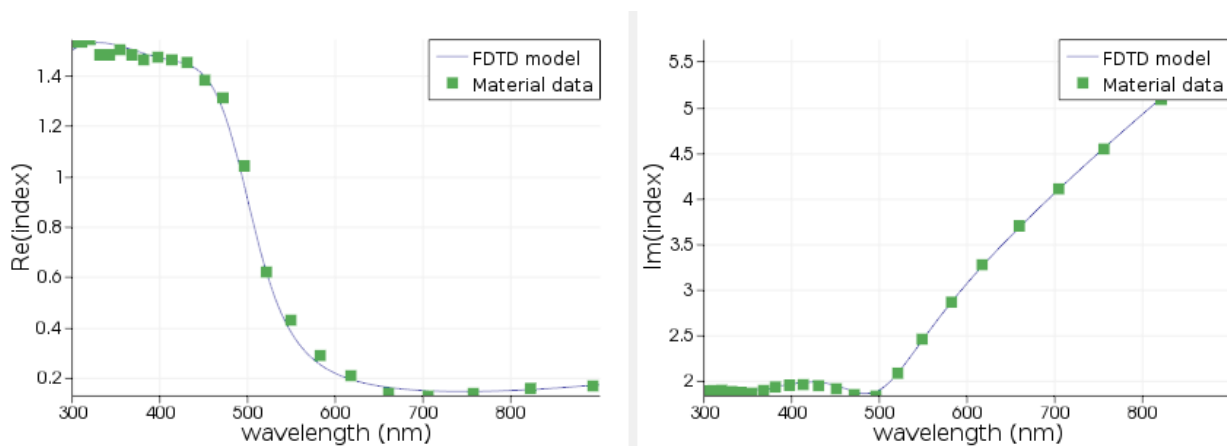


Figure 7. The FDTD model of gold used in the study.

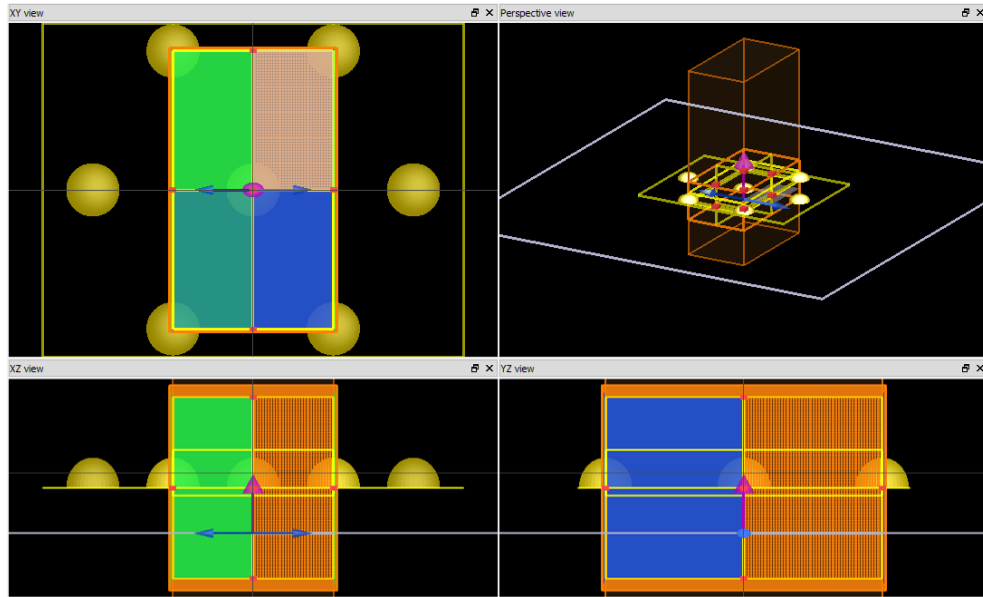


Figure 8. FDTD model of the gold hemisphere array in vacuum. The excitation source was placed beneath the base of the sol-Au hemispheres, simulating the illumination configuration of the nanostructured OPVs. The propagation direction of excitation is indicated by the magenta arrow. The polarization of the excitation is represented by the blue arrows.

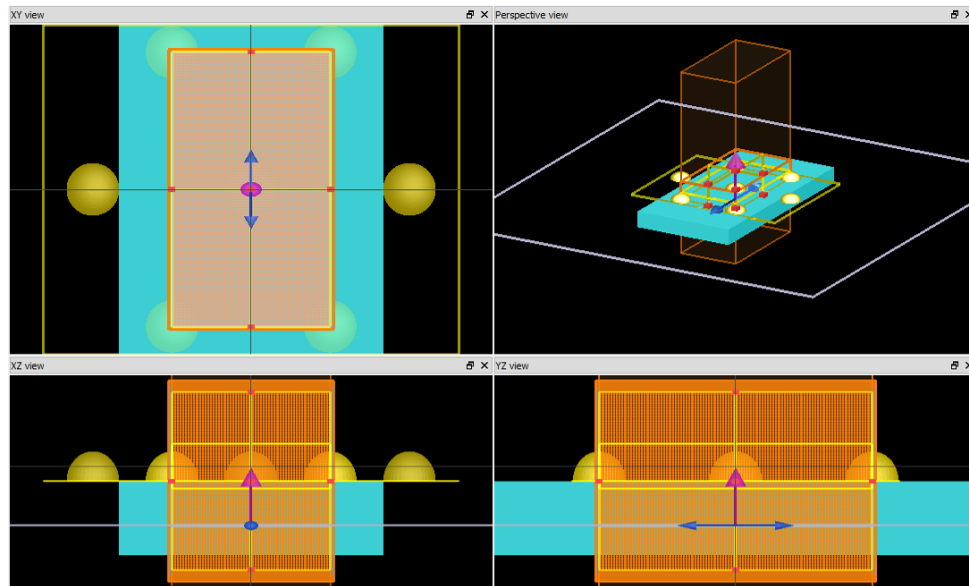


Figure 9. FDTD model of the gold hemisphere array on soda lime glass (teal-colored layer). The excitation source was position at the base of the sol-Au hemispheres. The propagation direction of excitation is indicated by the purple arrow. The polarization of the excitation is represented by the blue arrows.

2.3. Results

2.3.1. SEM micrographs and image analysis

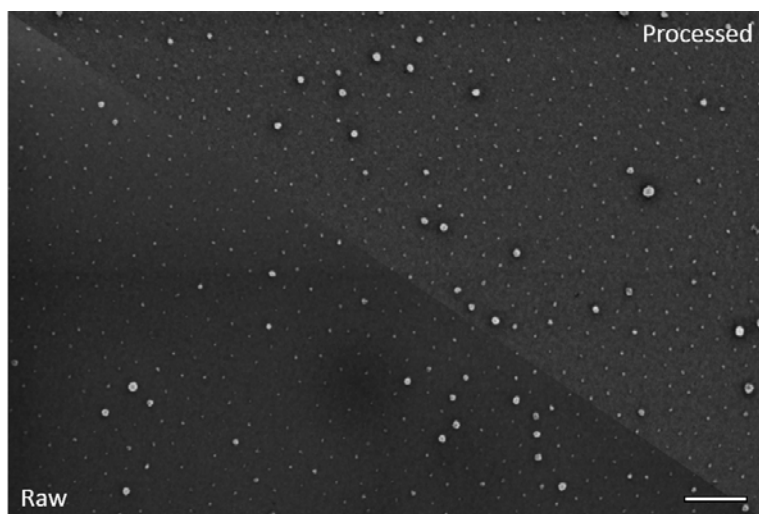


Figure 10. Raw and processed SEM micrograph of 1x sol-LiF deposition, 2% surface coverage.^[37] The scale bar represents 200 nm. Reprinted from *J. Mater. Sci. Mater. Electron.* Tuning hole charge collection efficiency in polymer photovoltaics by optimizing the work function of indium tin oxide electrodes with solution-processed LiF nanoparticles 2015, 9205–9212, Kurt, H., Jia, J., Shigesato, Y. & Ow-Yang, C. W. with permission of Springer.

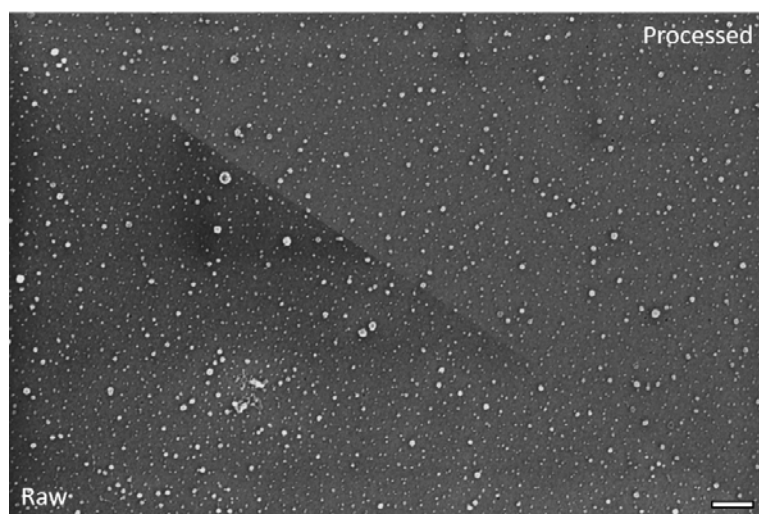


Figure 11. Raw and processed SEM micrograph of 1x sol-LiF deposition, 5.6% surface coverage.^[37] The scale bar represents 200 nm. Reprinted from *J. Mater. Sci. Mater. Electron.* Tuning hole charge collection efficiency in polymer photovoltaics by optimizing the work function of indium tin oxide electrodes with solution-processed LiF nanoparticles 2015, 9205–9212, Kurt, H., Jia, J., Shigesato, Y. & Ow-Yang, C. W. with permission of Springer.

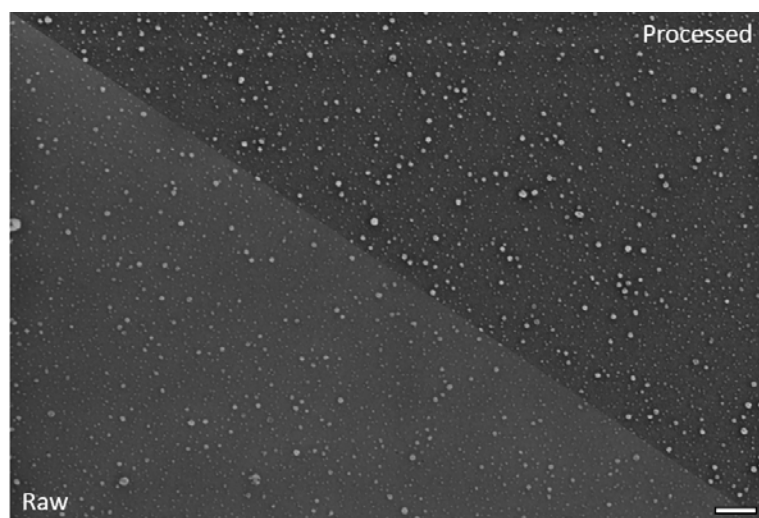


Figure 12. Raw and processed SEM micrograph of 5x sol-LiF deposition, 8.7% surface coverage.^[37] The scale bar represents 200 nm. Reprinted from *J. Mater. Sci. Mater. Electron.* Tuning hole charge collection efficiency in polymer photovoltaics by optimizing the work function of indium tin oxide electrodes with solution-processed LiF nanoparticles 2015, 9205–9212, Kurt, H., Jia, J., Shigesato, Y. & Ow-Yang, C. W. with permission of Springer.

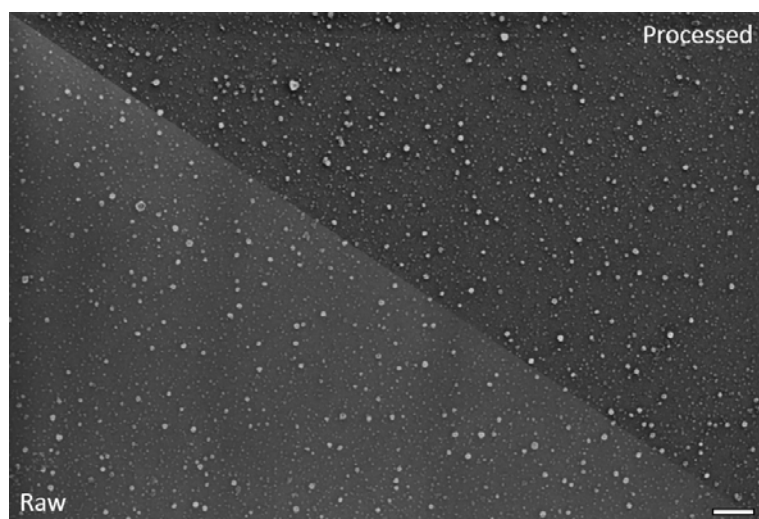


Figure 13. Raw and processed SEM micrograph of 7x sol-LiF deposition, 10.1% surface coverage.^[37] The scale bar represents 200 nm. Reprinted from *J. Mater. Sci. Mater. Electron.* Tuning hole charge collection efficiency in polymer photovoltaics by optimizing the work function of indium tin oxide electrodes with solution-processed LiF nanoparticles 2015, 9205–9212, Kurt, H., Jia, J., Shigesato, Y. & Ow-Yang, C. W. with permission of Springer.

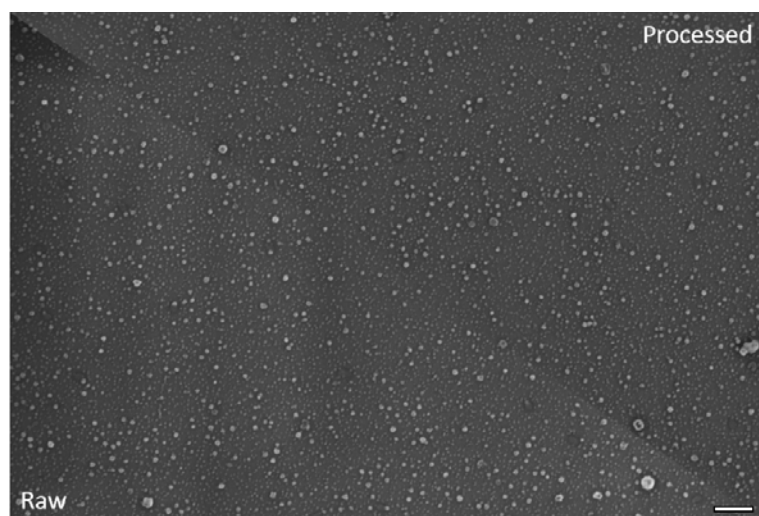


Figure 14. Raw and processed SEM micrograph of 10x sol-LiF deposition, 13.2% surface coverage.^[37] The scale bar represents 200 nm. Reprinted from *J. Mater. Sci. Mater. Electron.* Tuning hole charge collection efficiency in polymer photovoltaics by optimizing the work function of indium tin oxide electrodes with solution-processed LiF nanoparticles 2015, 9205–9212, Kurt, H., Jia, J., Shigesato, Y. & Ow-Yang, C. W. with permission of Springer.

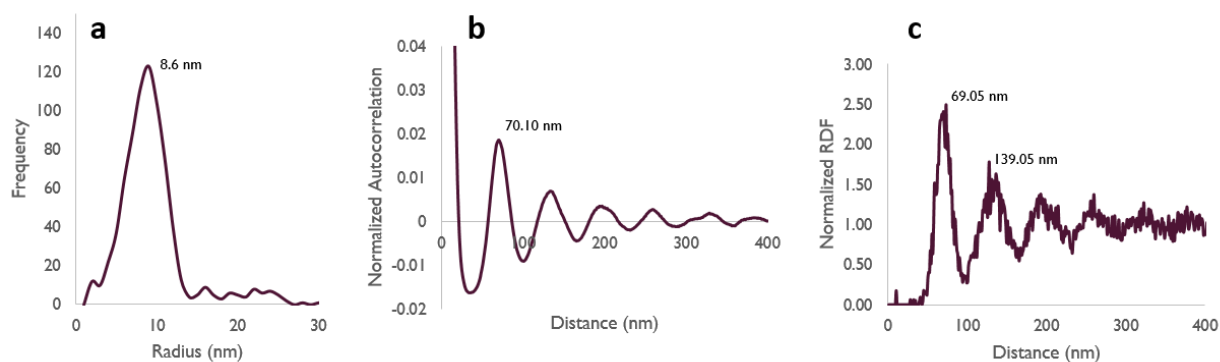


Figure 15. Single deposition, sol-LiF nanoparticle size histogram (a), normalized autocorrelation function between centers of the sol-LiF nanoparticles (b), normalized radial distribution function of sol-LiF nanoparticles (c). Reprinted from *J. Mater. Sci. Mater. Electron.* Tuning hole charge collection efficiency in polymer photovoltaics by optimizing the work function of indium tin oxide electrodes with solution-processed LiF nanoparticles 2015, 9205–9212, Kurt, H., Jia, J., Shigesato, Y. & Ow-Yang, C. W. with permission of Springer.

A single deposition of sol-LiF nanoparticles yielded a highly monodisperse array of nanocrystals with an average radius of 8.6 ± 0.8 nm, as shown in Figure 15a. A number of larger sol-LiF nanoparticles were also observed, although they remain as precursor loading anomalies, due to the hygroscopic nature of lithium hydroxide precursor. In Figure 15b, the normalized autocorrelation revealed a highly ordered arrangement of nanostructures, up to 5th nearest neighbor. Since autocorrelation reveals the ordering by using the mass centers of the nanostructures, the radial distribution function (RDF) method was also employed and confirmed the highly ordered arrangement of sol-LiF nanoparticles shown in Figure 15c. The average distance between centers of sol-LiF nanoparticles were 69-70 nm.

Sequential spin-coating deposition of sol-LiF nanoparticles on substrates showed increasing surface coverage. A single deposition of sol-LiF yielded a surface coverage of 2%. Three sequential depositions increased the coverage to 5.3%. The trend continued quasi-linearly up to 10.8% surface coverage with 7 deposition cycles (Figure 16). However, the linearity between sequential spin-coating cycles and surface coverage started to diminish at a surface coverage of 13.2% for 10 deposition cycles.

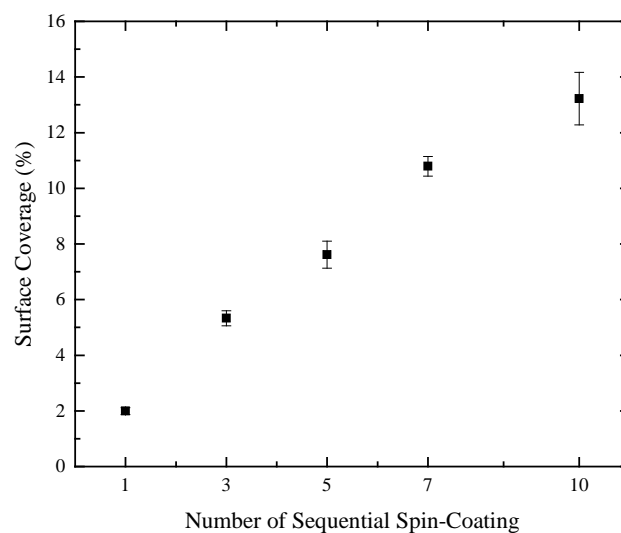


Figure 16. Number of sequential spin-coating versus LiF surface coverage. Reproduced from *J. Mater. Sci. Mater. Electron.* Tuning hole charge collection efficiency in polymer photovoltaics by optimizing the work function of indium tin oxide electrodes with solution-processed LiF nanoparticles 2015, 9205–9212, Kurt, H., Jia, J., Shigesato, Y. & Ow-Yang, C. W. with permission of Springer.

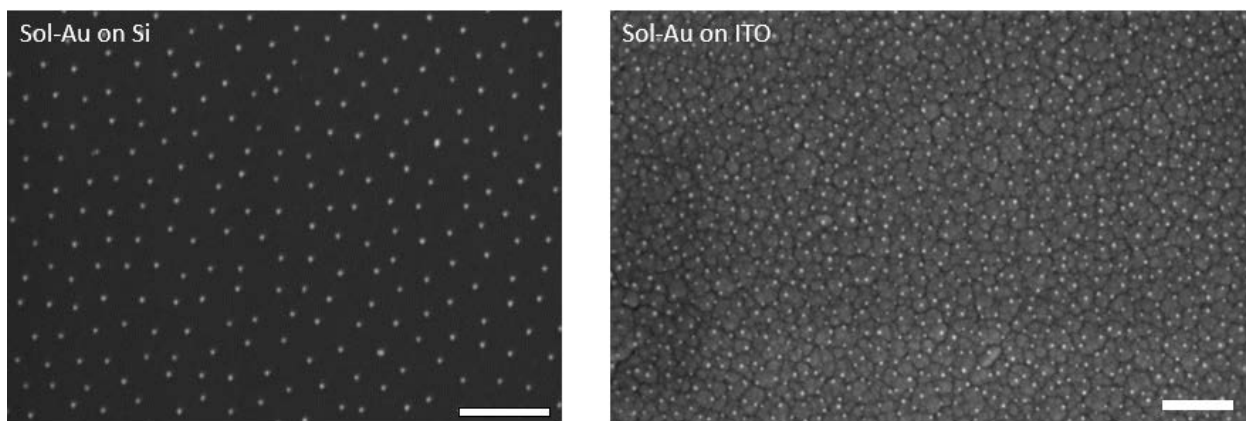


Figure 17. SEM micrographs of sol-Au nanoparticles on Si wafer (left) and sol-Au nanoparticles on ITO coated glass (right) after a single deposition. The scale bar represents 200 nm. H. Kurt & C.W. Ow-Yang, Impedance Spectroscopy Analysis of the photophysical dynamics due to the nanostructuring of anode interlayers in organic photovoltaics. *Physica Status Solidi A*. Copyright Wiley-VCH Verlag GmbH & Co. KGaA. Reproduced with permission.

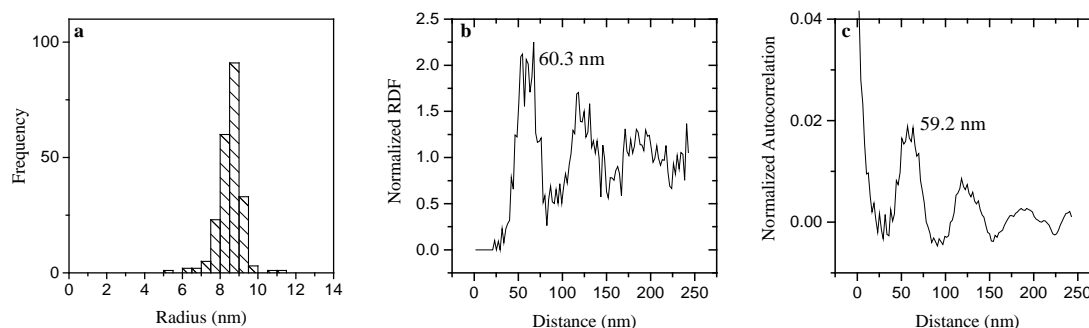


Figure 18. Single deposition, sol-Au nanoparticle size histogram (a), normalized autocorrelation function between centers of the sol-Au nanoparticles (b), normalized radial distribution function of sol-Au nanoparticles (c).

In the case of sol-Au deposition, sol-Au nanoparticles have a higher monodispersity in the size distribution on Si wafer and ITO surface with a quasi-ordered dispersion as shown in Figure 17. Image analysis revealed that the nanoparticle size distribution was monodisperse, with an average radius of 8.7 ± 0.6 nm in Figure 18a. Both the autocorrelation and the radial distribution function showed the average distance between nanoparticles to be 60 nm in Figure 18b and c. The short-range of order was observed up to 3rd nearest neighbor.

2.3.2. AFM images and image analysis

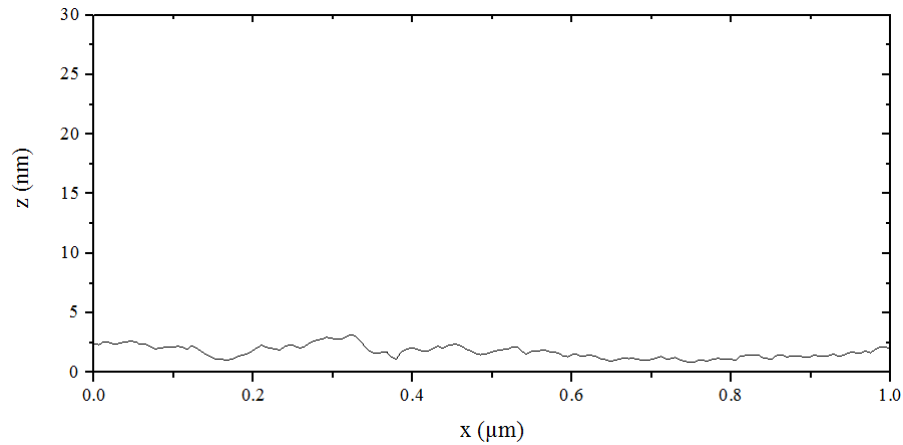


Figure 19. AFM line profile of bare ITO substrate. Reprinted from *J. Mater. Sci. Mater. Electron.* Tuning hole charge collection efficiency in polymer photovoltaics by optimizing the work function of indium tin oxide electrodes with solution-processed LiF nanoparticles 2015, 9205–9212, Kurt, H., Jia, J., Shigesato, Y. & Ow-Yang, C. W. with permission of Springer.

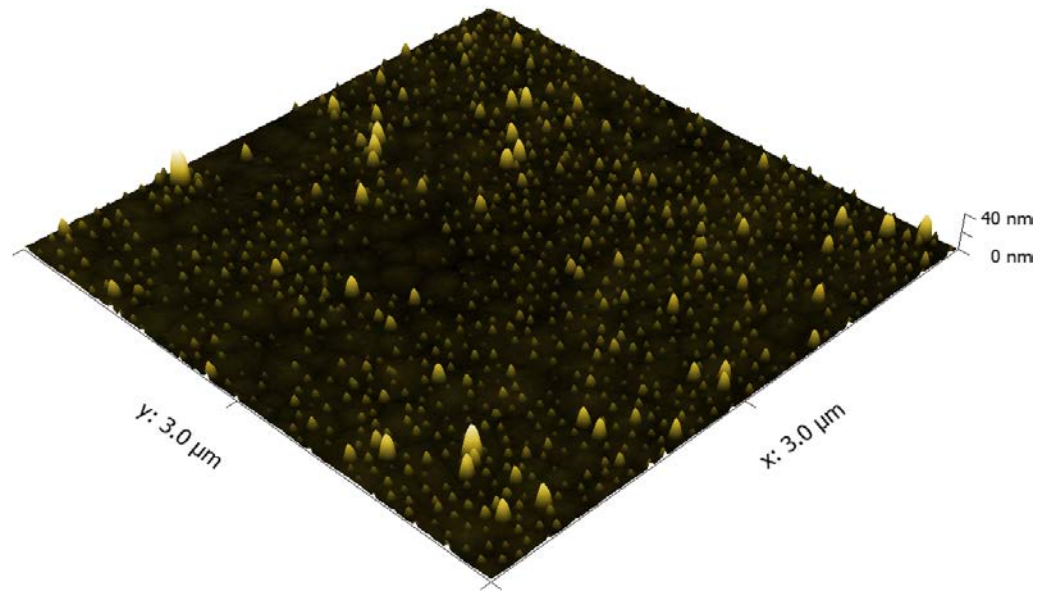


Figure 20. 3D AFM image of 1x sol-LiF deposition on ITO, with 2% surface coverage. Reprinted from *J. Mater. Sci. Mater. Electron.* Tuning hole charge collection efficiency in polymer photovoltaics by optimizing the work function of indium tin oxide electrodes with solution-processed LiF nanoparticles 2015, 9205–9212, Kurt, H., Jia, J., Shigesato, Y. & Ow-Yang, C. W. with permission of Springer.

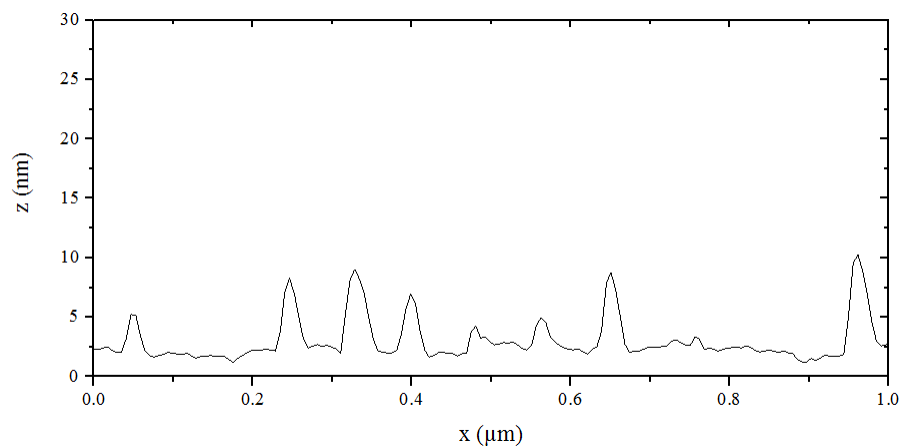


Figure 21. AFM line profile of 1x sol-LiF deposition on ITO, with 2% surface coverage. Reprinted from *J. Mater. Sci. Mater. Electron.* Tuning hole charge collection efficiency in polymer photovoltaics by optimizing the work function of indium tin oxide electrodes with solution-processed LiF nanoparticles 2015, 9205–9212, Kurt, H., Jia, J., Shigesato, Y. & Ow-Yang, C. W. with permission of Springer.

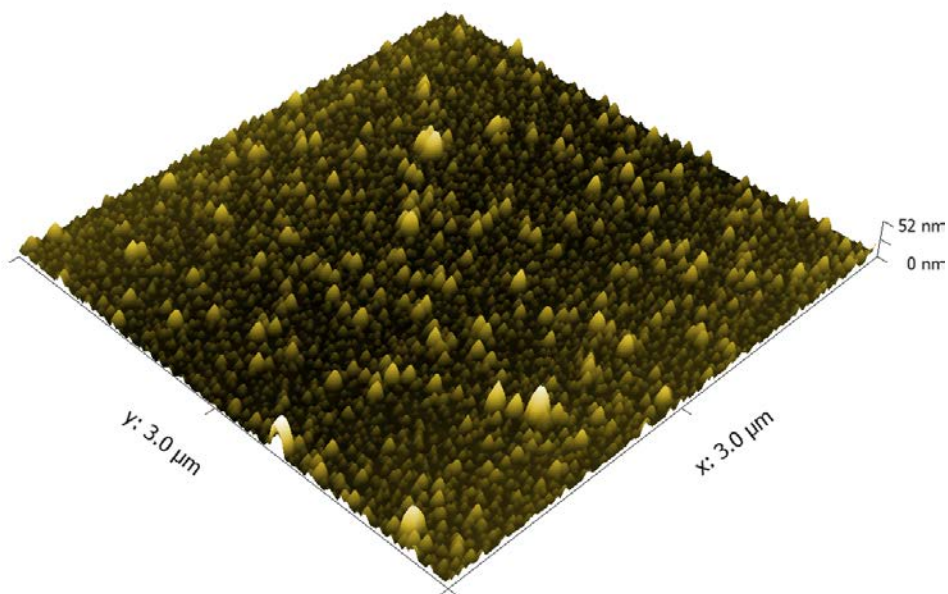


Figure 22. 3D AFM image of 3x sol-LiF deposition on ITO, with 5.6% surface coverage. Reprinted from *J. Mater. Sci. Mater. Electron.* Tuning hole charge collection efficiency in polymer photovoltaics by optimizing the work function of indium tin oxide electrodes with solution-processed LiF nanoparticles 2015, 9205–9212, Kurt, H., Jia, J., Shigesato, Y. & Ow-Yang, C. W. with permission of Springer.

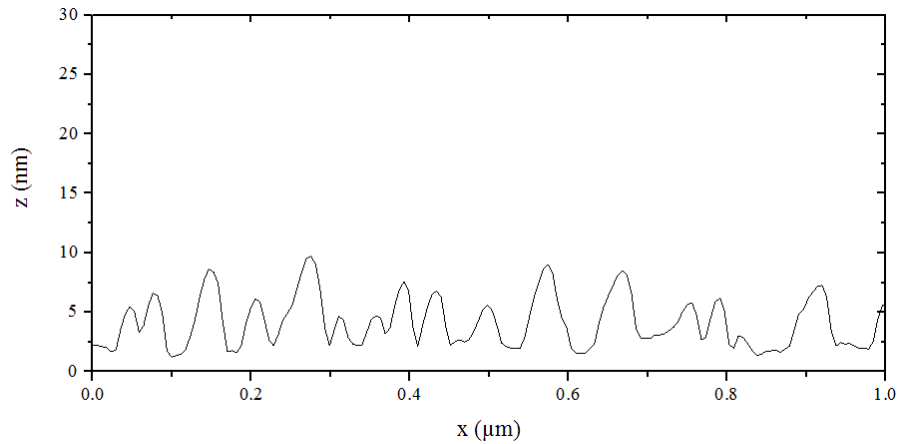


Figure 23. AFM line profile of 3x sol-LiF deposition on ITO, with 5.6% surface coverage. Reprinted from *J. Mater. Sci. Mater. Electron.* Tuning hole charge collection efficiency in polymer photovoltaics by optimizing the work function of indium tin oxide electrodes with solution-processed LiF nanoparticles 2015, 9205–9212, Kurt, H., Jia, J., Shigesato, Y. & Ow-Yang, C. W. with permission of Springer.

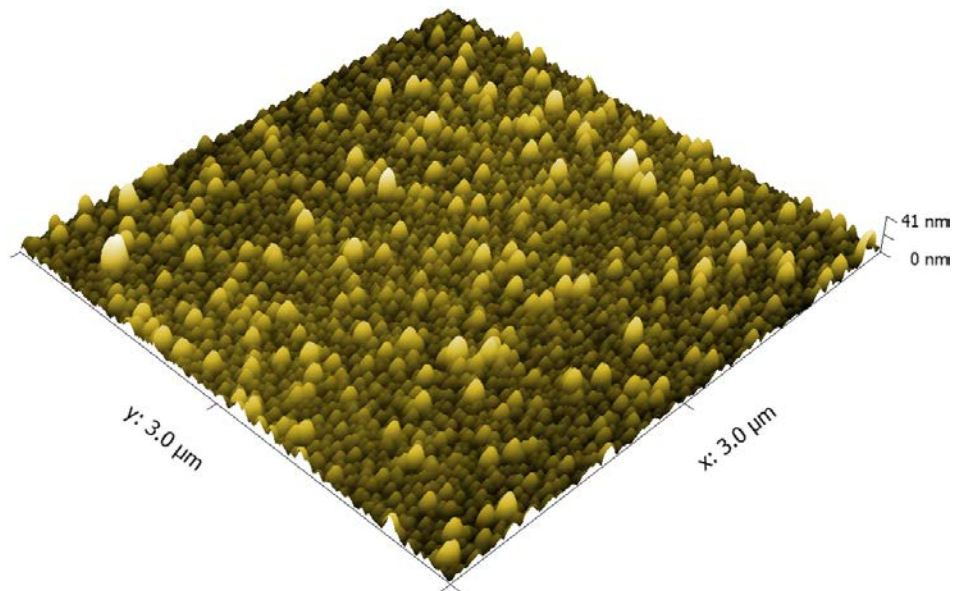


Figure 24. 3D AFM image of 5x sol-LiF deposition on ITO, with 8.7% surface coverage. Reprinted from *J. Mater. Sci. Mater. Electron.* Tuning hole charge collection efficiency in polymer photovoltaics by optimizing the work function of indium tin oxide electrodes with solution-processed LiF nanoparticles 2015, 9205–9212, Kurt, H., Jia, J., Shigesato, Y. & Ow-Yang, C. W. with permission of Springer.

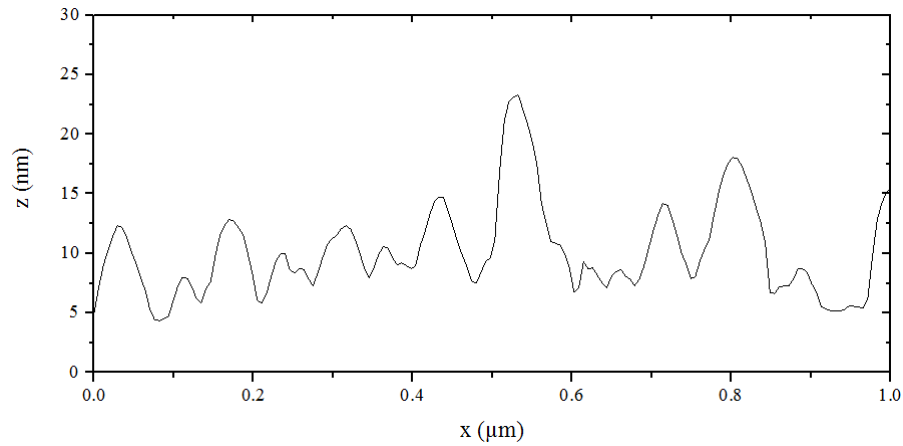


Figure 25. AFM line profile of 5x sol-LiF deposition on ITO, with 8.7% surface coverage. Reprinted from *J. Mater. Sci. Mater. Electron.* Tuning hole charge collection efficiency in polymer photovoltaics by optimizing the work function of indium tin oxide electrodes with solution-processed LiF nanoparticles 2015, 9205–9212, Kurt, H., Jia, J., Shigesato, Y. & Ow-Yang, C. W. with permission of Springer.

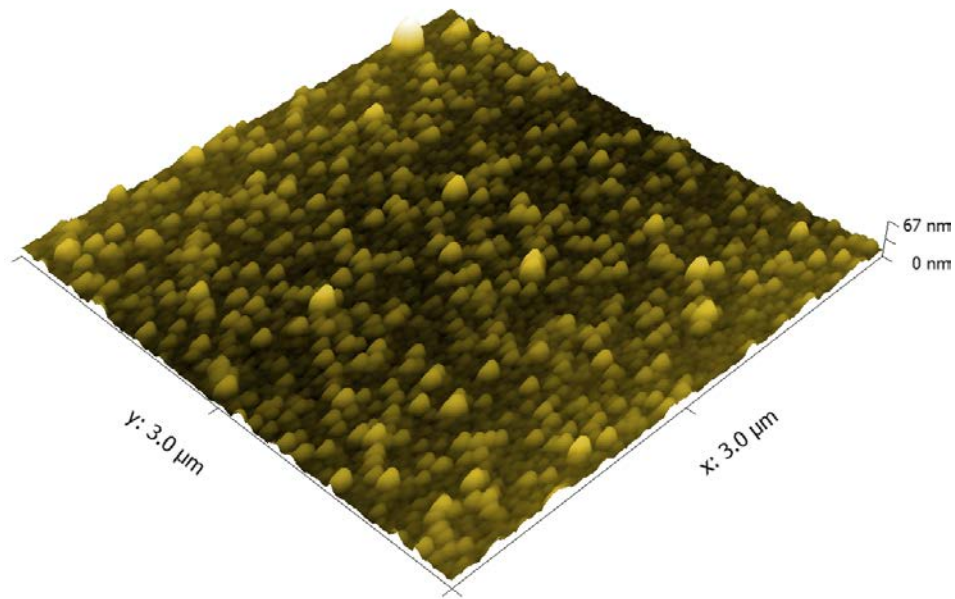


Figure 26. 3D AFM image of 7x sol-LiF deposition on ITO, with 10.1% surface coverage. Reprinted from *J. Mater. Sci. Mater. Electron.* Tuning hole charge collection efficiency in polymer photovoltaics by optimizing the work function of indium tin oxide electrodes with solution-processed LiF nanoparticles 2015, 9205–9212, Kurt, H., Jia, J., Shigesato, Y. & Ow-Yang, C. W. with permission of Springer.

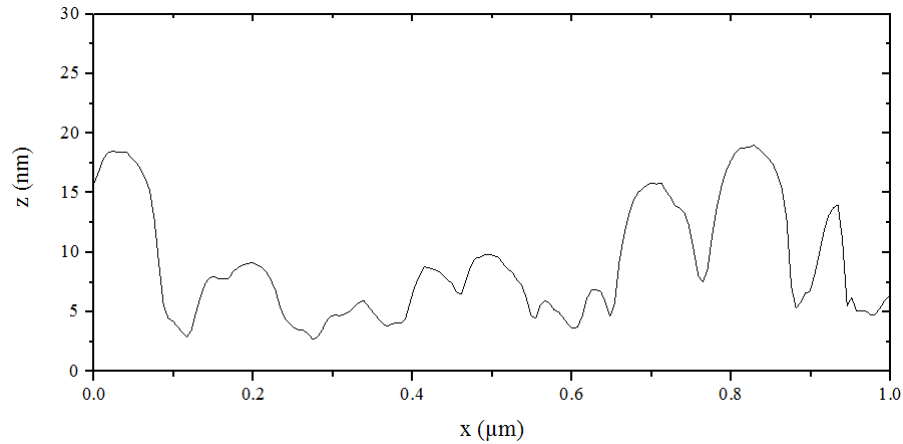


Figure 27. AFM line profile of 7x sol-LiF deposition on ITO, with 10.1% surface coverage. Reprinted from *J. Mater. Sci. Mater. Electron.* Tuning hole charge collection efficiency in polymer photovoltaics by optimizing the work function of indium tin oxide electrodes with solution-processed LiF nanoparticles 2015, 9205–9212, Kurt, H., Jia, J., Shigesato, Y. & Ow-Yang, C. W. with permission of Springer.

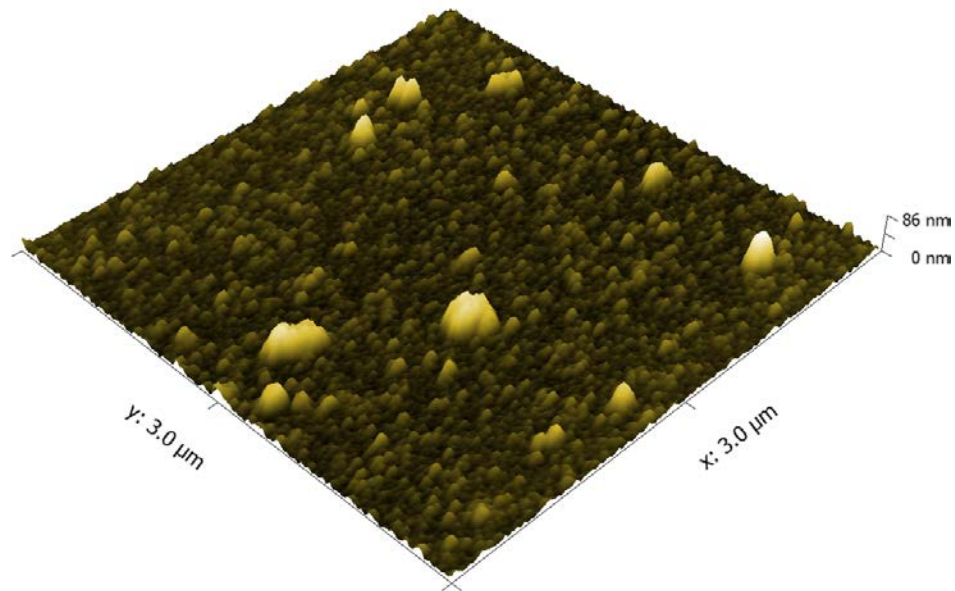


Figure 28. 3D AFM image of 10x sol-LiF deposition on ITO, with 13.2% surface coverage. Reprinted from *J. Mater. Sci. Mater. Electron.* Tuning hole charge collection efficiency in polymer photovoltaics by optimizing the work function of indium tin oxide electrodes with solution-processed LiF nanoparticles 2015, 9205–9212, Kurt, H., Jia, J., Shigesato, Y. & Ow-Yang, C. W. with permission of Springer.

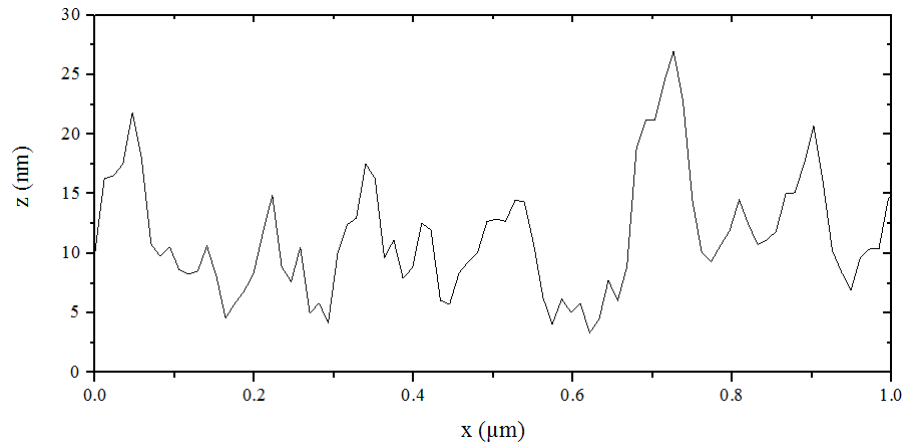


Figure 29. AFM line profile of 10x sol-LiF deposition on ITO, with 13.2% surface coverage. Reprinted from *J. Mater. Sci. Mater. Electron.* Tuning hole charge collection efficiency in polymer photovoltaics by optimizing the work function of indium tin oxide electrodes with solution-processed LiF nanoparticles 2015, 9205–9212, Kurt, H., Jia, J., Shigesato, Y. & Ow-Yang, C. W. with permission of Springer.

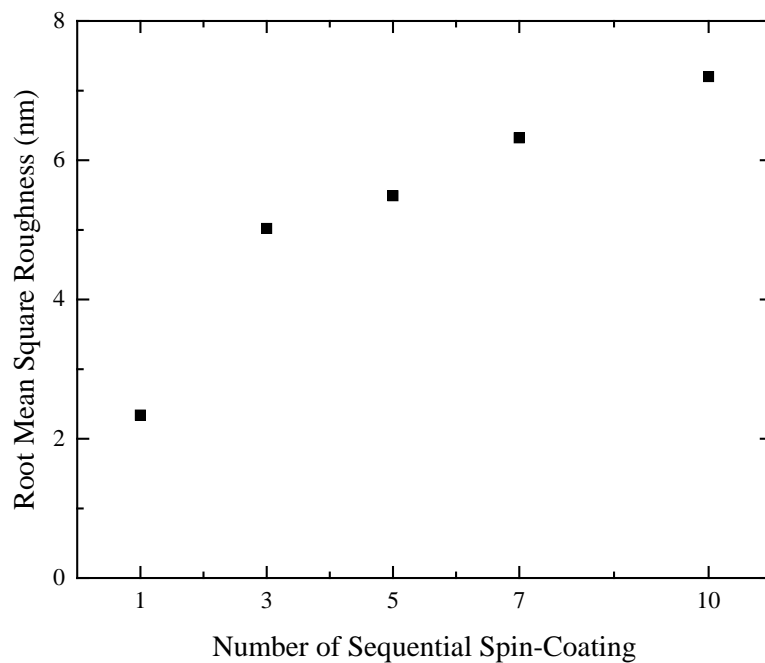


Figure 30. RMS Roughness of the sol-LiF modified ITO-coated glass versus the number of sequential spin-coating of sol-LiF dispersion. Reproduced from *J. Mater. Sci. Mater. Electron.* Tuning hole charge collection efficiency in polymer photovoltaics by optimizing the work function of indium tin oxide electrodes with solution-processed LiF nanoparticles 2015, 9205–9212, Kurt, H., Jia, J., Shigesato, Y. & Ow-Yang, C. W. with permission of Springer.

The sequential spin coating of sol-LiF on ITO coated substrates increased the root mean squared roughness from 1 nm up to 7 nm. Initial single deposition increased the RMS roughness over 2 nm directly. However, follow up depositions show a linear increase with lower slope than the initial deposition as shown in Figure 30. In the case of sol-Au deposition, the roughness increased to 2 nm level with a single deposition.

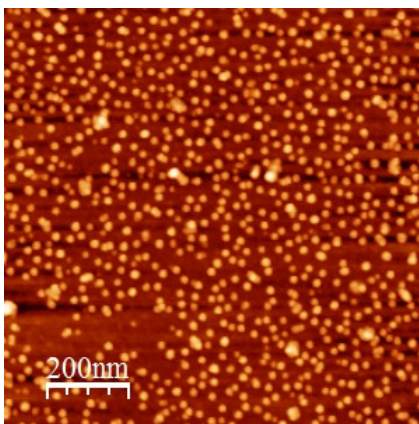


Figure 31. AFM image of sol-Au deposition on Si.

2.3.3. PESA measurements of sol-LiF modified ITO surfaces

Photoelectron emission yield spectroscopy was implemented to determine the surface work function of the sol-LiF modified ITO substrates. Since ITO is a degenerate n-type semiconductor owing to its highly doped nature, the electron band structure can be modelled as a metal. In order to analyze the photoelectron yield, square root of the yield was linearly fitted against the surface work function energy (the difference between energy of incident photons and kinetic energy of the electrons escaped from the surface).^[38] Extrapolated onset of the linear fit represents the energy needed for an electron to escape from the surface of the substrate.

Unlike photoelectron spectroscopy, PESA measurements can be carried out in ambient air conditions rather than high and ultra-high vacuum conditions. Surface work function measurements yield different results in vacuum conditions due to higher surface specific electron distributions. PESA provides a suitable characterization option to evaluate the work function of the relevant surfaces for ambient air conditions where they are fabricated and operated.

PESA measurements showed that unmodified ITO surface has a surface work function of 4.87 eV. Single deposition of sol-LiF nanoparticles increased the surface work function to 4.96 eV. Sequential depositions linearly increased the surface work function up to 5.30 eV at 10 deposition cycles.

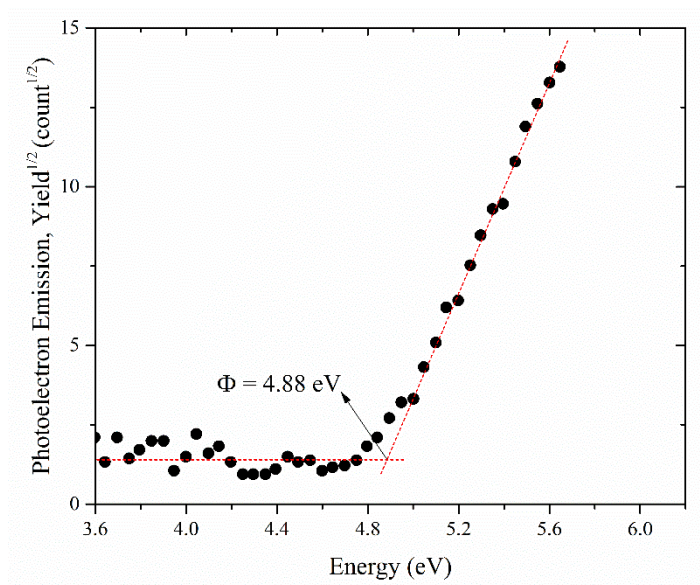


Figure 32. Photoelectron emission yield vs energy diagram for bare ITO surface. Reproduced from *J. Mater. Sci. Mater. Electron.* Tuning hole charge collection efficiency in polymer photovoltaics by optimizing the work function of indium tin oxide electrodes with solution-processed LiF nanoparticles 2015, 9205–9212, Kurt, H., Jia, J., Shigesato, Y. & Ow-Yang, C. W. with permission of Springer.

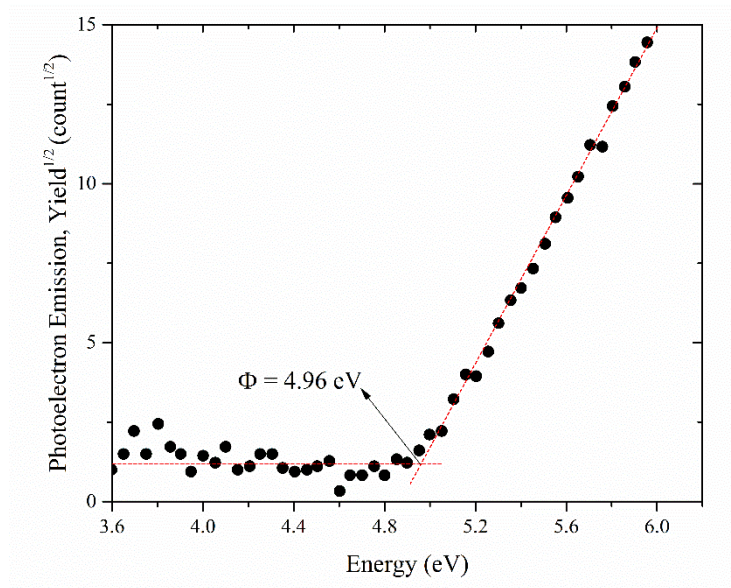


Figure 33. Photoelectron emission yield vs energy diagram for 1x sol-LiF (2% surface coverage) modified ITO surface. Reproduced from *J. Mater. Sci. Mater. Electron.* Tuning hole charge collection efficiency in polymer photovoltaics by optimizing the work function of indium tin oxide electrodes with solution-processed LiF nanoparticles 2015, 9205–9212, Kurt, H., Jia, J., Shigesato, Y. & Ow-Yang, C. W. with permission of Springer.

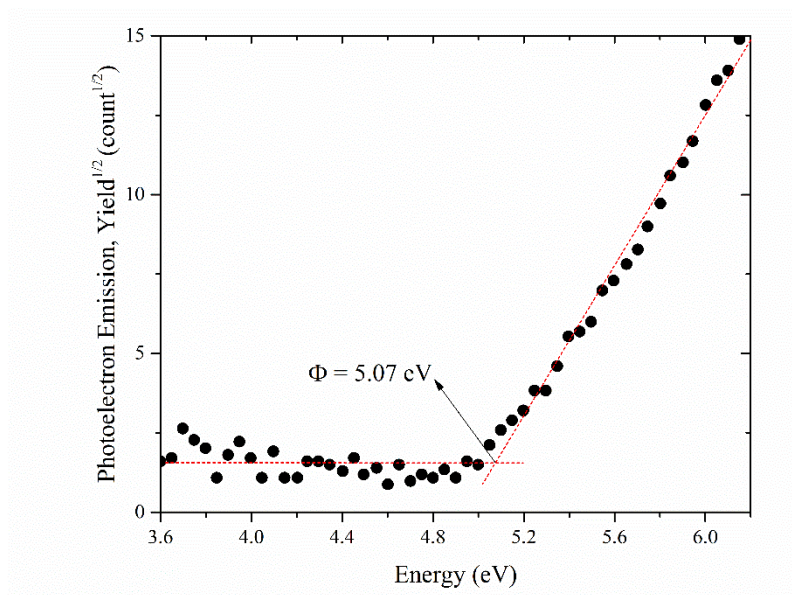


Figure 34. Photoelectron emission yield vs energy diagram for 3x sol-LiF (5.6% surface coverage) modified ITO surface. Reproduced from *J. Mater. Sci. Mater. Electron.* Tuning hole charge collection efficiency in polymer photovoltaics by optimizing the work function of indium tin oxide electrodes with solution-processed LiF nanoparticles 2015, 9205–9212, Kurt, H., Jia, J., Shigesato, Y. & Ow-Yang, C. W. with permission of Springer.

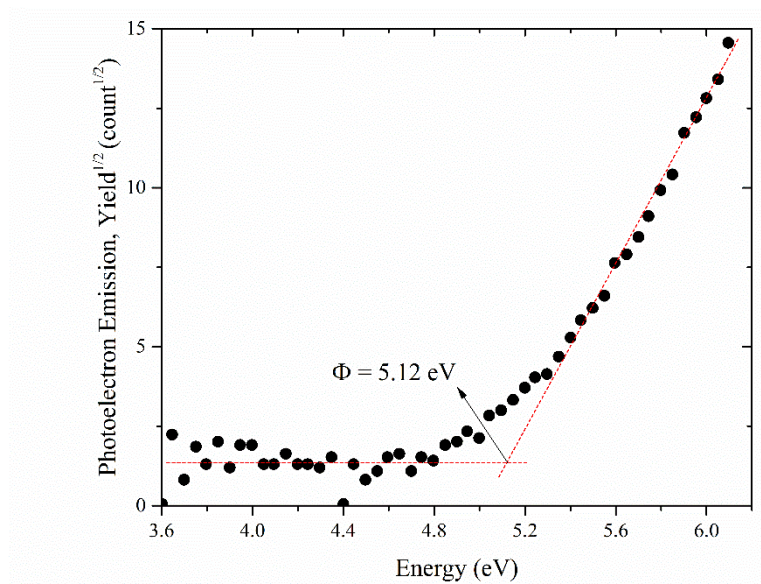


Figure 35. Photoelectron emission yield vs energy diagram for 5x sol-LiF (8.7% surface coverage) modified ITO surface. Reproduced from *J. Mater. Sci. Mater. Electron.* Tuning hole charge collection efficiency in polymer photovoltaics by optimizing the work function of indium tin oxide electrodes with solution-processed LiF nanoparticles 2015, 9205–9212, Kurt, H., Jia, J., Shigesato, Y. & Ow-Yang, C. W. with permission of Springer.

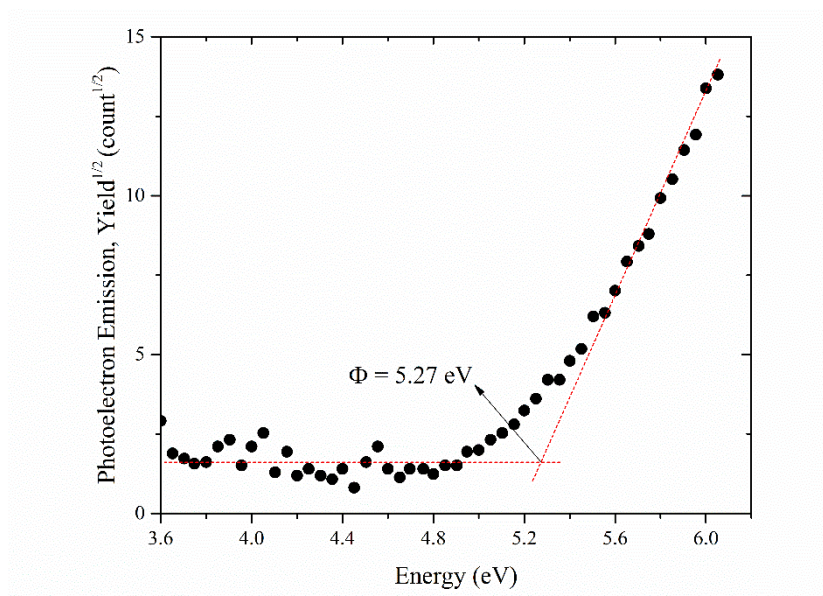


Figure 36. Photoelectron emission yield vs energy diagram for 7x sol-LiF (10.1% surface coverage) modified ITO surface. Reproduced from *J. Mater. Sci. Mater. Electron.* Tuning hole charge collection efficiency in polymer photovoltaics by optimizing the work function of indium tin oxide electrodes with solution-processed LiF nanoparticles 2015, 9205–9212, Kurt, H., Jia, J., Shigesato, Y. & Ow-Yang, C. W. with permission of Springer.

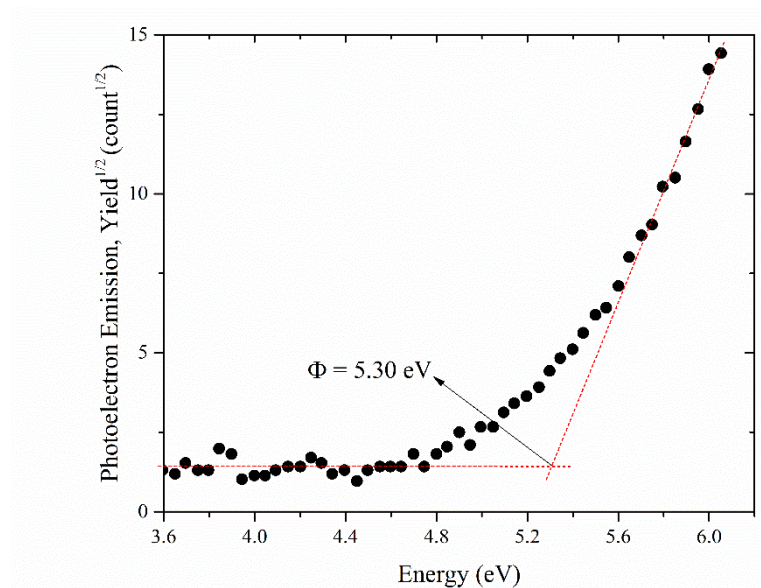


Figure 37. Photoelectron emission yield vs energy diagram for 10x sol-LiF (13.2% surface coverage) modified ITO surface. Reproduced from *J. Mater. Sci. Mater. Electron.* Tuning hole charge collection efficiency in polymer photovoltaics by optimizing the work function of indium tin oxide electrodes with solution-processed LiF nanoparticles 2015, 9205–9212, Kurt, H., Jia, J., Shigesato, Y. & Ow-Yang, C. W. with permission of Springer.

2.3.4. Sheet resistance measurements of sol-LiF and sol-Au modified ITO surfaces

The sheet resistance of the modified and unmodified ITO surfaces was evaluated using a 4-point probe equipped with a Keithley 6220 current source and a Keithley 2182A nanovoltmeter.

A significant change in sheet resistance of ITO-coated substrates was not observed for all sol-LiF and sol-Au nanoparticle depositions as shown in Table 2. Single depositions of sol-LiF and sol-Au induced a minor drop in the sheet resistance of the ITO thin film.

Table 2. Sheet Resistance of sol-LiF and sol-Au modified ITO surfaces. Reprinted from *J. Mater. Sci. Mater. Electron.* Tuning hole charge collection efficiency in polymer photovoltaics by optimizing the work function of indium tin oxide electrodes with solution-processed LiF nanoparticles 2015, 9205–9212, Kurt, H., Jia, J., Shigesato, Y. & Ow-Yang, C. W. with permission of Springer.

<i>LiF NP Surface Coverage (%)</i>	<i>Sheet Resistance of Nanostructured ITO Surface (Ω/\square)</i>
0	44.8
2.0	42.1
5.3	45.3
7.6	45.3
10.8	42.3
13.2	44.5
Sol-Au	43.1

2.3.5. Contact angle measurements of sol-LiF and sol-Au modified ITO surfaces

Water droplet contact angles of modified and unmodified ITO surfaces were investigated to evaluate the relative surface energy and hydrophobicity of the surfaces. Hydrophobicity is a crucial factor in the integrity and quality of overlaying interlayers, especially for the hole transport layer, PEDOT:PSS. All surfaces were subject to a UV-ozone treatment for cleaning and improving the hydrophilic nature of the ITO surfaces in device fabrication procedures. However, it is essential to evaluate the surface prior to the highly energetic UV-ozone treatment. Prior to UV-ozone treatments, bare ITO surface exhibits a contact angle of $75.08 \pm 0.08^\circ$. Sequential deposition of sol-LiF nanoparticles increases the water droplet contact angle above 92° level up. However, contact angle dropped to $87.86 \pm 0.17^\circ$ as the surface coverage reached 13.2%. In the case of single sol-Au deposition, the water contact angle showed a similar behavior to that of the single sol-LiF deposition and reached $96.13 \pm 0.36^\circ$.

Table 3. Water Droplet Contact Angle of sol-LiF and sol-Au nanostructured ITO surfaces before and after 30 minute of UV-ozone treatment. Reprinted from *J. Mater. Sci. Mater. Electron.* Tuning hole charge collection efficiency in polymer photovoltaics by optimizing the work function of indium tin oxide electrodes with solution-processed LiF nanoparticles 2015, 9205–9212, Kurt, H., Jia, J., Shigesato, Y. & Ow-Yang, C. W. with permission of Springer.

<i>LiF NP Surface Coverage (%)</i>	<i>Before Ozone Treatment</i>		<i>After Ozone Treatment</i>	
	<i>Water Droplet Contact Angle (deg)</i>	<i>Error (deg)</i>	<i>Water Droplet Contact Angle (deg)</i>	<i>Error (deg)</i>
0	75.08	0.08	12.64	0.05
2.0	97.82	0.20	27.33	0.05
5.3	92.59	0.99	24.37	0.05
7.6	92.95	0.29	19.31	0.10
10.8	94.33	1.54	14.59	0.04
13.2	87.86	0.17	10.43	0.04
sol-Au	96.13	0.36	15.12	0.06

Even though we had observed an increased hydrophobicity of the modified ITO surface prior to the UV-ozone treatment, 30 min of UV-ozone treatment significantly improved the hydrophilic nature of the surfaces. In particular, the surface coverage of 13.2% of sol-LiF nanoparticles showed a more hydrophilic nature than the unmodified ITO surfaces and lead to a contact angle of $10.43 \pm 0.04^\circ$. Modified ITO surfaces with sol-LiF surface coverage below 10% showed relatively high contact angles. Despite the relatively high contact angle after the UV-ozone treatment, the modified surfaces were sufficiently hydrophilic to enable high quality coverage by PEDOT:PSS overlay thin film since the contact angle values were still well below 40° .

2.3.6. FDTD Simulations of sol-Au nanostructures

An incident electric field induces collective oscillation of the free electrons on the surface of noble metals. In the case of subwavelength nanostructures like sol-Au, these collective oscillations induce a standing wave on the surface of the nanostructure. In particular, the edge or edge-like features of these nanostructures act as nodes for this standing waves and transform into poles of a dipole which can perturb and strongly focus incoming light in their vicinity.^[39] The dipoles formed can focus the incoming electric field in the near-field and also emit into the far-field like a dipole antenna.^[7] This type of strong field enhancements and antenna like behavior is desirable particularly in thin film photovoltaics with limited absorption.

FDTD simulations of sol-Au nanoparticles as hemispheres in vacuum revealed that incident plane-wave excitation was focused on the edges of the sol-Au hemispheres. As the propagation direction of the incident plane wave is oriented in the $+z$ direction, only s and p polarizations can be induced, as they are perpendicular to the propagation axis. Since the nanostructures are symmetrical along the x - and y -axes, only a single localized surface plasmon resonance (LSPR) wavelength was identified, at 532 nm. At this LSPR wavelength, the electromagnetic response field was focused on the edges of hemisphere strongly due to polarization of the free electron oscillations in the sol-Au by the polarized incident electric field. In fact, the field enhancement response amplitude was more than 10 times greater than the electric field intensity of incoming plane wave, as shown in Figure 38. The dipole formed thus simultaneously focuses the incoming electric field in the near-field and emits into the far-field like a dipole antenna.

Due to the orientation of hemisphere array (in the x - y plane) to the incoming plane wave propagating in $+z$ direction, the LSPR response was not angle-dependent. Both p -polarized and s -polarized plane waves were used for simulating nano-optical behavior resulting from unpolarized solar irradiation.

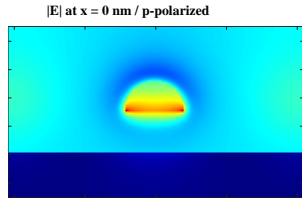


Figure 38. Electric field intensity, $|E|$, profile of sol-Au nanoparticle array at $x = 0$ (1st column), $y = 0$ (2nd column) and $z = -5$ planes (3rd column) under p -polarized (1st row), s -polarized (2nd row) and unpolarized (3rd row) 532 nm plane wave illumination in vacuum.

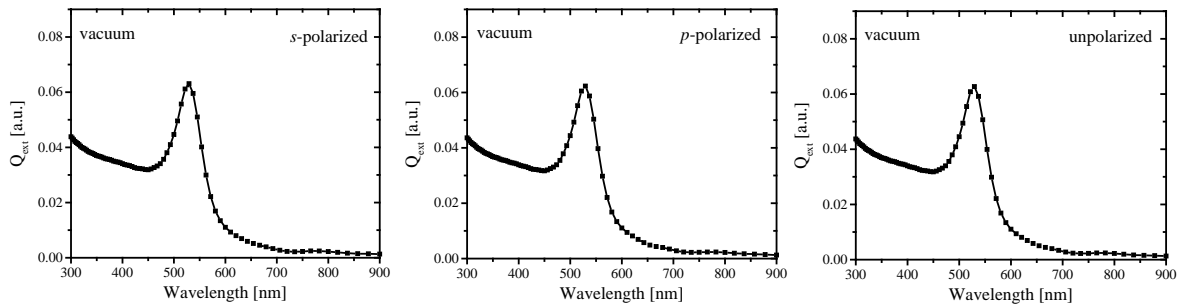


Figure 39. Extinction cross section, Q_{ext} , profile of sol-Au nanoparticle array under s -polarized (left), p -polarized (middle) and unpolarized (right) plane wave illumination in vacuum.

The combined results of *s*- and *p*-polarized plane wave excitation showed a field enhancement of 6-8 times of the electric field intensity of the incoming wave.

The next experiment in the simulation study was focused on the sol-Au hemispheres on a solid substrate, like soda lime glass. Change in the edge neighboring refractive index of sol-Au hemisphere array red-shifted the LSPR wavelength from 532 nm to 555 nm. The incoming plane wave excited the sol-Au hemisphere array from the soda lime glass side. Remarkably, the electric field enhancement surpassed 25 times with respect to the incoming *s*-polarized plane wave as shown in Figure 40.

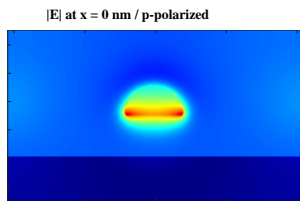


Figure 40. Electric field intensity, $|E|$, profile of sol-Au nanoparticle array at $x = 0$ (1st column), $y = 0$ (2nd column) and $z = -5$ planes (3rd column) under *p*-polarized (1st row), *s*-polarized (2nd row) and unpolarized (3rd row) 532 nm plane wave illumination on soda-lime glass.

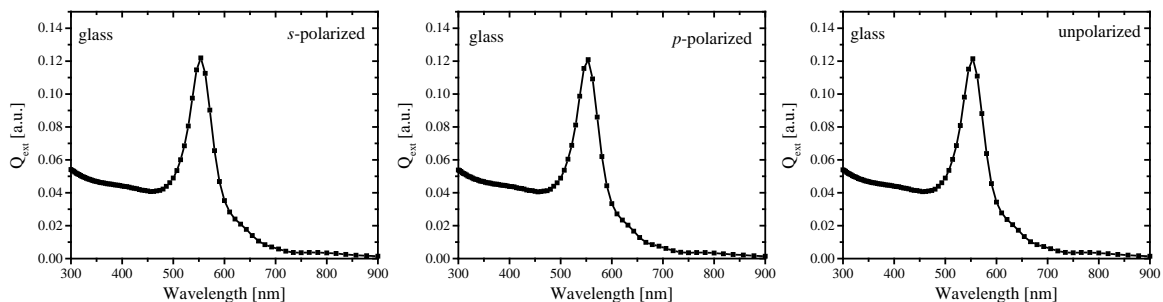


Figure 41. Extinction cross section, Q_{ext} , profile of sol-Au nanoparticle array under s -polarized (left), p -polarized (middle) and unpolarized (right) plane wave illumination on soda-lime glass substrate.

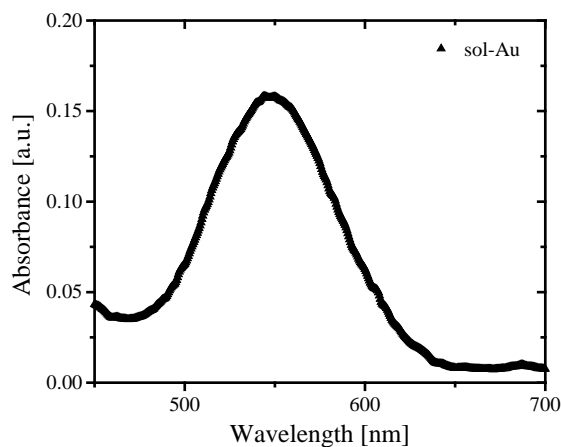


Figure 42. Absorption spectra showing the sol-Au nanoparticle response on soda lime glass substrate. H. Kurt & C.W. Ow-Yang, Impedance Spectroscopy Analysis of the photophysical dynamics due to the nanostructuring of anode interlayers in organic photovoltaics. *Physica Status Solidi A*. Copyright Wiley-VCH Verlag GmbH & Co. KGaA. Reproduced with permission.

The combined results of s - and p -polarized plane wave excitations showed the LSPR wavelength of 555 nm and field enhancement on the edge of sol-Au up to 15 times. In Figure 42, the FDTD simulations of sol-Au hemisphere arrays were consistent with the absorption spectra of fabricated sol-Au arrays on soda lime glass in terms of LSPR wavelength, but the absorption spectra showed a larger full-width-half-maximum (FWHM) due to the size distribution of sol-Au nanoparticles.

2.4. Discussion

A single layer of sol-LiF deposited on ITO substrates showed quasi-hexagonal ordering in the nanoparticle dispersion, due to a highly monodisperse DBCP micelle size, as shown in Figure 10. The average sol-LiF diameter was 9 ± 2.7 nm, while the average interparticle distance was 70.1 ± 12.2 nm. Sequential spin-coating of sol-LiF nanoparticles and oxygen plasma treatments yielded a linear increase in surface coverage by sol-LiF on ITO substrates, as shown in Figure 43. The sol-LiF layer introduced roughness on the ITO surface. For a single sol-LiF deposition, we measured a surface roughness of 2.3 nm, while 3 cycles of sequential spin-coating and etching increased the surface roughness to an RMS of 5.0 nm. Further sequential spin-coating steps increased the surface roughness less dramatically, reaching a maximum RMS of 7.2 nm for 10 iterations.

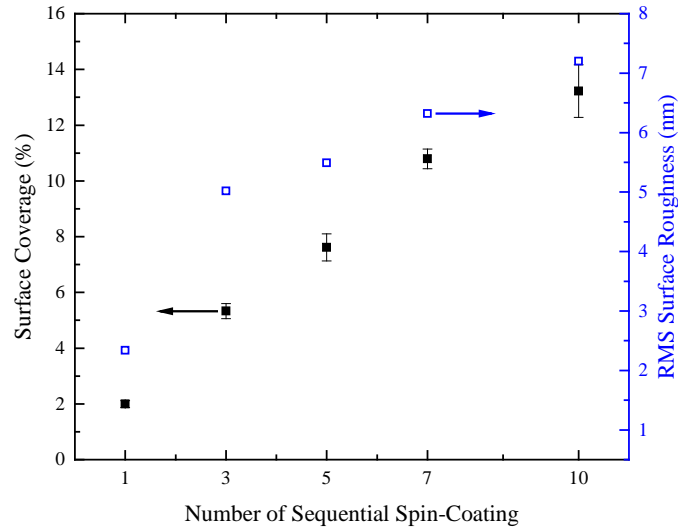


Figure 43. Correlation between sol-LiF surface coverage and surface roughness of sol-LiF modified ITO with sequential spin-coating steps. Reproduced from *J. Mater. Sci. Mater. Electron.* Tuning hole charge collection efficiency in polymer photovoltaics by optimizing the work function of indium tin oxide electrodes with solution-processed LiF nanoparticles 2015, 9205–9212, Kurt, H., Jia, J., Shigesato, Y. & Ow-Yang, C. W. with permission of Springer.

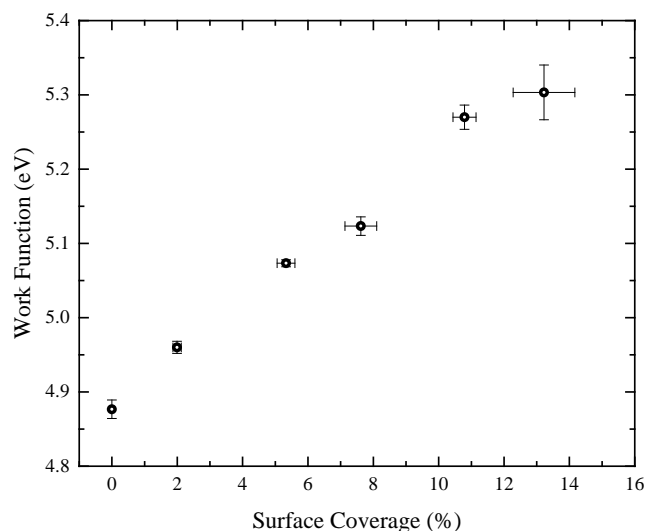


Figure 44. Correlation between surface work function of ITO, Φ , and surface coverage of sol-LiF nanostructures on ITO. Reproduced from *J. Mater. Sci. Mater. Electron.* Tuning hole charge collection efficiency in polymer photovoltaics by optimizing the work function of indium tin oxide electrodes with solution-processed LiF nanoparticles 2015, 9205–9212, Kurt, H., Jia, J., Shigesato, Y. & Ow-Yang, C. W. with permission of Springer.

The Φ of sol-LiF-modified ITO increased with the sol-LiF surface coverage, as shown in Figure 44. Bare ITO substrates were exposed to an oxygen plasma treatment of the same duration and conditions as substrates with a single sol-LiF deposition and had a measured surface work function of 4.88 eV. To tune the Φ of the ITO surface by controlling the ITO surface coverage by sol-LiF, we carried out a sequential alternation of sol-LiF-loaded micelle deposition and etch removal up to 10 times (i.e., 13.2% coverage), modifying Φ up to 5.30 eV.

The FDTD simulations of the LSPR response of sol-Au interlayers were consistent with the experimentally measured extinction cross-section (Q_{ext}) in Figure 41 and Figure 42. The hemispherical shape of the sol-Au interlayers showed angle-independent electric field enhancement of 8 times in vacuum and 15 times on a glass substrate. The LSPR wavelength was shifted from 532 nm in vacuum to 555 nm on soda lime glass substrate. Due to relatively high interparticle distance and small nanoparticle size, we did not observe hybridization or collective interaction of LSPR modes of sol-Au quasi-array. Even though high field enhancement factors was limited to the edges of the sol-Au nanostructures, the

sol-Au interlayers located at the ITO-PEDOT:PSS interface may still improve light trapping and enhance charge generation in an OPV, due to the thin nature of the active layers and PEDOT:PSS interlayer. This issue will be addressed in the next chapter.

Due to relatively low surface coverage of sol-LiF, the sheet resistance of sol-LiF modified ITO surfaces did not deviate significantly from the control substrates. However, hydrophobicity of ITO surface increased, as it can be comprehended from the increase of water contact angle from 75.08° to 97.82° for single deposition of sol-LiF. A similar behavior was observed from the single sol-Au depositions. Water contact angle of sol-LiF modified ITO surfaces gradually decreased to 87.86° as the surface coverage reaches to 13.2% for ten sequential depositions. After UV-ozone treatment, the hydrophilicity of sol-LiF and control ITO surfaces improved. The high concentration of oxygen radicals generated in UV-ozone process had increased the oxygen content of the modified and unmodified surfaces, as evidenced by the decrease in water contact angle by 3° in the sol-Au interlayers. On the other hand, low surface coverages of sol-LiF still exhibited relatively higher water contact angle, in comparison to control samples. However, all of the values measured were still suitable for depositing a conformal PEDOT:PSS hole transport overlayer.

2.5. Summary and Concluding Remarks

By using a diblock copolymer-based self-assembly technique, we produced sol-LiF and sol-Au nanoparticle dispersions on various surfaces. Among these surfaces, the ITO thin film-coated glass substrates were noteworthy due to their being commonly used in photovoltaic applications. We have characterized the sol-LiF and sol-Au deposited surfaces thoroughly. Consistent with the literature,^[29] our findings revealed that sol-LiF depositions can increase the work function of the deposited ITO thin film, in addition to tuning the surface work function of ITO by adding sequential depositions of the sol-LiF. Furthermore, we have improved the uniformity of sol-LiF dispersion at higher deposition cycles, addressed the limitations of surface roughness below 8 nm, and reached a higher degree of surface coverage to achieve a surface work function of -5.30 eV. Work function tuning could

provide a solution to address the problem of low hole collection efficiency in organic photovoltaics, which are hampered by the energy mismatch at the anodic interface.

Additionally, we have shown that sol-Au nanoparticles can induce an electric field enhancement in the close vicinity of their surfaces. For implementation in thin film photovoltaics, the improvement in absorption of sub-100 nm active layers is indeed compelling, particularly if we consider that this spectral response can be tuned by *i*) particle size and *ii*) array geometry.^[40] Thus the tunability offered by nanostructuring at the ITO surface with sol-Au could improve the spectral overlap between the re-emission spectrum and the absorption spectrum of organic donor polymers in photovoltaic device efficiencies.

It should be noted that our hypothesis for the study described in this chapter was that the ITO anode surface properties could be tuned by modifying the interlayer surface coverage with size monodisperse dielectric and plasmonic nanostructures. In light of our results, we have validated our hypothesis on the tunability of the ITO anode behavior by two approaches. Monodisperse and quasi-ordered sol-LiF and sol-Au nanostructures on ITO surfaces could indeed tune the work function and optical properties of ITO anode, respectively. It provides a stepping stone for our next chapter focusing on the hypothesis that these solution-processed functional nanostructures could improve the organic photovoltaic performance

Chapter 3: Incorporation of Nanostructured ITO Electrodes into Organic Photovoltaics

3.1. Introduction

The hypothesis that we had addressed in the focused study in this chapter was that nanostructuring would enhance BHJ OPV device performance efficiency. In the case of sol-LiF modified ITO anodes, the tunability of surface work function energy would enable optimizing the energy level to align better with the HOMO of the organic donor. In the case of sol-Au modified ITO anodes, the tunability of the LSPR emission response would facilitate better matching with the spectral profile of external quantum efficiency (EQE). For our methodology, we have incorporated the nanostructured interlayers into BHJ OPV devices based on two different types of BHJ polymer blends with significantly dissimilar highest occupied molecular orbital (HOMO) levels, and analyzed the *J-V* and EQE device characteristics. Furthermore, we performed finite difference time domain (FDTD) simulations, in order to compare the induced field enhancement with the EQE profiles for both types of BHJ polymer blends.

Due to the low compatibility between intrinsically different structures at the molecular level, organic-inorganic interfaces often result in recombination losses due to low charge carrier mobility and limited charge carrier lifetimes.^[8] By improving matching of the electronic structure at the low work function (Φ) electrode interface, mobile hole extraction can be increased, thereby lowering recombination losses and enhancing the electronic hole contribution to the current density. In this context, the surface energy and Φ of the electrode, typically of tin-doped indium oxide (ITO) in conventional BHJ device architectures, are key factors determining the overall device performance.

To tune the properties of the electrode/active layer interface, a panoply of approaches have been adopted^[9]—self-assembled monolayers,^[10–12] and chlorine surface modification;^[13] organic layers;^[14–16] carbon-based nanomaterials;^[17,18] transition-metal oxides;^[19–23] and alkali halides such as CsF and LiF.^[24] Interlayer engineering (IE) enables not only the tuning of charge collection efficiency and charge selectivity on both electrodes, but also control over OPV stability and durability. An additional parameter for tuning at the high Φ

electrode is PEDOT:PSS, which is commonly used as an electronic hole transport/electron-blocking layer. Considering the low electronic homogeneity^[25] and the low-pH nature of PEDOT:PSS, the interface it forms with ITO offers limited electron-blocking capability,^[26] as well as chemical instability leading to Indium diffusion into active layers.^[27] The scope of this chapter herein is focused on interface engineering of the ITO/PEDOT:PSS interlayer in P3HT:PC₆₀BM and PCDTBT:PC₇₀BM BHJ photovoltaic devices, through tuning charge collection efficiency by sol-LiF nanostructuring, and improvement of active layer absorption through plasmonic response of sol-Au nanostructures on ITO.

We have observed that varying the surface coverage of sol-LiF nanoparticles offer additional tunability for the ITO surface Φ , suggesting that device performance can be tailored by tuning the energy level alignment at the organic-inorganic interface.^[31] Moreover, incorporation of sol-Au nanoparticles significantly improve the OPV performance of P3HT:PC₆₀BM and PCDTBT:PC₇₀BM BHJ devices.

This chapter of the thesis is mainly based on our previously published works.^[30]

Reprinted and adapted from *J. Mater. Sci. Mater. Electron.* Tuning hole charge collection efficiency in polymer photovoltaics by optimizing the work function of indium tin oxide electrodes with solution-processed LiF nanoparticles 2015, 9205–9212, Kurt, H., Jia, J., Shigesato, Y. & Ow-Yang, C. W. with permission of Springer.

H. Kurt & C.W. Ow-Yang, Impedance Spectroscopy Analysis of the photophysical dynamics due to the nanostructuring of anode interlayers in organic photovoltaics. *Physica Status Solidi A*. Copyright Wiley-VCH Verlag GmbH & Co. KGaA. Reproduced with permission.

3.2. Experimental

3.2.1 Materials

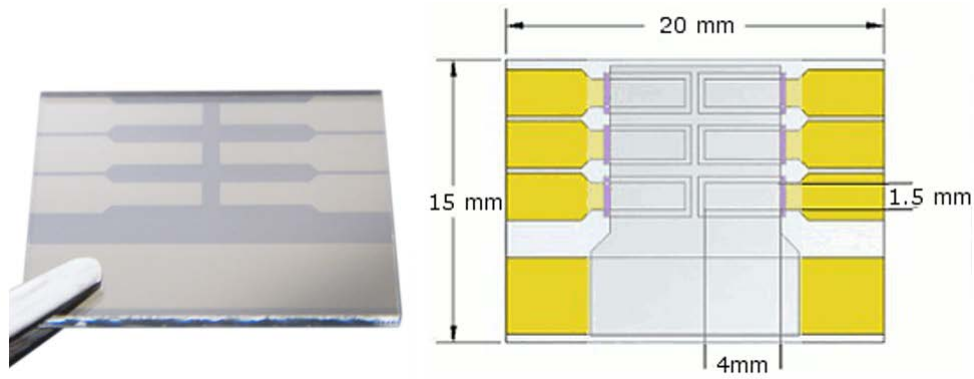


Figure 45. ITO coated pixelated anode glass substrates (left) and relevant dimensions (right)

100 nm ITO coated pixelated anode glass substrates with 20 mm × 15 mm lateral dimensions and 1.1 mm thickness were used in photovoltaic device fabrication as represented in Figure 45. Pixel dimension were 4 mm × 1.5 mm. The pixelated anodes were obtained from Ossila Ltd.

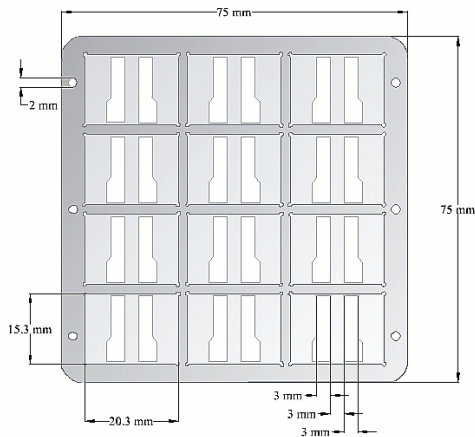


Figure 46. Aluminum cathode deposition mask.

The cathode deposition mask (V2) was purchased from Ossila Ltd and dimensions are represented in Figure 46.

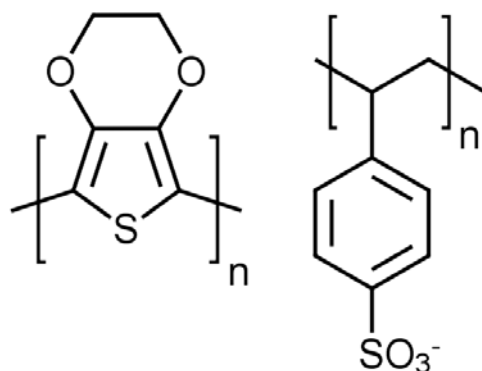


Figure 47. Chemical representation of PEDOT (left) and PSS (right) components of hole transport layer.

PEDOT:PSS (Heraeus Clevios™ P VP AI 4083, 1:6 ratio, Figure 47) solution was purchased from Ossila Ltd. and used as the hole transporting layer over ITO anode substrate.

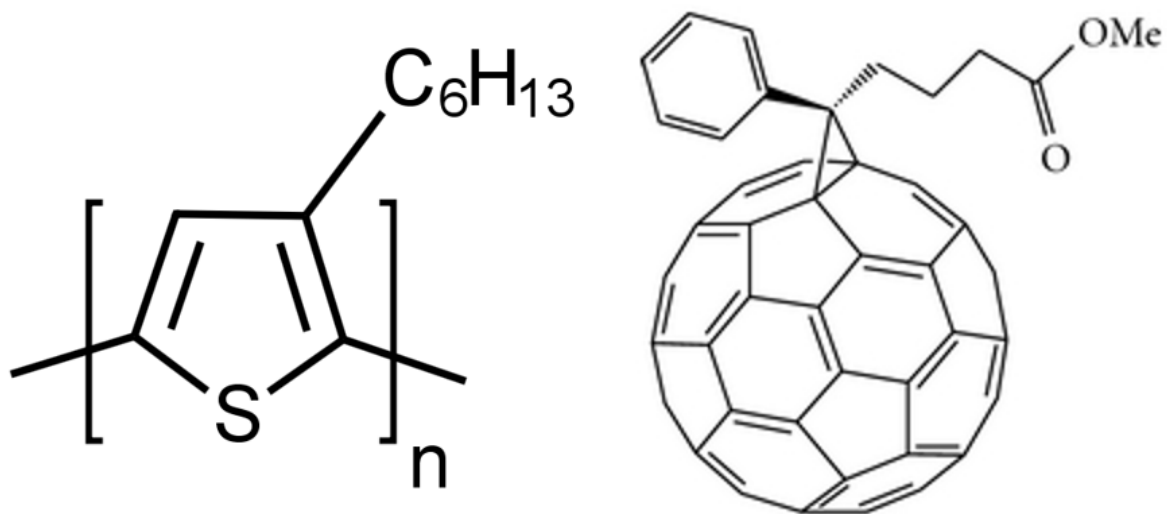


Figure 48. Chemical structure of P3HT (left) and PC₆₀BM (right)

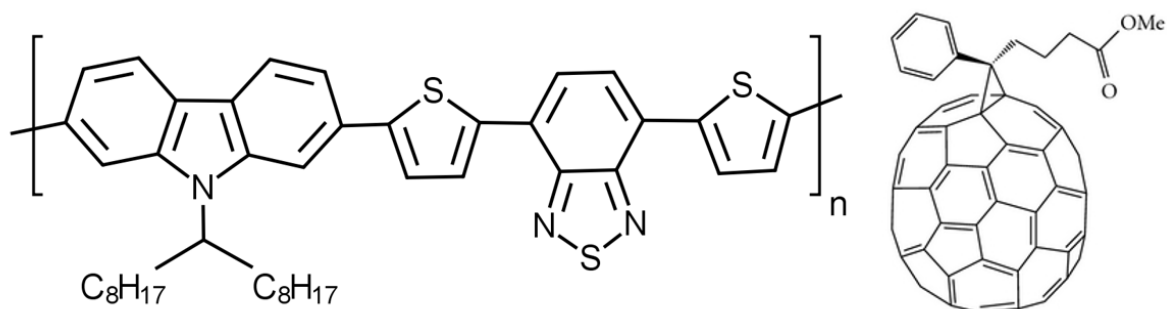


Figure 49. Chemical structure of PCDTBT (left) and PC₇₀BM (right)

Regioregular poly(3-hexylthiophene-2,5-diyl) (P3HT, M103, M_w 65200, 95.7% regioregular, Ossila Ltd, Sheffield, UK), poly[N-9'-heptadecanyl-2,7-carbazole-alt-5,5-(4',7'-di-2-thienyl-2',1',3'-benzothiadiazole)] (PCDTBT, M137, M_w 42000, Ossila Ltd, Sheffield, UK), [6,6]-phenyl-C₆₁-butyric acid methyl ester (PC₆₀BM, 99%, M111, Ossila Ltd, Sheffield, UK) and [6,6]-phenyl-C₇₁-butyric acid methyl ester (PC₇₀BM, 95%, M113, Ossila Ltd, Sheffield, UK) were used active layer materials in bulk heterojunction photovoltaic devices. 0.45 μm PTFE syringe filters (Acrodisc Syringe filters) were obtained from Pall GmbH, Dreieich, Germany. Lithium fluoride (LiF, 99.99%, Aldrich) and Aluminum evaporation slugs (Al, 99.999%, Aldrich) were used as thermal evaporation source materials for cathode deposition.

3.2.2. Fabrication and device characterization of P3HT:PC₆₀BM solar cells

Pixelated ITO anode substrates with and without sol-LiF nanoparticles were sonicated in acetone, methanol and isopropanol baths for 10 min each with polypropylene substrate rack. The cleaned substrates were transferred to clean room within fresh isopropanol bath. Prior to photovoltaic fabrication, the substrates were treated with UV-ozone treatment (UV Ozone Cleaner – Procleaner[™], Bioforce Nanosciences Holdings Inc., Ames, IA, USA) for 30 minutes.

PEDOT:PSS solution was filtered using 0.45 μm PTFE syringe filters prior to spin coating deposition to remove aggregates. Approximately 40 nm thick PEDOT:PSS thin film was

deposited by spin-coating speed of 5000 rpm on pixelated ITO anode substrates and annealed at 150 °C for 15 min. P3HT and PC₆₀BM (Ossila M111, Sheffield, UK; 99%) were mixed in a 1:0.6 weight ratio in chlorobenzene. P3HT:PC₆₀BM (25 mg/mL) solution was deposited by spin-coating at 2000 rpm for 60 s, resulting in a ~90 nm thick layer. Layer thicknesses were measured using a surface profiler (KLA-Tencor P6, Milpitas, CA, USA). The samples were thermally annealed at 150 °C for 10 min. and immediately transferred to a thermal evaporator chamber and placed under high vacuum ($\sim 2 \times 10^{-6}$ mbar). To make the back-side electrical contact, we performed thermal evaporation of a 1.2 nm-thick LiF layer, followed by a 100 nm-thick Al cathode layer on the organic active layers. The samples were then annealed at 150 °C for 10 min. after cathode evaporation. The devices were subsequently encapsulated using UV-curable epoxy (Ossila E131, Sheffield, UK).

The final device structure produced was composed of the following layer sequence: ITO/sol-LiF interlayer/PEDOT:PSS/P3HT:PC₆₀BM/LiF/Al, where the sol-LiF interlayer was deposited by sequentially spin-coating and plasma etching 1, 3, 5, 7 and 10 times. The device size for each cell was 0.045 cm². We measured the current density-voltage (*J-V*) characteristics using a source meter (Keithley Instruments Model 2400, Cleveland, OH, USA) under AM 1.5G solar irradiation at 100 mW/cm² (Newport Corporation Oriel Sol3A Class AAA 91192 Solar Simulator equipped with 450W xenon lamp, Newport, CA, USA). The light intensity was calibrated by reference Si photodiode cell.

3.2.3. Fabrication and device characterization of PCDTBT:PC₇₀BM Solar Cells

We integrated the sol-LiF interlayers into poly[N-9'-heptadecanyl-2,7-carbazole-alt-5,5-(4',7'-di-2-thienyl-2',1',3'-benzothiadiazole)]:[6,6]-Phenyl-C₇₁-butyric acid methyl ester (PCDTBT:PC₇₀BM) bulk heterojunction (BHJ) devices. Pre-patterned indium tin oxide anode substrates (ITO, Ossila S101, Sheffield, UK) with and without sol-LiF nanoparticles were sonicated in acetone, methanol and isopropanol baths for 10 min each, before 30 min. of UV-ozone treatment. A thin layer of diluted poly(3,4-ethylenedioxythiophene):polystyrene sulfonate (PEDOT:PSS, Heraeus Clevious™ PVP AI 4083, filtered at 0.45 μm) was deposited by spin-coating (6000 rpm, ~30 nm thickness) and annealed at 150 °C for 15 min. PCDTBT (Ossila M137, Sheffield, UK; M_w 42200) and

PC₇₀BM (Ossila M113, Sheffield, UK; 95%) were mixed in a 1:4 weight ratio in chlorobenzene. P3HT:PC₆₀BM (20 mg/mL) solution was deposited by spin-coating at 3000 rpm for 60 s, resulting in a ~70 nm thick layer. Layer thicknesses were measured using a surface profiler (KLA-Tencor P6, Milpitas, CA, USA). The samples were fabricated in ambient clean room conditions and immediately transferred to a thermal evaporator chamber and placed under high vacuum ($\sim 2 \times 10^{-6}$ mbar). To make the back-side electrical contact, we performed thermal evaporation of a 1.3 nm-thick LiF layer, followed by a 120 nm-thick Al cathode layer on the organic active layers. The samples were then annealed at 80°C for 15 min. after cathode evaporation. The devices were subsequently encapsulated using UV-curable epoxy (Ossila E131, Sheffield, UK).

The final device structure produced was composed of the following layer sequence: ITO/sol-LiF interlayer/PEDOT:PSS/PCDTBT:PC₇₀BM/LiF/Al, where the sol-LiF interlayer was deposited by sequentially spin-coating and plasma etching 1, 3, 5, 7 and 10 times. The device size for each cell was 0.045 cm². We measured the current density-voltage (*J-V*) characteristics using a source meter (Keithley Instruments Model 2400, Cleveland, OH, USA) under AM 1.5G solar irradiation at 100 mW/cm² (Newport Corporation Oriel Sol3A Class AAA 91192 Solar Simulator equipped with 450W xenon lamp, Newport, CA, USA). The light intensity was calibrated by reference Si photodiode cell.

3.2.4. FDTD Simulations of P3HT:PC₆₀BM and PCDTBT:PC₇₀BM Solar Cells: with and without sol-Au interlayers

In this section, sol-Au nanoparticle quasi-arrays were integrated into the device structure of thin-film organic photovoltaics as interlayers between the ITO anode and the PEDOT:PSS layers. The array of sol-Au nanoparticles were simulated again as hemispheres with a diameter of 10 nm. Refractive indices and extinction coefficients of P3HT:PC₆₀BM (1:0.6) BHJ and of PCDTBT:PC₇₀BM (1:4) BHJ were obtained from the works of Compoy-Quiles et al. and Guerrero et al.^[41,42] The optical constants of other components were used as in Section 2.2.5. The material data were prefitted into the FDTD model before the simulations were performed in Lumerical Material Explorer, as shown in Figure 50-Figure 54 .

The simulated light source was in the 350-800 nm wavelength range with a pulse length of 1.9947 femtosecond. The *x-y* cross-sectional simulation area was set to 60 nm × 104 nm

with a depth of 400 nm in the z direction as shown in Figure 55 and Figure 56. The boundary conditions used were perfectly matched layers (PML) along the propagation axis, z , and periodic boundary conditions in the x and y directions. A maximum mesh size of 0.5 nm was set in all spatial directions of the simulation region to ensure the highest resolution for the simulation. The device structure was identical to the fabricated devices. For P3HT:PC₆₀BM BHJ OPV devices, ITO (100 nm)/sol-Au interlayer/PEDOT:PSS (40 nm) /P3HT:PC₆₀BM (90 nm) /LiF (1.2 nm) /Al (100 nm) device architecture was used as shown in Figure 55. For PCDTBT: PC₇₀BM BHJ OPV devices, ITO (100 nm) /sol-Au interlayer/PEDOT:PSS (30 nm) /PCDTBT:PC₇₀BM (70 nm) /LiF (1.2 nm) /Al (120 nm) device architecture was used as shown in Figure 56.

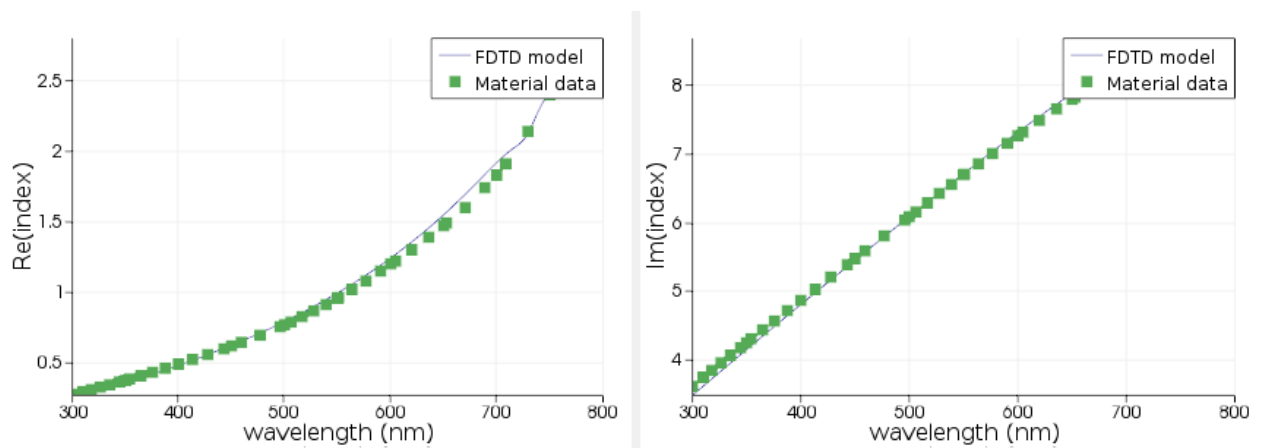


Figure 50. The FDTD model of aluminum back electrode used in the study.

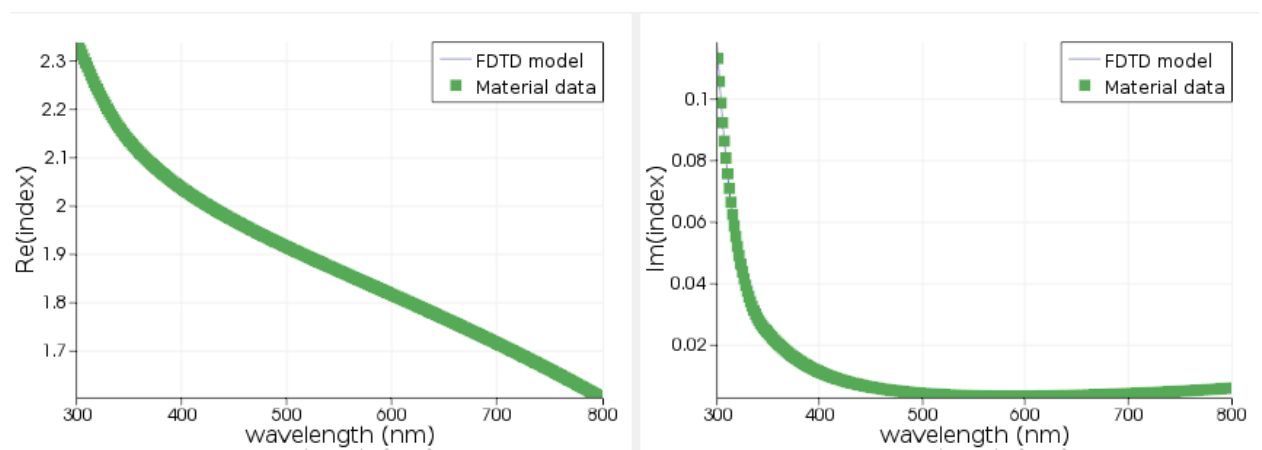


Figure 51. The FDTD model of ITO transparent electrode used in the study.

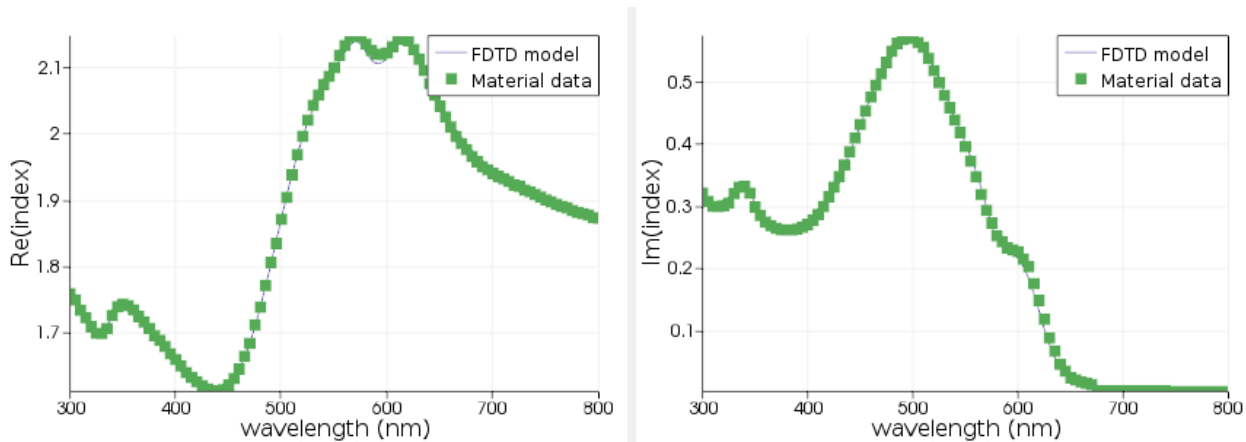


Figure 52. The FDTD model of P3HT:PC₆₀BM bulk heterojunction active layer used in the study.

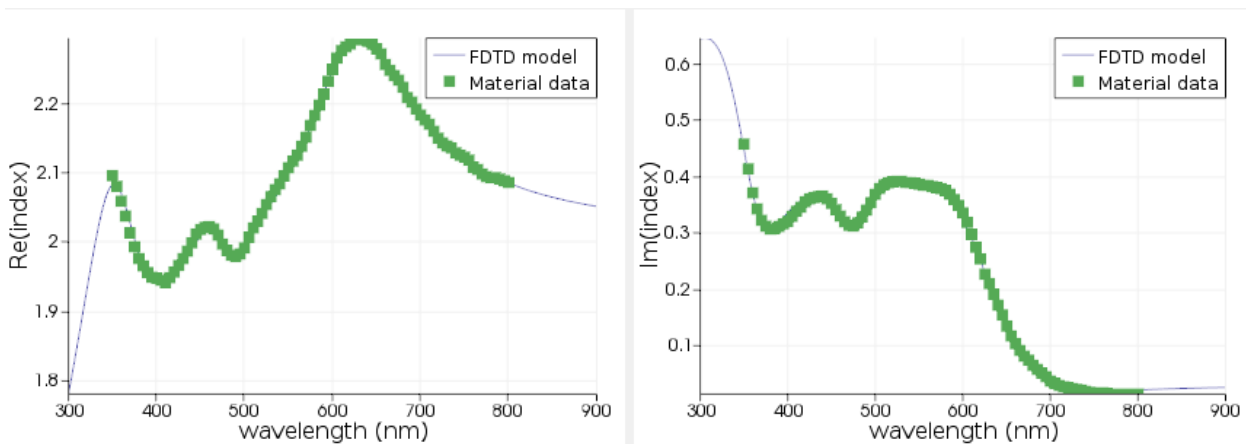


Figure 53. The FDTD model of PCDTBT:PC₇₀BM bulk heterojunction active layer used in the study.

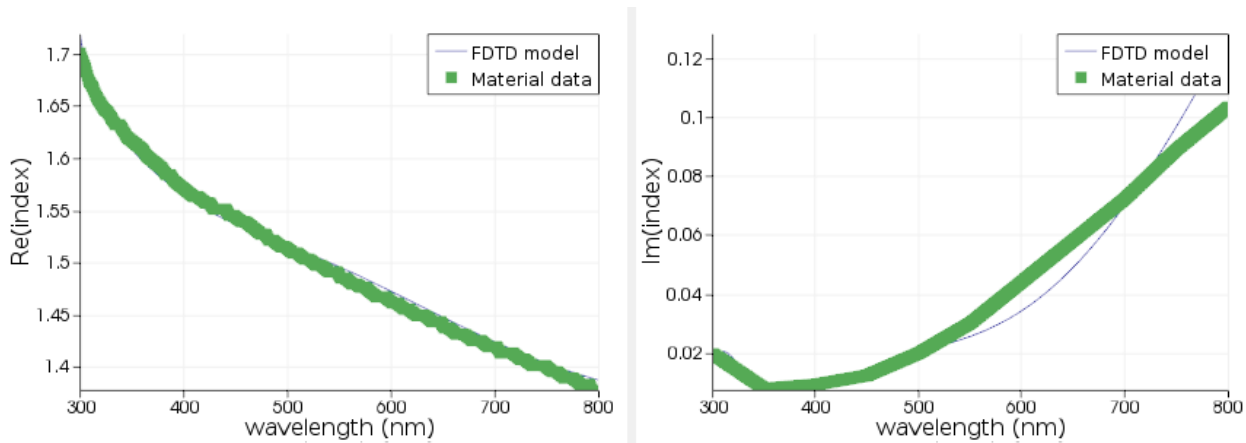


Figure 54. The FDTD model of PEDOT:PSS hole transport layer used in the study.

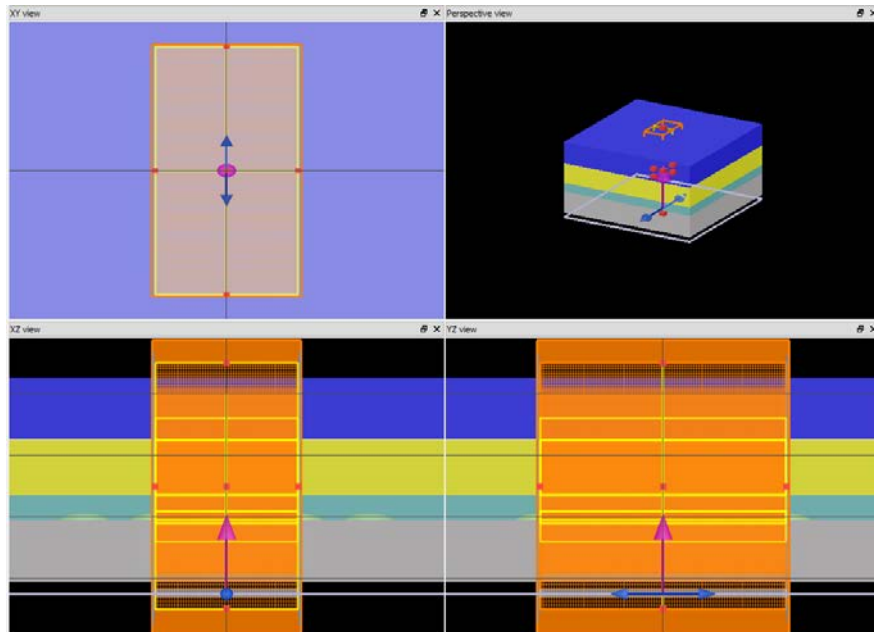


Figure 55. The FDTD simulation model used for P3HT:PC₆₀BM BHJ OPVs with sol-Au nanostructures on ITO surface. Black background represents the soda-lime glass, 100 nm thick grey layer represents the ITO anode, 40 nm thick teal layer represents the PEDOT:PSS HTL, 90 nm thick yellow layer represents the active layer, P3HT:PC₆₀BM and finally 100 nm thick blue layer represents Al cathode.

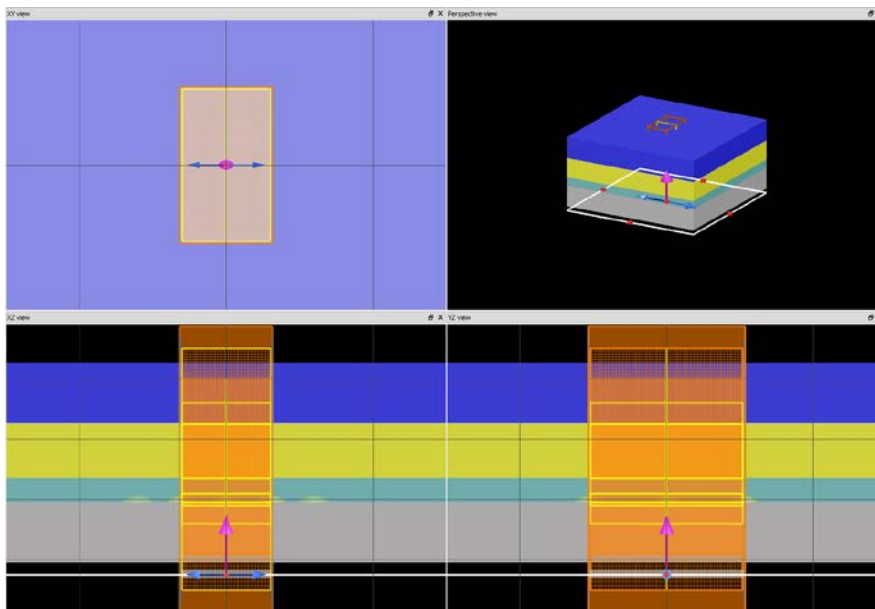


Figure 56. The FDTD simulation model used for PCDTBT:PC₇₀BM BHJ OPVs with sol-Au nanostructures on ITO surface. Black background represents the soda-lime glass, 100 nm thick grey layer represents the ITO anode, 30 nm thick teal layer represents the PEDOT:PSS HTL, 70 nm thick yellow layer represents the active layer, PCDTBT:PC₇₀BM and finally 120 nm thick blue layer represents Al cathode.

3.3. Results

3.3.1. P3HT:PC₆₀BM and PCDTBT:PC₇₀BM BHJ OPV devices with and without sol-Au interlayers

The sol-Au interlayer showed an LSPR wavelength of 532 and 555 nm in vacuum and on soda lime glass respectively. Within the P3HT:PC₆₀BM BHJ OPV device structure, the LSPR wavelength of the sol-Au interlayer red-shifted to 615 nm, due to the relatively high refractive index of ITO thin film and close proximity to the relatively high refractive index of P3HT:PC₆₀BM BHJ active layer. In Figure 57, the response electric field intensity within the device was plotted versus wavelength of the incoming plane wave excitation. The active layer, P3HT:PC₆₀BM BHJ, was positioned between $z = 35$ nm and $z = 125$ nm. The electric field intensity within the active layer surpassed that of the incident field for the wavelength range 520-700 nm. The response electric field intensity in the active layer increased with excitation closer to the LSPR wavelength as shown in Figure 58.

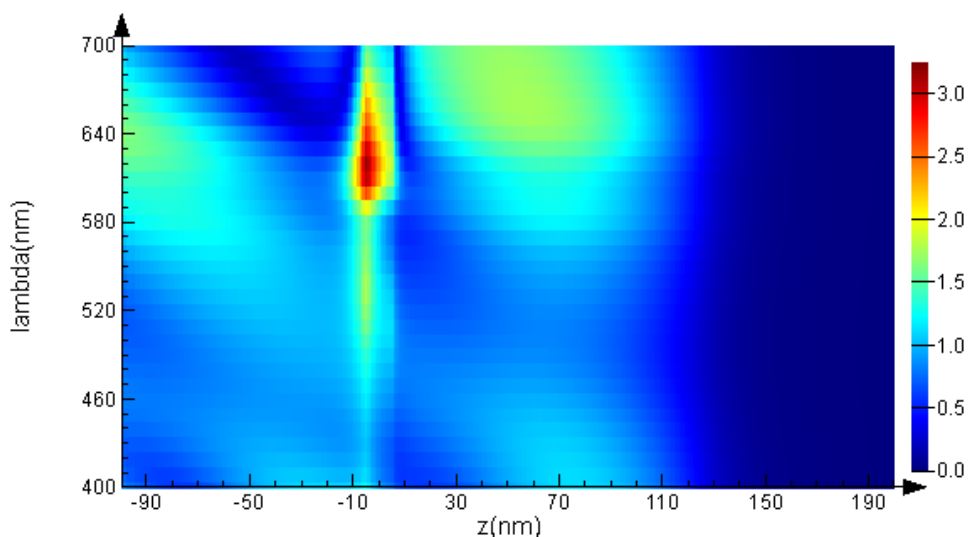


Figure 57. Electric field intensity, $|E|$, profile of propagating light in a P3HT:PC₆₀BM BHJ OPV device with a sol-Au interlayer, through the thickness from $z = -100$ nm to $z = 200$ nm and over the wavelength range between 400 nm and 700 nm. The active layer is positioned between $z = 35$ nm and $z = 125$ nm. H. Kurt & C.W. Ow-Yang, Impedance Spectroscopy Analysis of the photophysical dynamics due to the nanostructuring of anode interlayers in organic photovoltaics. *Physica Status Solidi A*. Copyright Wiley-VCH Verlag GmbH & Co. KGaA. Reproduced with permission.

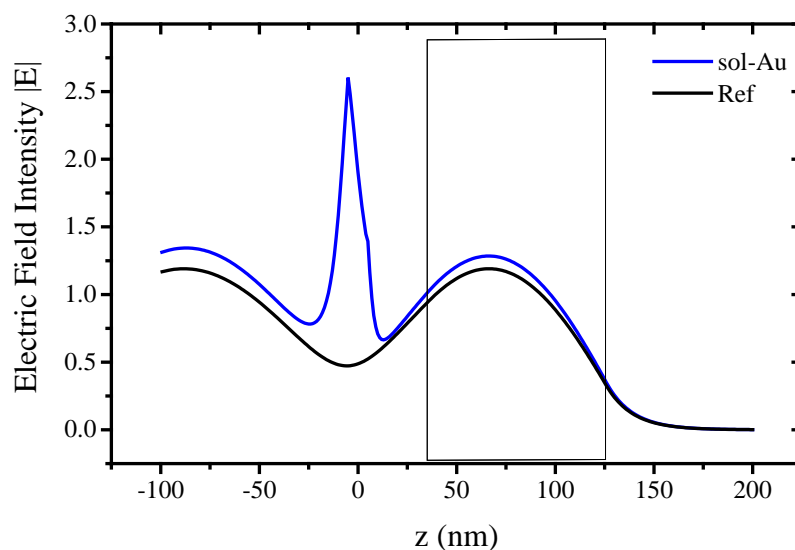


Figure 58. The induced response electric field intensity, $|E|$, profile of the propagating light in a P3HT:PC₆₀BM OPV device with sol-Au interlayer, through the thickness from $z = -100$ nm to $z = 200$ nm at the wavelength of 610 nm. The active layer is positioned between $z = 35$ nm and $z = 125$ nm and represented as shaded. H. Kurt & C.W. Ow-Yang, Impedance Spectroscopy Analysis of the photophysical dynamics due to the nanostructuring of anode interlayers in organic photovoltaics. *Physica Status Solidi A*. Copyright Wiley-VCH Verlag GmbH & Co. KGaA. Reproduced with permission.

Concurrent with the increased response electric field intensity within the active layer, the absorption of the P3HT:PC₆₀BM active layer increased in the vicinity of the LSPR wavelength, as shown in Figure 59.

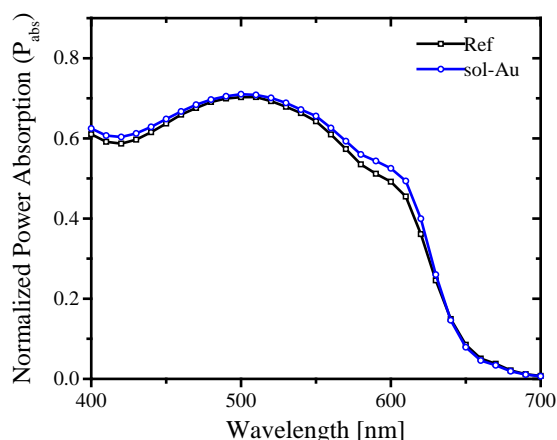


Figure 59. The normalized power absorption, P_{abs} , profile of a P3HT:PC₆₀BM BHJ active layer with a sol-Au interlayer at the ITO/PEDOT:PSS interface. H. Kurt & C.W. Ow-Yang, Impedance Spectroscopy Analysis of the photophysical dynamics due to the nanostructuring of anode interlayers in organic photovoltaics. *Physica Status Solidi A*. Copyright Wiley-VCH Verlag GmbH & Co. KGaA. Reproduced with permission.

The difference between the absorption in reference and sol-Au incorporated devices (Figure 60) confirmed the increased absorption of P3HT:PC₆₀BM BHJ active layer.

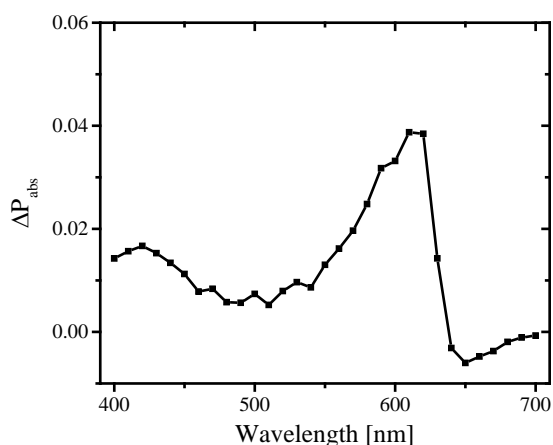


Figure 60. The difference between the normalized power absorption, ΔP_{abs} , profile of a P3HT:PC₆₀BM BHJ active layer with a sol-Au interlayer at the ITO/PEDOT:PSS interface and the reference P3HT:PC₆₀BM BHJ active layer. H. Kurt & C.W. Ow-Yang, Impedance Spectroscopy Analysis of the photophysical dynamics due to the nanostructuring of anode interlayers in organic photovoltaics. *Physica Status Solidi A*. Copyright Wiley-VCH Verlag GmbH & Co. KGaA. Reproduced with permission.

In PCDTBT:PC₇₀BM BHJ OPV device structure, the LSPR wavelength of the sol-Au interlayer had red-shifted to 633 nm, due to the thinner PEDOT:PSS layer (30 nm) and relatively higher refractive index of the PCDTBT:PC₇₀BM blend compared to the P3HT:PC₆₀BM blend, as shown in Figure 61. The response electric field intensity within the device was plotted versus wavelength of the incoming plane wave excitation in Figure 62. The active layer, P3HT:PC₆₀BM BHJ, was positioned between $z = 25$ nm and $z = 95$ nm. The response electric field intensity within the active layer exceeded that of the incident field for wavelength range 500-800 nm. Even though the PCDTBT:PC₇₀BM active layer was 30 nm thinner than the P3HT:PC₆₀BM layer, the spectral match of absorption in PCDTBT:PC₇₀BM and the LSPR wavelength profile of sol-Au interlayers showed stronger correlation in absorption of active layer as in Figure 63. The difference between absorption between reference and sol-Au incorporated devices, Figure 64, confirmed the increased absorption of light in the PCDTBT:PC₇₀BM BHJ active layer.

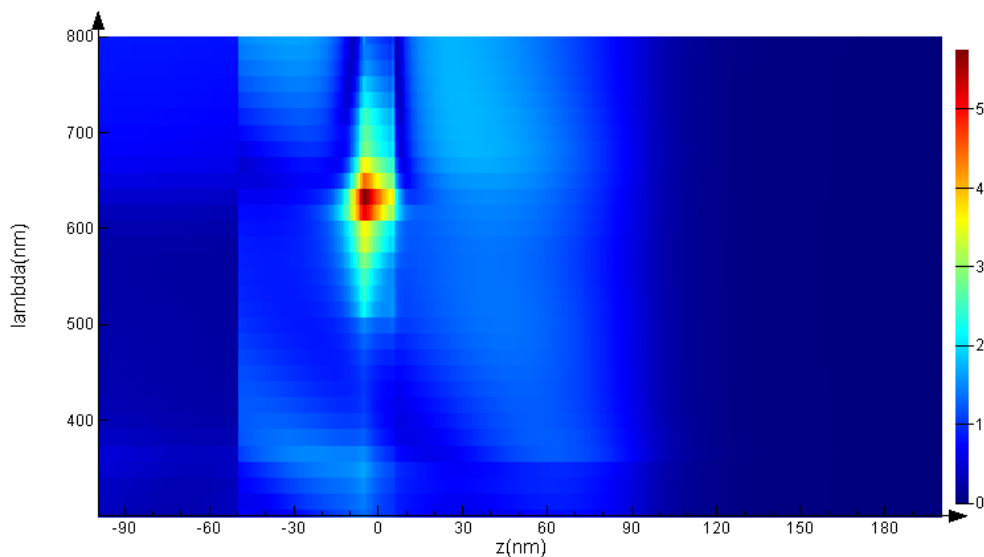


Figure 61. The induced response electric field intensity, $|E|$, profile as propagating light in a PCDTBT:PC₇₀BM(1:4) OPV device with sol-Au interlayer, through the thickness from $z = -100$ nm to $z = 200$ nm and over the wavelength range between 300 nm and 800 nm. The active layer is positioned between $z = 25$ nm and $z = 95$ nm. H. Kurt & C.W. Ow-Yang, Impedance Spectroscopy Analysis of the photophysical dynamics due to the nanostructuring of anode interlayers in organic photovoltaics. *Physica Status Solidi A*. Copyright Wiley-VCH Verlag GmbH & Co. KGaA. Reproduced with permission.

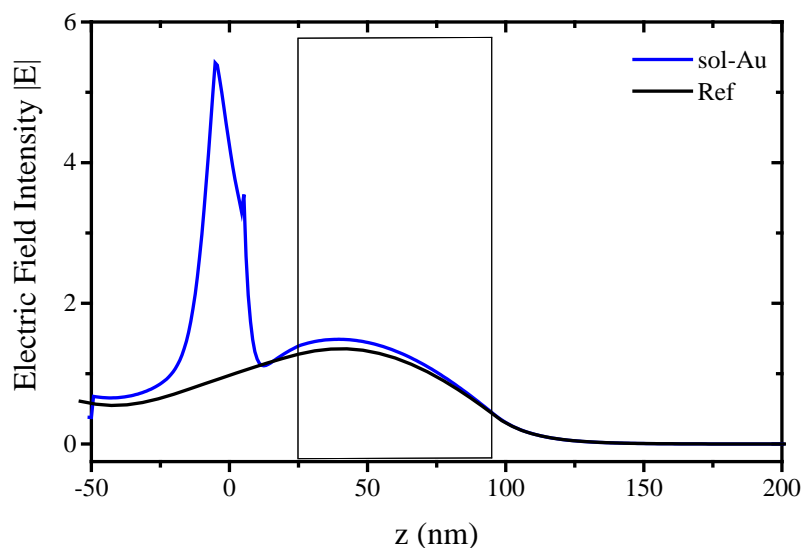


Figure 62. The response electric field intensity, $|E|$, profile as propagating light in a PCDTBT:PC₇₀BM OPV device with sol-Au interlayer, through the thickness from $z = -100$ nm to $z = 200$ nm at the wavelength of 633 nm. The active layer is positioned between $z = 25$ nm and $z = 95$ nm and represented as shaded. H. Kurt & C.W. Ow-Yang, Impedance Spectroscopy Analysis of the photophysical dynamics due to the nanostructuring of anode interlayers in organic photovoltaics. *Physica Status Solidi A*. Copyright Wiley-VCH Verlag GmbH & Co. KGaA. Reproduced with permission.

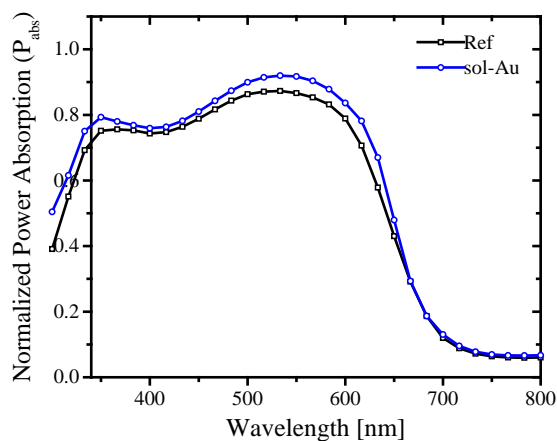


Figure 63. The normalized power absorption, P_{abs} , profile of a PCDTBT:PC₇₀BM BHJ active layer with a sol-Au interlayer at the ITO/PEDOT:PSS interface, compared with the profile of a control device without the sol-Au layer. H. Kurt & C.W. Ow-Yang, Impedance Spectroscopy Analysis of the photophysical dynamics due to the nanostructuring of anode interlayers in organic photovoltaics. *Physica Status Solidi A*. Copyright Wiley-VCH Verlag GmbH & Co. KGaA. Reproduced with permission.

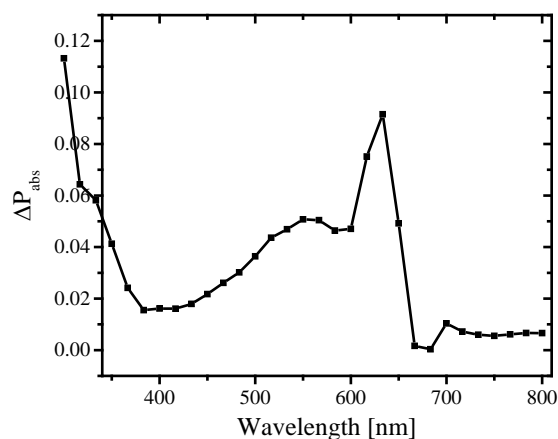


Figure 64. The difference between the normalized power absorption, ΔP_{abs} , profile of a PCDTBT:PC₇₀BM BHJ active layer with a sol-Au interlayer at the ITO/PEDOT:PSS interface and the reference PCDTBT:PC₇₀BM BHJ active layer. H. Kurt & C.W. Ow-Yang, Impedance Spectroscopy Analysis of the photophysical dynamics due to the nanostructuring of anode interlayers in organic photovoltaics. *Physica Status Solidi A*. Copyright Wiley-VCH Verlag GmbH & Co. KGaA. Reproduced with permission.

3.3.2. P3HT:PC₆₀BM and PCDTBT:PC₇₀BM BHJ OPV devices with and without sol-LiF interlayers

We incorporated the sol-LiF nanostructured ITO surfaces into conventional P3HT:PCBM BHJ photovoltaic devices. The control devices consisted of the standard PEDOT:PSS layer deposited on top of ITO without sol-LiF, and the PCE measured was $1.51 \pm 0.11\%$, based on 12 devices. When the ITO was modified by 5.3% sol-LiF coverage, the best power conversion efficiency (PCE) had improved to 2.7%, corresponding to a 74.3% improvement over the control device. For the OPV containing an ITO anode modified by 7.6% sol-LiF coverage, the PCE was 23.7% higher than the best control device.

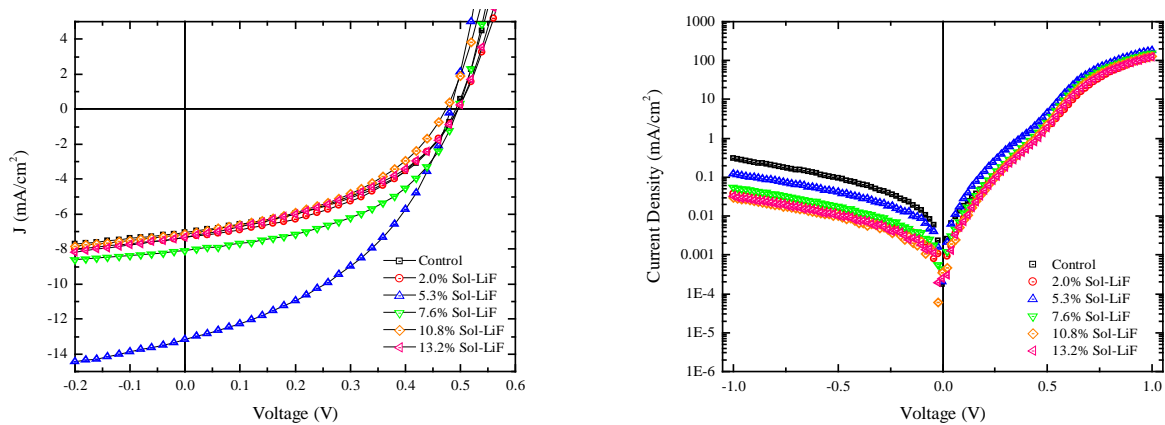


Figure 65. Current density–voltage characteristic curves of P3HT:PC₆₀BM solar cells with ITO anodes modified by different sol-LiF surface coverages, a) under AM1.5G illumination; b) in the dark. Reprinted from *J. Mater. Sci. Mater. Electron.* Tuning hole charge collection efficiency in polymer photovoltaics by optimizing the work function of indium tin oxide electrodes with solution-processed LiF nanoparticles 2015, 9205–9212, Kurt, H., Jia, J., Shigesato, Y. & Ow-Yang, C. W. with permission of Springer.

Table 4. The device parameters of P3HT:PC₆₀BM BHJ OPVs with different levels of LiF nanostructured ITO anodes under AM1.5G illumination. Average PCE was obtained from measurements of the best six performing devices. Reproduced from *J. Mater. Sci. Mater. Electron.* Tuning hole charge collection efficiency in polymer photovoltaics by optimizing the work function of indium tin oxide electrodes with solution-processed LiF nanoparticles 2015, 9205–9212, Kurt, H., Jia, J., Shigesato, Y. & Ow-Yang, C. W. with permission of Springer.

LiF NP Surface Coverage (%)	Work Function of Nanostructured ITO Surface	V_{oc} [mV]	J_{sc} [mA/cm^2]	FF [%]	Best PCE [%]	Dark Ideality Factor	J_{sat} [mA/cm^2]	R_s [Ω/cm^2]	R_{sh} [Ω/cm^2]	Average PCE [%]
0	4.88	492	7.04	45.0	1.56	1.89	7.8E-8	2.23	543.6	1.51±0.11
2.0	4.96	495	7.34	44.1	1.60	2.07	12.5E-8	2.07	716.8	1.57±0.02
5.3	5.07	482	13.17	42.8	2.72	1.73	5.2E-8	1.77	282.3	2.59±0.15
7.6	5.12	496	8.06	48.2	1.93	1.84	7.0E-8	1.90	739.8	1.84±0.07
10.8	5.27	473	7.12	43.2	1.46	1.90	8.5E-8	2.20	590.9	1.45±0.01
13.2	5.30	496	7.31	41.7	1.51	1.94	9.3E-8	2.27	730.4	1.47±0.03

The device with ITO modified by 5.3% sol-LiF coverage showed a short circuit current density (J_{sc}) of 13.2 mA/cm^2 , which is a substantial 87% improvement. In devices with other sol-LiF coverages, J_{sc} fell within a narrow range of 1-4% improvement. The key

parameters of OPVs with ITO anodes modified by different coverages of sol-LiF were tabulated in Table 4. The open circuit voltages (V_{oc}) were similar for the control and sol-LiF-containing OPVs—the variation in values fell within the limits of measurement error. While the fill factor (FF) for control devices was extracted to be 45%, OPVs with sol-LiF-modified ITO anodes dropped to the 42-44% regime, with the exception of the device containing ITO covered 7.6% by sol-LiF, for which the FF improved to 48.2%.

The shunt resistance, generally associated with leakage currents in the device,^[43] and parasitic series resistance (R_s) were extracted using the diode model under constant 1 sun illumination. The dark current ideality factor (n) and reverse saturation current density (J_{sat}) were extracted from dark J-V characteristics according to the two-diode model developed by Suckow and co-workers.^[44] Although R_s had increased only in the device with 13.2% sol-LiF coverage, it was reduced in the other devices, with the best improvement being 21% and 15% of R_s in the control devices, for those with 5.3% and 7.6% sol-LiF coverage, respectively. The shunt resistance (R_{sh}) of the control devices was $589 \pm 54 \text{ } \Omega\text{-cm}^{-2}$. The device containing the 5.3% sol-LiF-modified ITO anode showed an R_{sh} 48% lower than the control devices, whereas the devices with other sol-LiF coverages all had R_{sh} values 22-26% higher (*i.e.*, better). While the control devices demonstrated an n of 1.89, ITO electrodes with 5.3% and 7.6% sol-LiF coverage demonstrated improved n values of 1.73 and 1.84 respectively. In parallel with ideality factors, J_{sat} were slightly improved from $7.8 \times 10^{-8} \text{ mA cm}^{-2}$ to $5.2 \times 10^{-8} \text{ mA cm}^{-2}$ and to $7.0 \times 10^{-8} \text{ mA cm}^{-2}$, respectively for 5.3% and 7.6% sol-LiF covered ITO anodes.

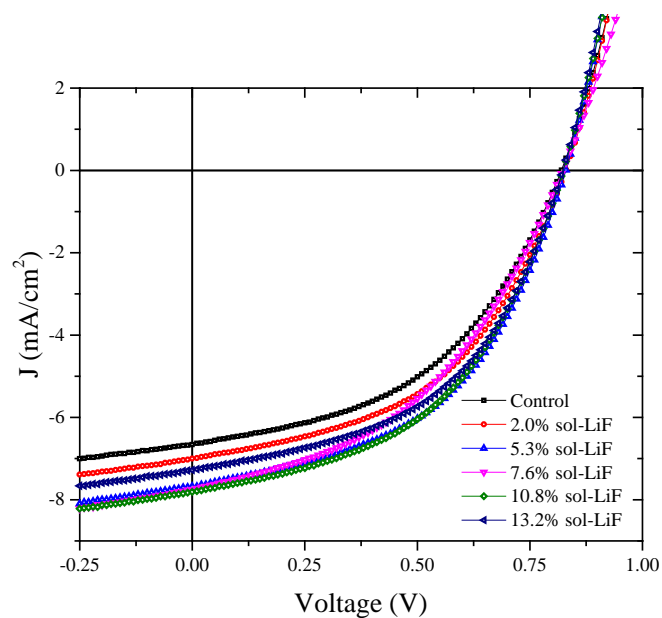


Figure 66. Current density–voltage characteristic curves of PCDTBT:PC₇₀BM solar cells with ITO anodes modified by different sol-LiF surface coverages under AM1.5G illumination.

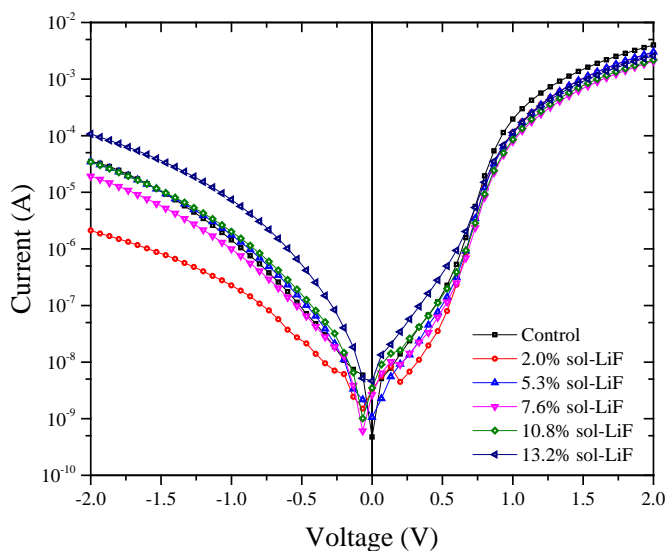


Figure 67. Current–voltage characteristic curves of PCDTBT:PC₇₀BM solar cells with ITO anodes modified by different sol-LiF surface coverages under dark conditions.

Table 5. The device parameters of PCDTBT:PC₇₀BM BHJ OPVs with different levels of LiF nanostructured ITO anodes under AM1.5G illumination.

<i>LiF NP Surface Coverage [%]</i>	<i>Work Function of Nanostructured ITO Surface [eV]</i>	<i>V_{oc} [mV]</i>	<i>J_{sc} [mA/cm²]</i>	<i>FF [%]</i>	<i>PCE [%]</i>
0	4.88	820	6.66	46.5	2.54
2.0	4.96	830	6.99	47.1	2.77
5.3	5.07	825	7.67	47.8	3.02
7.6	5.12	820	7.74	47.2	2.77
10.8	5.27	824	7.81	47.8	3.07
13.2	5.30	820	7.27	41.7	2.94

As we incorporated the sol-LiF nanostructured ITO anodes into PCDTBT:PC₇₀BM BHJ OPV devices, we observed a behavior similar to P3HT:PCBM devices. A surface coverage of 5.3% sol-LiF substantially increased the short circuit current density to 7.67 mA/cm² with respect to reference device with J_{sc} of 6.66 mA/cm². Furthermore, open circuit voltage and fill factor values were higher (*i.e.*, improved) and contributed to a power conversion efficiency (PCE) of 3.02% with respect to reference devices with a PCE of 2.54%. J_{sc} of PCDTBT:PC₇₀BM BHJ OPV devices increased as the surface coverage of sol-LiF nanostructures increased up to surface coverage of 7.81 mA/cm². Further increase in surface coverage led to sudden drop of J_{sc} to 7.27 mA/cm² and fill factor to 41.7%. The highest optimized power conversion efficiency recorded as 3.07% for surface coverage of 10.8% with an improved fill factor reaching to 47.8%. Unlike P3HT:PC60BM BHJ OPV devices, a surface coverage of 10.8% sol-LiF nanostructures was the optimized deposition level for PCDTBT:PC₇₀BM BHJ OPV devices.

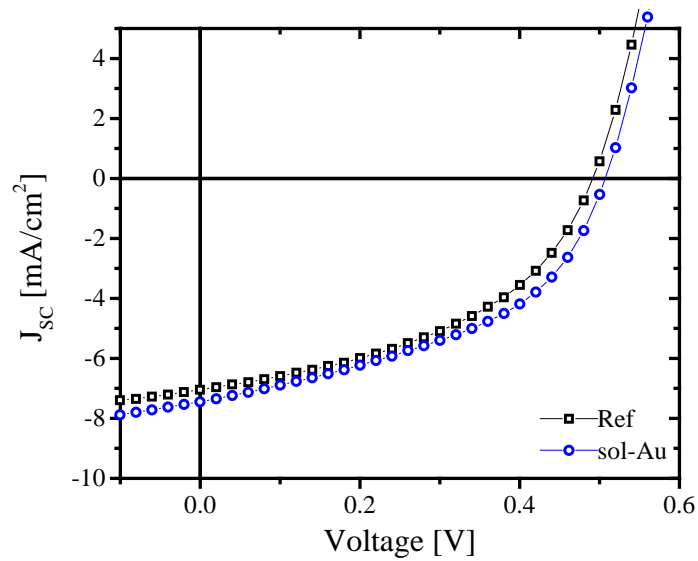


Figure 68. Current density–voltage characteristic curves of P3HT:PC₆₀BM solar cells with and without sol-Au modified ITO anodes under AM1.5G illumination. H. Kurt & C.W. Ow-Yang, Impedance Spectroscopy Analysis of the photophysical dynamics due to the nanostructuring of anode interlayers in organic photovoltaics. *Physica Status Solidi A*. Copyright Wiley-VCH Verlag GmbH & Co. KGaA. Reproduced with permission.

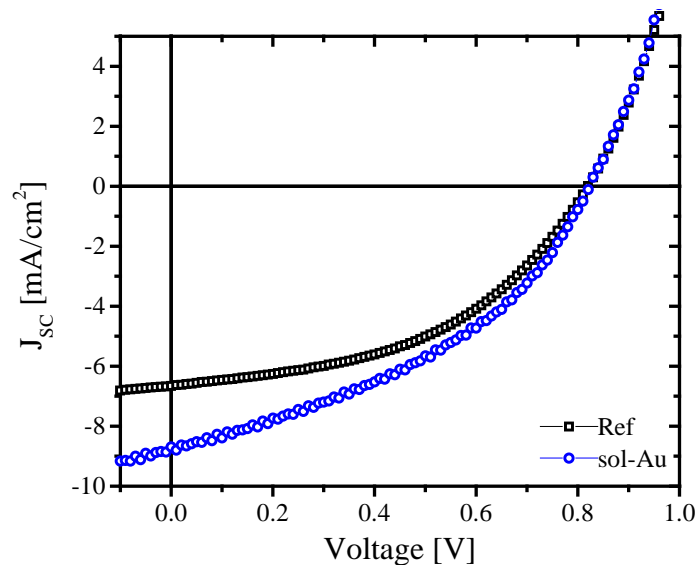


Figure 69. Current density–voltage characteristic curves of PCDTBT:PC₇₀BM solar cells with and without sol-Au modified ITO anodes under AM1.5G illumination. H. Kurt & C.W. Ow-Yang, Impedance Spectroscopy Analysis of the photophysical dynamics due to the nanostructuring of anode interlayers in organic photovoltaics. *Physica Status Solidi A*. Copyright Wiley-VCH Verlag GmbH & Co. KGaA. Reproduced with permission.

Table 6. The device characteristics of sol-Au modified and reference P3HT:PC₆₀BM and PCDTBT:PC₇₀BM OPVs under AM1.5G illumination. H. Kurt & C.W. Ow-Yang, Impedance Spectroscopy Analysis of the photophysical dynamics due to the nanostructuring of anode interlayers in organic photovoltaics. *Physica Status Solidi A*. Copyright Wiley-VCH Verlag GmbH & Co. KGaA. Reproduced with permission.

BHJ Type	Interlayer	J_{sc} [mA·cm ⁻²]	V_{oc} [mV]	FF [%]	η [%]
P3HT:PC ₆₀ BM	-	-7.04	492	45.0	1.56
	sol-Au	-7.44	508	45.5	1.72
PCDTBT:PC ₇₀ BM	-	-6.66	820	46.5	2.54
	sol-Au	-8.69	823	40.6	2.90

The incorporation of sol-Au interlayers into both types of BHJ OPV devices improved the power conversion efficiency. In P3HT:PC₆₀BM BHJ OPV devices, sol-Au interlayers increased the J_{sc} by 5% while increasing the V_{oc} from 492 mV to 508 mV and slightly perturbing the fill factor. The overall PCE had improved by 10.2%. On the other hand, the fill factors had dropped from 46.5% to 40.6% in PCDTBT:PC₇₀BM BHJ OPV devices with sol-Au interlayers. However, the PCE was significantly improved by 14.2%, owing to an increase in J_{sc} by 30.5%. The loss of the fill factor was strongly compensated by the gain in J_{sc} .

In order to evaluate the spectral relation of PCE improvement, we analyzed the external quantum efficiency of both types of devices using an incident photon-to-electron conversion efficiency setup (IPCE). In Figure 70 and Figure 71, both types of BHJ OPV devices with sol-LiF interlayers showed an increase in external quantum efficiency (EQE) independent of the wavelength of the incident light. However, both types of BHJ OPVs with sol-Au interlayers exhibited a wavelength dependent improvement in EQE as predicted in FDTD simulations of sol-Au interlayers incorporated into OPV devices.

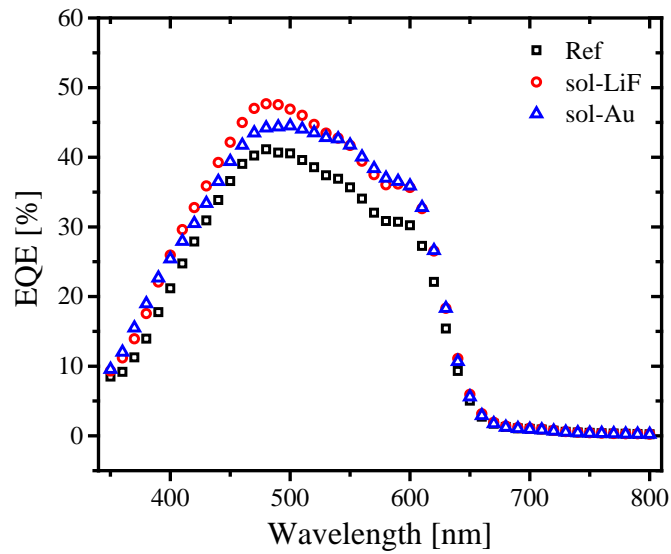


Figure 70. EQE of P3HT:PC₆₀BM control device, compared to ones with either a sol-LiF interlayer with surface coverage of 7.6% (red circles) or a sol-Au interlayer (blue triangles). H. Kurt & C.W. Ow-Yang, Impedance Spectroscopy Analysis of the photophysical dynamics due to the nanostructuring of anode interlayers in organic photovoltaics. *Physica Status Solidi A*. Copyright Wiley-VCH Verlag GmbH & Co. KGaA. Reproduced with permission.

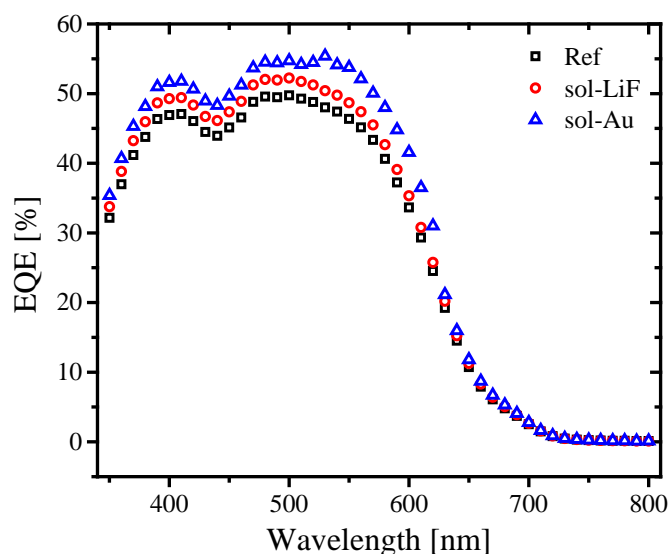


Figure 71. EQE of PCDTBT:PC₇₀BM control device, compared to ones with either a sol-LiF interlayer with a surface coverage of 10.8% (red circles) or a sol-Au interlayer (blue triangles). H. Kurt & C.W. Ow-Yang, Impedance Spectroscopy Analysis of the photophysical dynamics due to the nanostructuring of anode interlayers in organic photovoltaics. *Physica Status Solidi A*. Copyright Wiley-VCH Verlag GmbH & Co. KGaA. Reproduced with permission.

3.4. Discussion

To understand why the conventional P3HT:PCBM (1:0.6) devices, which were fabricated in ambient air and clean room conditions, showed a substantial 74.5% improvement in PCE when the ITO anode was modified by 5.3% sol-LiF coverage, it would be worthwhile to revisit Figure 44 and note that these modified anodes had a surface Φ of 5.07 eV. The modified anode with such a Φ value would align well with the energy level of PEDOT:PSS, reported to be at 5.10 eV.^[45,46] It appears that the Φ of the modified ITO facilitates the collection of hole charges through reducing the Schottky barrier between ITO and PEDOT:PSS to an ohmic contact. The better energy level alignment thus contributes to the 87% improvement in J_{sc} . As J_{sc} indicates the number of photogenerated charge carriers extracted to the external circuit, these results are consistent with an improvement in hole collection efficiency.

Since faster and improved charge collection efficiency would be due to an increase in the effective charge carrier lifetime within the bulk heterojunction, these results revealed a general improvement in the effective charge carrier lifetime up to 6-fold, correlated with a 78% decrease in contact resistance in the best-performing device. Since hole mobility and thickness in the PEDOT:PSS hole transport layer were not changed, the faster hole transport— see Chapter 4 —can be attributed to the increased electronic surface states at the modified ITO,^[29,31] resulting in an increase electrical potential gradient imposed on the mobile holes and sweeping them to the anode more quickly. However, the hole collection efficiency and short circuit current improvement were still significantly below what this improvement leads us to expect. One possible explanation would be that the increase in induced polarization at the ITO contact surface would offset these gains, leading to a charge accumulation at the sol-LiF interface. The tradeoff between the competing effects^[47] gave rise to the optimal device PCE of 2.59%, when 5.3% of the ITO surface was modified by sol-LiF nanostructuring.

Furthermore, contributions to R_s can come from 3 sources: (i) contact resistance between the electrode and the active layer, (ii) the bulk resistance of the polymer film, or (iii) the bulk resistance of the contacts.^[48] In this study, the polymer film and the contacts were the same for all of the devices tested, so the variation in R_s stems from differences at the contact between the electrode and the active layer, *i.e.* with sol-LiF coverage.^[43] When sol-LiF NPs increase the modified ITO surface Φ , the charge transfer away from the ITO is increased into the dielectric layer in direct contact.^[29] Thus with little variation in electrical potential at the contact and an increase in the charge collection current for the modified electrode with the 5.07 eV work function, it follows that the contact resistance for the device with this interlayer would be the lowest. For ideal solar cell behavior, R_s should be 0 and R_{sh} infinite.^[48]

Reduction in J_{sat} and n parameters could be the indicator of greater selectivity in harvesting charge carriers.^[21] This enhancement can be attributed to lowering the energy barrier for hole charge carrier^[49] and reduced surface recombination for bound-polaron pairs^[50,51] at the PEDOT:PSS/ITO interface.

Compared to the control device, the low R_{sh} for the device with Φ of 5.07 eV suggests a difference in wetting by the PEDOT:PSS layer. From Figure 43, the modified ITO surface roughness scaled directly proportional to sol-LiF surface coverage. An increase in surface roughness could lead to the formation of hot spots in the electrode layer. However, sol-LiF modified ITO anodes either improved or did not affect R_{sh} with the exception of 5.3% sol-LiF coverage. Moreover, increasing surface roughness increased R_s with respect to control devices with the exception of 13.2% sol-LiF coverage.

In addition to roughness, discontinuity in the sol-LiF layer may have also induced changes in wetting of PEDOT:PSS on the modified electrode. However, SEM images of all layers reveal sol-LiF layers that are discontinuous for all surface coverages investigated,^[37] and the discontinuous nature of the sol-LiF layer would not be the root cause for the unusually low R_{shunt} relative to the other devices with unmodified and modified ITO electrodes.

Despite the dramatic improvement in J_{sc} and R_s for the modified electrode with a Φ of 5.07 eV, the FF did not improve significantly, due to the substantially poorer R_{sh} . Instead, the superior FF of the modified electrode with a Φ of 5.12 eV resulted from a moderate improvement in balanced contributions from J_{sc} , R_s , and R_{sh} .

Unlike the P3HT:PC₆₀BM BHJ OPV devices with sol-Au interlayers (5.3% areal density), we observed an overall improvement in device characteristics at a higher surface coverage (10.8%) in PCDTBT:PC₇₀BM BHJ OPV devices. The work function of sol-LiF interlayers with 10.8% was determined to be 5.27 eV. Due to the relatively high surface roughness of substrates with 10.8% sol-LiF coverage and relatively thinner PEDOT:PSS HTL layer (30 nm) used in PCDTBT:PC₇₀BM BHJ OPVs, a higher amount of sol-LiF nanostructures were in contact with not only with HTL layer but also with the BHJ active layer. The relatively deeper HOMO level of the PCDTBT donor polymer (5.5 eV) than P3HT (5.2 eV) could be the underlying reason for this change in the optimized surface coverage. It leads to the similar conclusion of better energy alignment led to efficient extraction of holes from the BHJ active layer as well as the HTL layer.

The incorporation of sol-Au interlayers in both types of BHJ OPVs improved the PCE of the devices. However, devices characteristics did not correlate with the underlying mechanism, due to an abrupt change in fill factor. The EQE analysis revealed that, unlike in

the case of sol-LiF interlayers, enhancement of PCE depended on the illumination wavelength, suggesting that enhancement of the response electric field in the active layer may better explain the phenomenon. Since the absorption profile of PCDTBT:PC₇₀BM (see Figure 71) has a better spectral overlap with the LSPR emission profile of the sol-Au interlayer (see Figure 42) than that of the P3HT:PC₆₀BM blend (see Figure 70), the PCE improvement was more substantial in PCDTBT:PC₇₀BM despite its thinner active layer.

3.5. Conclusion

In summary we have evaluated the performance of a PEDOT:PSS/ITO interface in a polymer-based solar cell, by nanostructuring the ITO surface with sol-LiF nanoparticles covering increasing areal density and sol-Au nanoparticles. We have determined the Φ of the modified ITO by PESA and observed an increase in Φ with increasing coverage of sol-LiF. FDTD simulations of stimulated LSPR response fields revealed that sol-Au interlayers improve the absorption of active layer in the BHJ OPV devices we investigated. We have incorporated the sol-LiF- and sol-Au-modified ITO anodes into P3HT:PC₆₀BM and PCDTBT:PC₇₀BM BHJ OPVs, and compared their performance with non-modified ITO-based control devices. Although the effect of nanostructuring did not significantly perturb wetting of the PEDOT:PSS on the modified ITO surface, the presence of the sol-LiF enabled tuning of the ITO surface Φ , via optimizing coverage of the ITO surface, and the presence of the sol-Au improved the EQE and PCE of both BHJ OPV devices in the vicinity of LSPR wavelength region.

In order to confirm that sol-LiF modified ITO anodes enable tuning of the device performance, we have incorporated the nanostructured interlayers into BHJ OPV devices based on two different types of BHJ polymer blends with significantly dissimilar highest occupied molecular orbital (HOMO) levels, and analyzed the *J-V* and EQE device characteristics. The optimized performances substantiated our first part of our hypothesis and revealed different levels of sol-LiF deposition led to optimized device performances for two different BHJ polymer blends. To rule out optical effects of sol-LiF and confirm the sol-Au interlayer induced field enhancement, the external quantum efficiency (EQE) profiles were evaluated. Revealing sol-LiF interlayer induced device performance increase

had no spectral dependence unlike sol-Au interlayer induced improvements. Furthermore, sol-Au interlayer induced field enhancement investigated using finite difference time domain (FDTD) simulations. FDTD results, in order to compare the induced field enhancement with correlated the findings in the EQE profiles for both types of BHJ polymer blends.

We conclude that the significantly improved PCE in both types of devices, was consistent with an improved electronic hole collection efficiency resulting from optimized energy level alignment between PEDOT:PSS and the modified sol-LiF anode. Our results confirm that sol-LiF can be used to tune the surface Φ of ITO for improved energy level matching with other contact layers and enhance the hole extraction efficiency and sol-Au can be utilized to control the level of light intensity within the active layer to improve the effective absorption of the active layer. As we hypothesized, dielectric sol-LiF interlayers improved the OPV device performance through improving the energy level alignment. Evidently, different levels of sol-LiF surface coverage show optimized device performance, due to the different HOMO levels of the donor polymers in spite of the using identical hole transport layer (PEDOT:PSS). In parallel, sol-Au interlayers significantly improved the device performance through increased short circuit density in the expense of loss in the fill factor implying increased charge generation rate. However, a more detailed characterization was in need for decisively identify the underlying improvement mechanisms.

CHAPTER 4: IMPEDANCE SPECTROSCOPY OF OPVS WITH NANOSTRUCTURED INTERLAYERS

4.1. Introduction

The hypothesis that we had addressed in the focused study in this chapter was that the mechanisms contributing to improved performance in devices with nanostructured interlayers at the ITO anodes can be elucidated by *in-operando* impedance spectroscopy (IS) analysis. To validate, we analyze the IS data measured from the devices presented in Chapter 3, by fitting the parameters to an equivalent circuit and evaluating the photophysical dynamics—*e.g.*, hole transport, charge separation, and mobile charge carrier generation rates.

Impedance spectroscopy (IS) is a non-destructive small perturbation technique for monitoring the dynamics in an electrochemical system. Recently, this technique has been applied toward probing photoelectrochemical response in organic photovoltaics.^[47] In IS, low amplitude alternating current (AC) signal is applied to probe charge carrier dynamics, recombination kinetics, diffusion mechanisms and the density of states in both in-situ and dark conditions. The Cole-Cole plots of OPVs typically consist of a dominant semi-circle arc at low frequencies, associated with the recombination of photogenerated charge carriers within active layers. At higher frequencies, transport and series resistances determine the impedance behavior, in addition to the dielectric response.

The measured capacitance in OPVs consists of multiple contributions: 1) the geometrical capacitance, which arises from the depletion layer between the opposing electrodes, and 2) the chemical capacitance, which can also be thought of as the electrochemical potential originating from photogenerated charge carriers at BHJ interfaces.^[47] In order to analyze the individual OPV operating mechanisms, several different forms of equivalent circuit models have been proposed.^[52] IS enables the evaluation of BHJs, interlayers and interfaces in terms of their individual roles and impacts in OPV operation, such as charge extraction efficiency, charge transport efficiency, global charge mobility, recombination and trap assisted losses.

Herein we present how IS can be applied for analyzing to investigate nanostructured anode interlayers. In this study, we used IS to validate the possibility for engineering not only energy level alignment, but also i) hole selectivity improvement with dielectric nanostructured interlayers; ii) charge carrier generation rate improved with plasmonic metal nanostructures; and iii) recombination/transport kinetics. We have analyzed two different interlayers, each with distinct dominant physical interactions with bulk heterojunction polymer blends: i) nanostructured LiF interlayers for surface work function tuning of the ITO anode to improve charge carrier extraction^[29] and ii) nanostructured Au interlayers^[53,54] for plasmonic field enhancement within the BHJ to improve charge generation. Diblock copolymer micelle nano-reactors^[29,55] were utilized for the synthesis of nanostructured layers to provide monodisperse size control and enable quasi-ordered array formation for uniform deposition (Figure 72 and Figure 73). Two different traditional BHJ polymer blends were used as the model systems: P3HT:PC₆₀BM (1:0.6) and PCDTBT:PC₇₀BM (1:4). The difference in the highest occupied molecular orbital (HOMO) levels of P3HT (-5.2 eV)^[56] and PCDTBT (-5.5 eV)^[57] donor polymers enables us to probe the effects of work function tuning by sol-LiF interlayers at optimized surface coverage. Different spectral absorption profiles of two BHJ blends enabled us to compare the extent of plasmonic field enhancement of sol-Au interlayers. By applying IS analysis, we were able to distinguish the effects of each nanostructured interlayer on charge generation/recombination kinetics and charge transport/collection kinetics in BHJ OPVs. We have not only observed an improvement in the performance of each type of device, but also identified the actual mechanisms resulting in the improved performance by using IS. Our results justify continuing research on organic photovoltaics, given the advantages and drawbacks hampering efficiency.

This chapter of the thesis is mainly based on our recently accepted publication. H. Kurt & C.W. Ow-Yang, Impedance Spectroscopy Analysis of the photophysical dynamics due to the nanostructuring of anode interlayers in organic photovoltaics. *Physica Status Solidi A*. Copyright Wiley-VCH Verlag GmbH & Co. KGaA. Reproduced with permission.

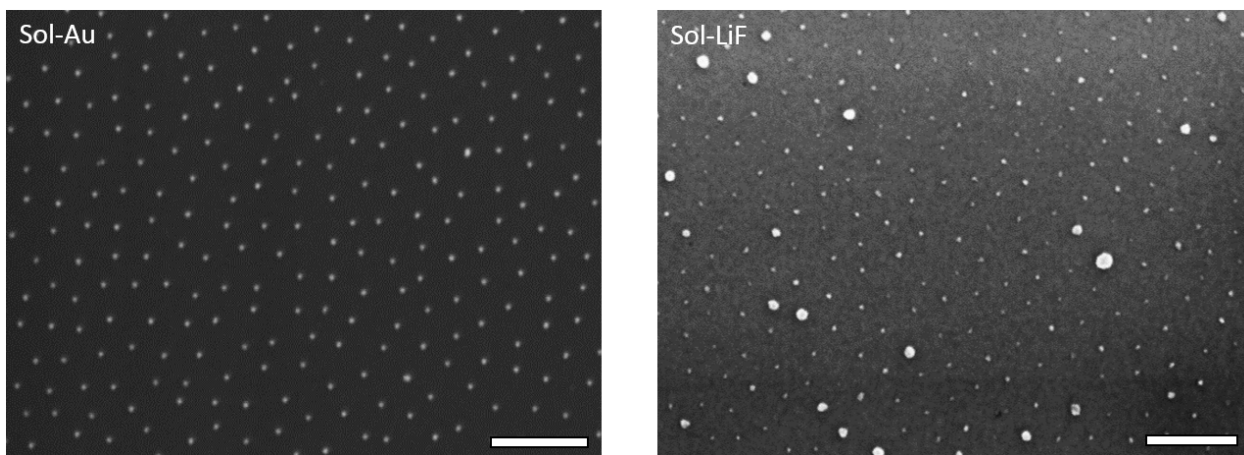


Figure 72. SEM micrographs of sol-Au nanoparticles (left) and sol-LiF nanoparticles (right) after a single deposition on a silicon wafer. The scale bar represents 200 nm. H. Kurt & C.W. Ow-Yang, Impedance Spectroscopy Analysis of the photophysical dynamics due to the nanostructuring of anode interlayers in organic photovoltaics. *Physica Status Solidi A*. Copyright Wiley-VCH Verlag GmbH & Co. KGaA. Reproduced with permission.

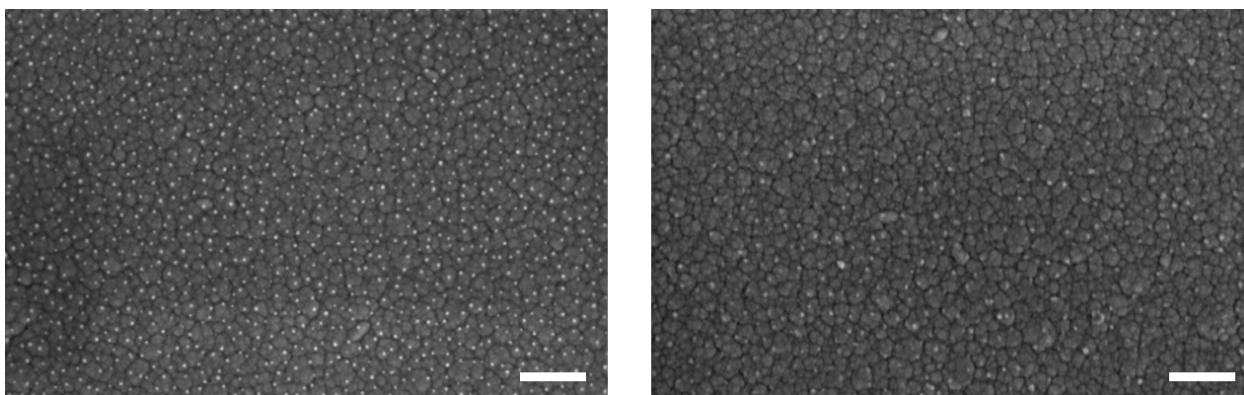


Figure 73. SEM micrographs of sol-Au nanoparticles (left) and sol-LiF nanoparticles (right) after a single deposition on ITO coated glass. The scale bar represents 200 nm. H. Kurt & C.W. Ow-Yang, Impedance Spectroscopy Analysis of the photophysical dynamics due to the nanostructuring of anode interlayers in organic photovoltaics. *Physica Status Solidi A*. Copyright Wiley-VCH Verlag GmbH & Co. KGaA. Reproduced with permission.

Impedance spectroscopy became a well-established technique in dye-sensitized and organic photovoltaic cells in recent years,^[47,58,59] and several informative reviews are available in the literature.^[60] Here we will briefly introduce only the key concepts of IS directly relevant to our analysis and explain the methodology that we have used.

For IS analysis, a DC bias is applied with the superposition of a low amplitude AC signal across a frequency range. The AC signal should be small enough to probe the differential information from the density of states and quasi-Fermi level of the photovoltaic cell. Resistance (Z') represents the measure of difficulty as the current travels through the conductor. Reactance (Z'') represents the opposition of a circuit element – e.g. capacitor – to the change in the current or voltage. The equivalent-circuit method (Figure 74) is used to fit the distributed resistor-capacitor and resistor-constant phase element components collectively within the system.

In order to compare only the contributions of the modified interlayers to the charge dynamics, the series AC resistance (R_s) of the OPVs are first subtracted, thus removing the geometrical capacitance (C_g), which arises from the polarization between the anode and cathode, with the dielectric layer being the polymer blend (having a relative permittivity, $\epsilon_r \approx 3$),^[61]

$$C_g = \frac{\epsilon_0 \epsilon_r A}{d} \quad (1)$$

where ϵ_0 is free space permittivity, A is the area of the device, and d is the active layer thickness.

In the resulting Cole-Cole plots, the characteristic dominant low-frequency arc represents the recombination dynamics in the device, while the smaller higher frequency arc represents the charge transport events, which are faster in nature. To analyze the recombination dynamics represented by the low frequency arc, a parallel circuit is used, consisting of a resistor and a constant phase element. The constant phase element approach is used to represent the BHJ domains as distributed circuit elements with individual time constants.^[62] For the higher frequency arc, transport resistance (R_{tr}) and capacitance (C_{tr}) circuit elements are used.

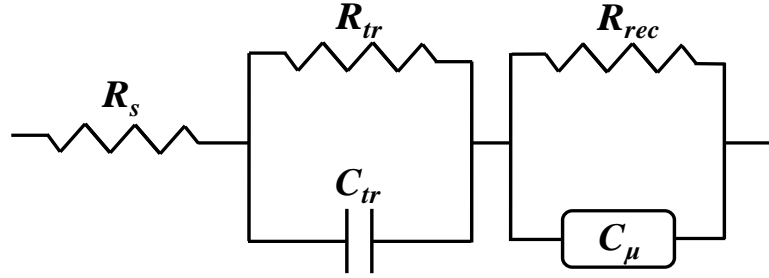


Figure 74. The equivalent circuit model used for our IS analysis. H. Kurt & C.W. Ow-Yang, Impedance Spectroscopy Analysis of the photophysical dynamics due to the nanostructuring of anode interlayers in organic photovoltaics. *Physica Status Solidi A*. Copyright Wiley-VCH Verlag GmbH & Co. KGaA. Reproduced with permission.

The chemical capacitance (C_μ) originates from the polarization of charge carriers generated at the BHJ interfaces. C_μ represents the increase in mobile charge density, n , and can be measured from the changes in n at quasi-Fermi level (E_F), since it directly affects the density of the states as

$$C_\mu = q \frac{dQ}{dE_F} = q^2 d \frac{dn}{dE_F}, \quad (2)$$

where q represents the unit electronic charge, Q the total charge, and d the active layer thickness. By integrating the differential changes in C_μ over the applied bias range, one can determine the number of charge carrier of the system as in Equation (3). However, since the applied bias does not affect the quasi-Fermi level directly, a proportionality constant, α , is used for relating the applied bias to the shift in the quasi-Fermi level. Since electron and hole mobilities are significantly different in P3HT:PC₆₀BM and PCDTBT:PC₇₀BM systems, for example appropriate α constants can be utilized to relate the quasi-Fermi level to the applied bias. The initial number of charge, n_0 , is approximated from the charge carrier flux at short-circuit condition using $J_{sc}R_n C_n / qd$.

$$n = \frac{1}{d} \int C_\mu dE_F + n_0 = \frac{1}{qd} \int C_\mu \alpha dV + n_0 \quad (3)$$

The transport lifetime, τ_{tr} , and recombination lifetime, τ_{rec} , are extracted from fitting an equivalent circuit model to the overall system in the frequency domain by Equation (4) and (5):

$$\tau_{tr} = C_{tr}R_{tr} \quad (4)$$

$$\tau_{rec} = C_{\mu}R_{rec} \quad (5)$$

The recombination lifetime value can then be combined with the number of charge carrier to extract the recombination rate, k_{rec} , and recombination order, δ , as below:

$$k_{rec} = \frac{n-n_0}{\tau_{rec}(n)} \quad (6)$$

$$\delta \equiv \frac{d \log(k_{rec})}{d \log(n)} \quad (7)$$

Meanwhile, the transport lifetime is used to estimate the global charge mobility, μ , in the system as:

$$\mu = \frac{d^2}{V_{oc} \tau_{tr}} \quad (8)$$

4.2. Experimental

Experimental procedure was implemented to ensure the linearity, causality and stability conditions. Linearity of the impedance response was carefully analyzed using different AC perturbation amplitudes. The applied AC amplitudes were confirmed to be small enough to assure linear response. Causality was confirmed by examining the solar cell response before and after impedance measurements. Stability of impedance response of solar cells were validated by three consecutive measurements.

Equivalent circuit modelling was performed using ZView and EIS analyser softwares. The initial value of series resistance (R_s) was extrapolated from impedance response at high frequency region. Initial value of R_{rec} and C_{μ} was obtained using the low frequency arc of the impedance response. The model fitting procedure was continued until reaching highest of 5% error.

4.3. Results & Discussion

Our previous studies have shown that nanostructured interlayers could improve the OPV performance by lowering the probability of recombination for the mobile charge carriers.^[37] In this work, we perform detailed analyses of the recombination and transport kinetics in order to understand more precisely the mechanisms by which the nanostructured interlayers hinder recombination and facilitate charge transport. To this end, we have evaluated OPV devices with anodes modified by sol-LiF and sol-Au interlayers. We performed IS analysis on the devices and applied the equivalent-circuit model shown in Figure 74, in order to decouple the recombination and transport kinetics and extract the contributions to these parameters from the modified interlayers. Finally, from the insights revealed by these transport processes we deduce the different physical mechanisms resulting in improved OPV characteristics.

Nanostructured sol-LiF and sol-Au interlayers were deposited on ITO anodes (Figure 73). The surface coverage of sol-LiF nanoparticles was controlled by sequential spin coating alternating with plasma etch removal of the polymeric material. For P3HT:PC₆₀BM devices, an optimized sol-LiF coverage of 7.6% resulted in a work function of 5.12 eV at the ITO electrode. For PCDTBT:PC₇₀BM devices, an optimized sol-LiF coverage of 10.8% yielded a work function of 5.27 eV. The optimized device performances were attributed to improved energy level alignment of the HOMO level of the PEDOT:PSS hole transport layer (HTL) to the anode. Only a single deposition of sol-Au interlayers was investigated to maintain the level of uniformity and order of the nanoparticles array effectively. A thin (30-40 nm) layer of PEDOT:PSS (-5.1 eV HOMO)^[46] was still used to improve the planarity of the electrode surface. The device characteristics of the P3HT:PC₆₀BM and PCDTBT:PC₇₀BM OPV devices with modified and unmodified interlayers are summarized in Table 7. Sol-LiF interlayers improved the overall device characteristics for both BHJ types, but the improvement is mainly attributed to an increase in short-circuit current density and fill factor. On the other hand, the fill factor change in the sol-Au interlayers were not correlated in both types of BHJ OPVs. For P3HT:PC₆₀BM BHJ devices, a slight increase was observed in the J_{sc} , the open-circuit voltage (V_{oc}) and the fill factor (FF), while in the PCDTBT:PC₇₀BM BHJ devices, the short circuit current density was improved by 30%, countered by a decrease in the fill factor from 46.5% to 40.6%.

The sol-Au interlayer on glass surface exhibited a localized plasmon resonance (LSPR) at a wavelength of 550 nm in the absorption spectra (Figure 75a), while Finite Difference Time Domain (FDTD) simulations of the sol-Au interlayer revealed similar extinction characteristics (Figure 41). The external quantum efficiency (EQE) characteristics of the devices investigated are presented in Figure 75b and Figure 75c. The devices containing sol-LiF interlayers showed a uniform increase in EQE over all wavelengths. However, devices modified by sol-Au interlayers showed significantly improved EQE in the 550-625 nm wavelength range for both BHJ types. The improvements in EQE and in J_{sc} for the PCDTBT:PC₇₀BM devices were more dominant than in the P3HT:PC₆₀BM ones, which was consistent with the absorption tail of the PCDTBT blend stretching out to 700 nm, whereas that of the P3HT blend depleted at 650 nm. Moreover, FDTD simulations of sol-Au interlayers within the actual device geometry further revealed that sol-Au interlayers both enhanced the stimulated response electric field intensity within the active layer and improved the degree of absorption of the incoming electric field.^[63] The spectral dependence of active layer absorption was improved in the 560-630 nm spectral range, as shown in Figure 63 and Figure 64.

Table 7. The device characteristics of interlayer-modified and reference P3HT:PC₆₀BM and PCDTBT:PC₇₀BM OPVs under AM1.5G illumination. H. Kurt & C.W. Ow-Yang, Impedance Spectroscopy Analysis of the photophysical dynamics due to the nanostructuring of anode interlayers in organic photovoltaics. *Physica Status Solidi A*. Copyright Wiley-VCH Verlag GmbH & Co. KGaA. Reproduced with permission.

BHJ Type	Interlayer	J_{sc} [mA cm ⁻²]	V_{oc} [mV]	FF [%]	η [%]
P3HT:PC ₆₀ BM	-	-7.04	492	45.0	1.56
	sol-LiF	-8.06	496	48.3	1.93
	sol-Au	-7.44	508	45.5	1.72
PCDTBT:PC ₇₀ BM	-	-6.66	820	46.5	2.54
	sol-LiF	-7.81	824	47.8	3.08
	sol-Au	-8.69	823	40.6	2.90

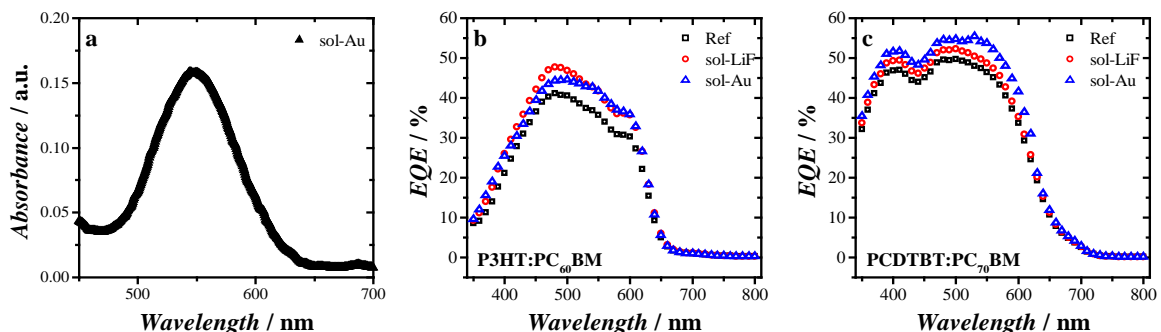


Figure 75. a) Absorption spectra showing the colloidal gold nanoparticle response, compared to the EQE of b) P3HT:PC₆₀BM control device, compared to ones with either a sol-LiF interlayer (red circles) or a sol-Au interlayer (blue triangles) and c) PCDTBT:PC₇₀BM. H. Kurt & C.W. Ow-Yang, Impedance Spectroscopy Analysis of the photophysical dynamics due to the nanostructuring of anode interlayers in organic photovoltaics. *Physica Status Solidi A*. Copyright Wiley-VCH Verlag GmbH & Co. KGaA. Reproduced with permission.

The impedance response of the P3HT:PC₆₀BM devices with and without modified anodes are summarized in Figure 76. Devices with sol-Au and sol-LiF interlayers exhibited significantly lower resistance (Z') and reactance ($-Z''$). The frequency response of the reactance showed a dominant low-frequency and minor high-frequency loss mechanism.^[64] We assigned the dominant low-frequency loss mechanism as recombination losses within the BHJ. As for the minor high-frequency loss, we attributed that mechanism to be transport-related losses within the BHJ and the contacting interlayers.

4.3.1. Recombination Lifetime

The time constants for each of loss mechanism can be converted from the angular frequency response plots. Because recombination generally dominates the impedance response of an OPV device, the recombination-related time constant, τ_{rec} , which corresponds to the average time between recombination events, represents the product of recombination resistance and capacitance. The value of τ_{rec} can be approximated directly from the frequency plot of the impedance response.

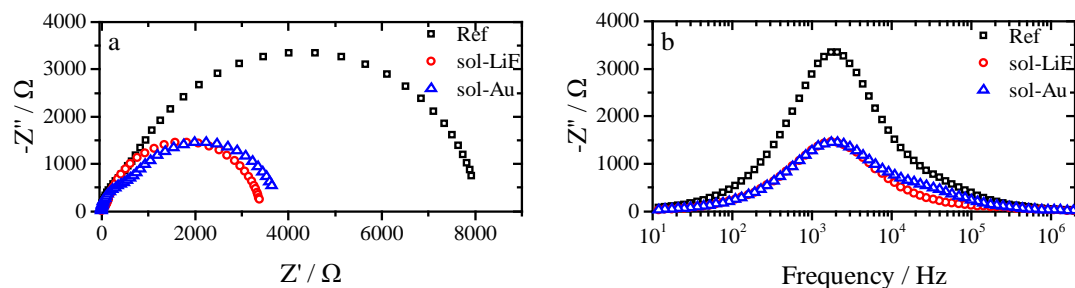


Figure 76. The impedance response of the reference (Ref) device, the sol-LiF device (sol-LiF, red circles), and the plasmonic gold enhanced device (sol-Au, blue triangles) a) Cole-Cole plot of resistance (Z') and reactance (Z'') b) Frequency dependence of reactance (Z''). No DC bias applied. H. Kurt & C.W. Ow-Yang, Impedance Spectroscopy Analysis of the photophysical dynamics due to the nanostructuring of anode interlayers in organic photovoltaics. *Physica Status Solidi A*. Copyright Wiley-VCH Verlag GmbH & Co. KGaA. Reproduced with permission.

Although the recombination resistance (R_{rec}) of photovoltaic cells with modified interlayers was significantly lower in comparison to the reference devices, the substantial improvement in device characteristics suggests that the recombination resistance alone may not be solely responsible for the improved power conversion efficiency (PCE) in devices with modified interlayers. When the charge carrier concentrations increased in an operating device, the probability of mobile charge carriers interacting with each other would have increased as a result, and also lowered the recombination resistance. This behavior was manifested by the improvement in J_{sc} , despite the drop in R_{rec} , and was consistent with the variation in R_{rec} at low bias (Figure 77a and Figure 77b). When the applied voltage approached the V_{oc} , the devices with modified interlayers showed a higher recombination resistance than the reference devices, indicating that the drift current dropped at such a relatively high applied bias. As a consequence, the probability was lowered for mobile charge carriers to reach their respective electrodes. In contrast at low drift currents, it appeared that the modified interlayers improved the recombination resistance and lowered the recombination losses, by either sweeping the mobile charges more quickly away from the BHJ (toward the electrodes) or increasing the mobile charge carrier density.^[65] To differentiate between these two possible mechanisms, it is not sufficient to monitor the recombination resistance alone to determine the effects of the modified interlayers on recombination processes. Instead, the charge carrier density and charge carrier lifetime profiles should also be considered, via analyzing the chemical capacitance.

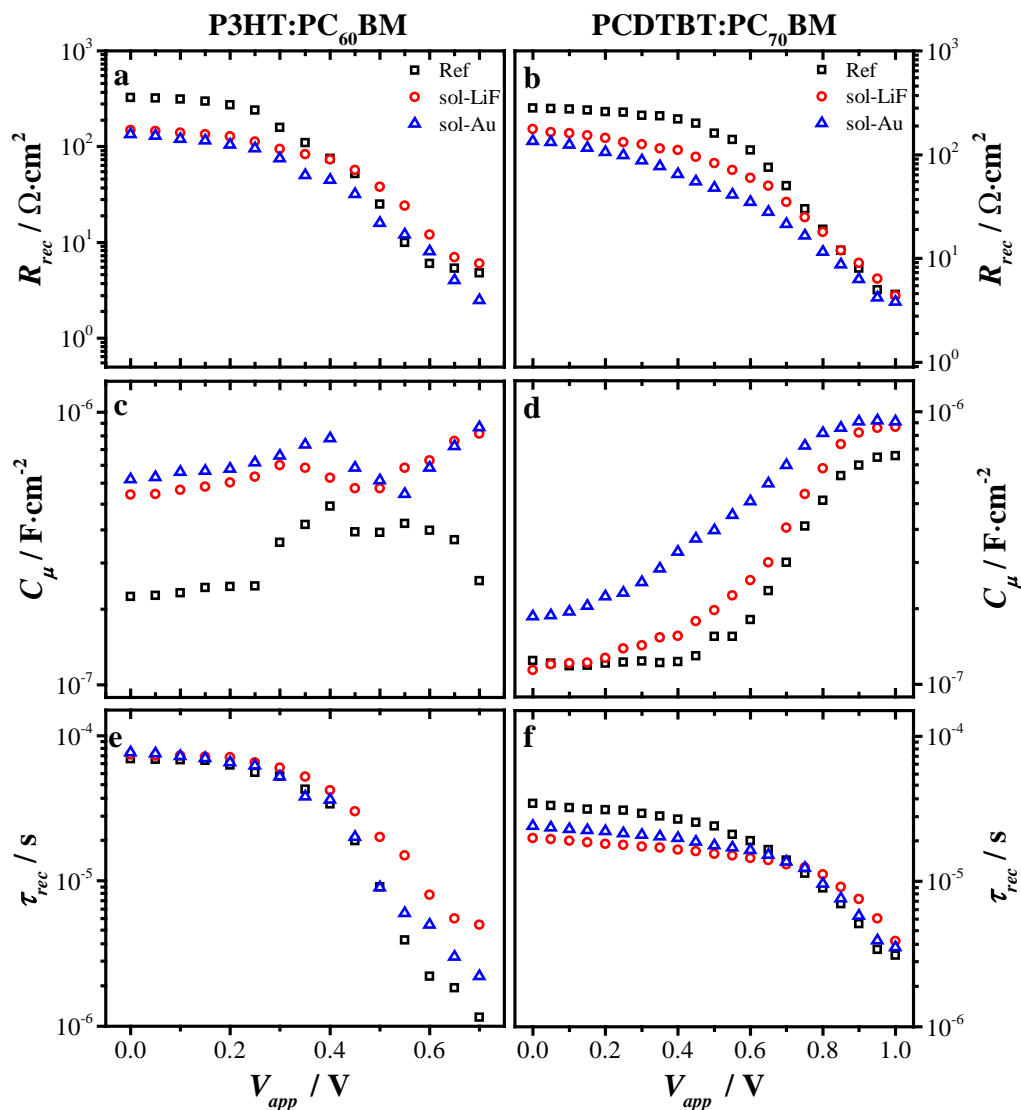


Figure 77. Recombination resistance (R_{rec}), chemical capacitance (C_{μ}) and recombination lifetime (τ_{rec}) vs. applied bias (V_{app}) for the P3HT:PC₆₀BM devices (a, c, and e respectively) and PCDTBT:PC₇₀BM devices (b, d, and f respectively). H. Kurt & C.W. Ow-Yang, Impedance Spectroscopy Analysis of the photophysical dynamics due to the nanostructuring of anode interlayers in organic photovoltaics. *Physica Status Solidi A*. Copyright Wiley-VCH Verlag GmbH & Co. KGaA. Reproduced with permission.

The chemical capacitance (C_{μ}) of an OPV device represents the generation of mobile charge carriers at the BHJ by either photoexcitation or injection in the dark and the resulting induced polarization. The separation of bound excitons also induces a measurable polarization within the active layers. Thus, C_{μ} provides valuable information on how the

modified interlayers affect charge separation and generation in the steady state. For example, the AC voltage superposed on the applied DC bias enables probing the density of states of the polymer blend differentially.^[47] For both BHJ type devices, the C_μ values extracted over the applied bias voltage are presented in Figure 77c and Figure 77d. The increase in C_μ between 0.25-0.5 V applied voltages could be attributed to oxygen doping of mid-gap states due to the ambient processing of P3HT:PC₆₀BM cells. Since the PCDTBT:PC₇₀BM polymer blend has a substantially lower potential for oxygen susceptibility, the C_μ profile was more monotonic. The chemical capacitance for both types of OPVs dramatically increased until the applied bias was comparable to the magnitude of the V_{oc} and saturated as the density of states overlap was diminished.^[66] For both P3HT:PC₆₀BM and PCDTBT:PC₇₀BM OPVs, sol-LiF and sol-Au interlayers improved the chemical capacitance over all bias voltages, suggesting that exciton dissociation was more efficient and the separation of the mobile charges generated was better maintained. While the plasmonic sol-Au interlayers showed superior charge separation/generation for devices of both polymer blends, owing to the enhanced field intensity within the active layer,^[67] the dielectric sol-LiF interlayers provided a higher level of C_μ improvement in P3HT:PC₆₀BM OPVs in comparison to PCDTBT:PC₇₀BM, due to better energy level alignment with the HOMO level of P3HT. The result is due not only to improved charge extraction, but also to the generation of a higher concentration of mobile charge carriers, as the internal bias potential is shifted so as to better facilitate exciton separation.

Coming back to the recombination lifetime, τ_{rec} represents the elapsed time between recombination events and is a fundamental characteristic representing directly the kinetics of all recombination processes overall, including recombination behavior and charge separation. As we were probing devices under operation, τ_{rec} provided valuable insight on charge statics and dynamics under steady-state conditions. In the P3HT:PC₆₀BM OPVs, the average lifetime of charge carriers was 68 μ s under short-circuit conditions. Sol-LiF and sol-Au interlayers improved the average lifetime value to 74 and 76 μ s respectively (Figure 77e). Increasing the applied voltage further revealed that the sol-LiF interlayers extended the charge carrier lifetime. On the other hand, both interlayers showed a lower recombination lifetime profile in the PCDTBT:PC₇₀BM blend below 0.7 V applied bias (Figure 77f). Considering the fullerene ratio^[42] and thinner^[68] nature of PCDTBT:PC₇₀BM

blend, the PC₇₀BM domains have a higher percentage of contact with the modified interlayers, which could increase the recombination flux and lower the recombination lifetime as a consequence.

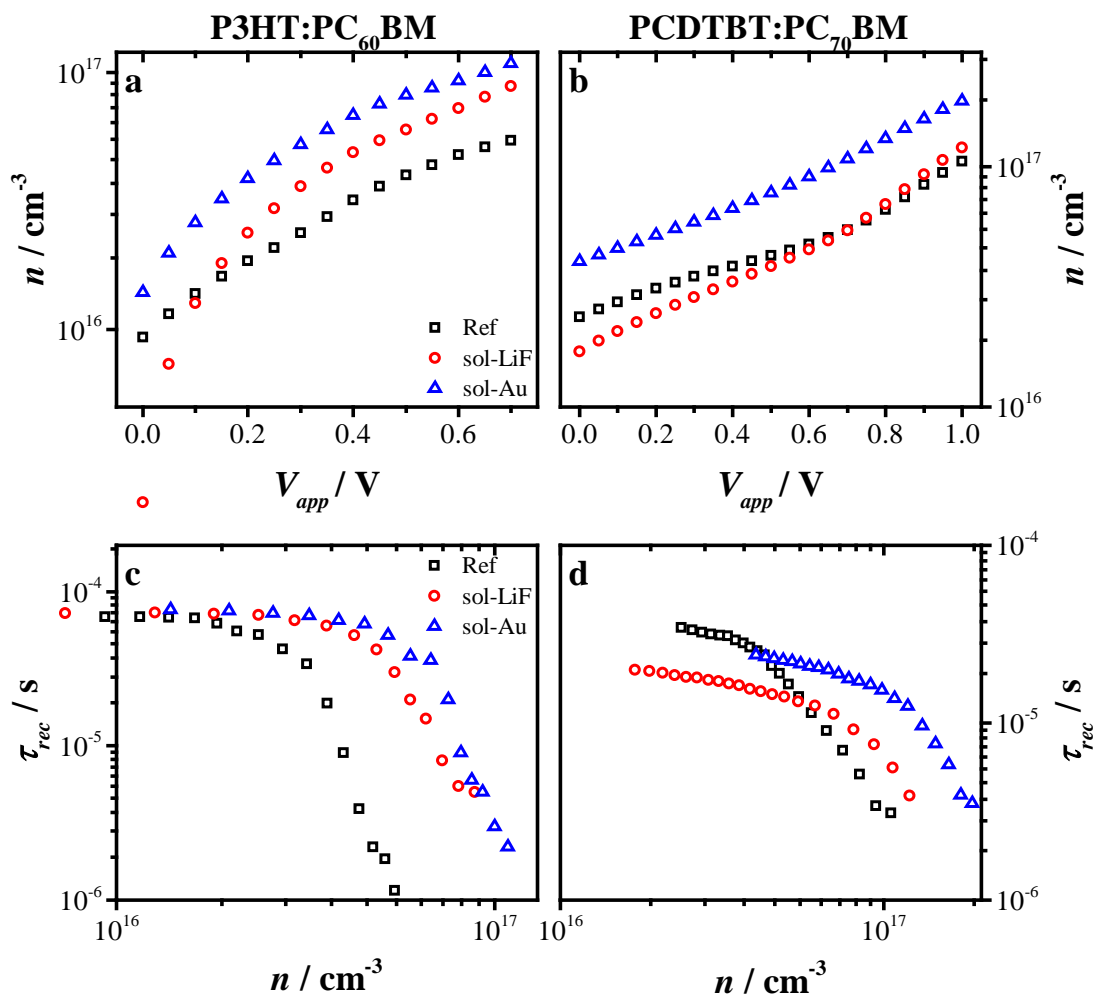


Figure 78. Mobile charge carrier density (n) vs applied bias (V_{app}) for the a) P3HT:PC₆₀BM devices and b) PCDTBT:PC₇₀BM devices. Recombination lifetime (τ_{rec}) vs. mobile charge carrier density (n) for the c) P3HT:PC₆₀BM devices and d) PCDTBT:PC₇₀BM devices. H. Kurt & C.W. Ow-Yang, Impedance Spectroscopy Analysis of the photophysical dynamics due to the nanostructuring of anode interlayers in organic photovoltaics. *Physica Status Solidi A*. Copyright Wiley-VCH Verlag GmbH & Co. KGaA. Reproduced with permission.

4.3.2. Charge Carrier Density

The charge carrier density in Figure 78a and Figure 78b was obtained by integrating the chemical capacitance over applied voltage. The initial charge carrier density (n_0), *i.e.* under short-circuit conditions, was extracted using the charge carrier flux (J_{sc}/qd) under one sun and the transit time.^[66] While the mobile charge carrier concentration had increased with applied bias in all devices, the higher concentration values were observed in both of the BHJ type devices containing sol-Au modified interlayers. We attributed this trend to field enhancement within the active layer, even though the charge carrier lifetime profile was inferior to the reference devices. The plasmonic improvement of sol-Au interlayers was more pronounced in PCDTBT OPVs due to more overlap between the LSPR and the EQE characteristics of PCDTBT:PC₇₀BM blend.^[7,69] In contrast, no charge carrier increase was observed in the sol-LiF-modified OPV's spectral response profile, since they do not exhibit plasmonic response in the visible spectrum.^[43]

In comparison to reference devices, both sol-LiF and sol-Au interlayers induced a higher number of mobile charge carriers. Sol-Au interlayers achieved this improvement through plasmonic field enhancement, while sol-LiF interlayers improved the separation of exciton pairs through induced polarization at the anode and more favorable anode energy alignment with donor polymers.

It appeared that the mobile charge carrier concentration and recombination lifetime were the two key parameters determining device performance. For both BHJ types, two different regimes of charge carrier concentration and recombination lifetime were revealed (Figure 78c and Figure 78d). The intersection of these regimes coincided approximately with the maximum power point (MPP) of the device characteristics. The P3HT:PC₆₀BM OPVs with modified interlayers showed a higher recombination lifetime for substantially higher charge carrier concentrations in comparison to the reference cells. In the case of the PCDTBT:PC₇₀BM OPVs, the reference devices showed a higher lifetime at low charge carrier concentrations compared to the sol-LiF modified devices. However, in the high charge carrier concentration regime, the sol-LiF modified devices increasingly surpassed the carrier lifetime of the reference devices. Clearly, the charge extraction plays a vital role in extending apparent recombination lifetime. Moreover, without adversely impacting the

recombination lifetime, the charge carrier concentration of sol-Au interlayers improved the drift current.^[52]

4.3.3. Recombination Rate and Order

The recombination rate (k_{rec}) encompasses all of the effects of recombination-related losses,^[70] and analyzing k_{rec} enables us to evaluate the correlated behavior of $n-n_0$ and τ_{rec} (Equation 6). For applied biases below V_{oc} , the reference devices showed a lower recombination rate in comparison to devices with modified interlayers. Above V_{oc} , the devices with sol-LiF modified interlayers showed a lower recombination rate as shown in Figure 79a and Figure 79b. Even though the recombination rate results suggested that modified interlayers increased recombination, one should always consider the generated charge carrier density in parallel. The improvement in charge carrier density was extrapolated from the chemical capacitance and the short-circuit current; it suggested that PCE had improved as a result of lower recombination losses.^[70]

The recombination order (δ) (from Equation 7) provides insight into the dominant recombination mechanism. $\delta = 1$ indicates that recombination of mobile charge carrier occurred via deep traps within the band gap. $\delta = 2$ is associated with the bimolecular recombination of mobile electrons and holes within BHJ. $\delta > 2$ implies significant surface recombination and non-ideal carrier gradients due to interfacial heterogeneity especially in considerably thin devices, which interfaces plays a vital role.^[71]

In the P3HT:PC₆₀BM BHJ OPVs, due to induced field gradients and surface recombination at the BHJ interfaces resulting from oxygen doping, the sol-LiF interlayers lowered the recombination order in Figure 79c and Figure 79d, indicating improved charge carrier density and faster charge carrier collection rates, attributed to favorable energy alignment between the PEDOT:PSS and modified ITO anode. At low applied voltages, the dominant mechanism was trap-mediated recombination in sol-LiF modified devices. However, at biases closer to the MPP, bimolecular recombination dominated the recombination behavior. On the other hand, sol-Au interlayers induced mainly bimolecular recombination, attributed to improved plasmon-enhanced charge carrier density at low applied voltages. At biases higher than the MPP, the oxygen-filled mid-gap states lead to an increase in surface recombination, most likely at the BHJ/electrode interfaces. In the PCDTBT:PC₇₀BM BHJ

devices, the recombination order levels remained below 5, owing to the low oxygen susceptibility of the PCDTBT:PC₇₀BM blend. Both sol-LiF and sol-Au interlayers lowered the recombination order, and bimolecular recombination was the dominant mechanism over the range of 0 V up to V_{oc} —consistent with the dipole field of the sol-LiF interlayers decreasing the Coulombic attraction of holes to the ITO anode and repelling mobile electrons to the Al cathode. The electric field gradient was compensated at the sol-LiF interlayers and lowered the recombination losses closer to the MPP point. Further lowering of the recombination order was achieved by sol-LiF interlayers (Figure 79c and Figure 79d).

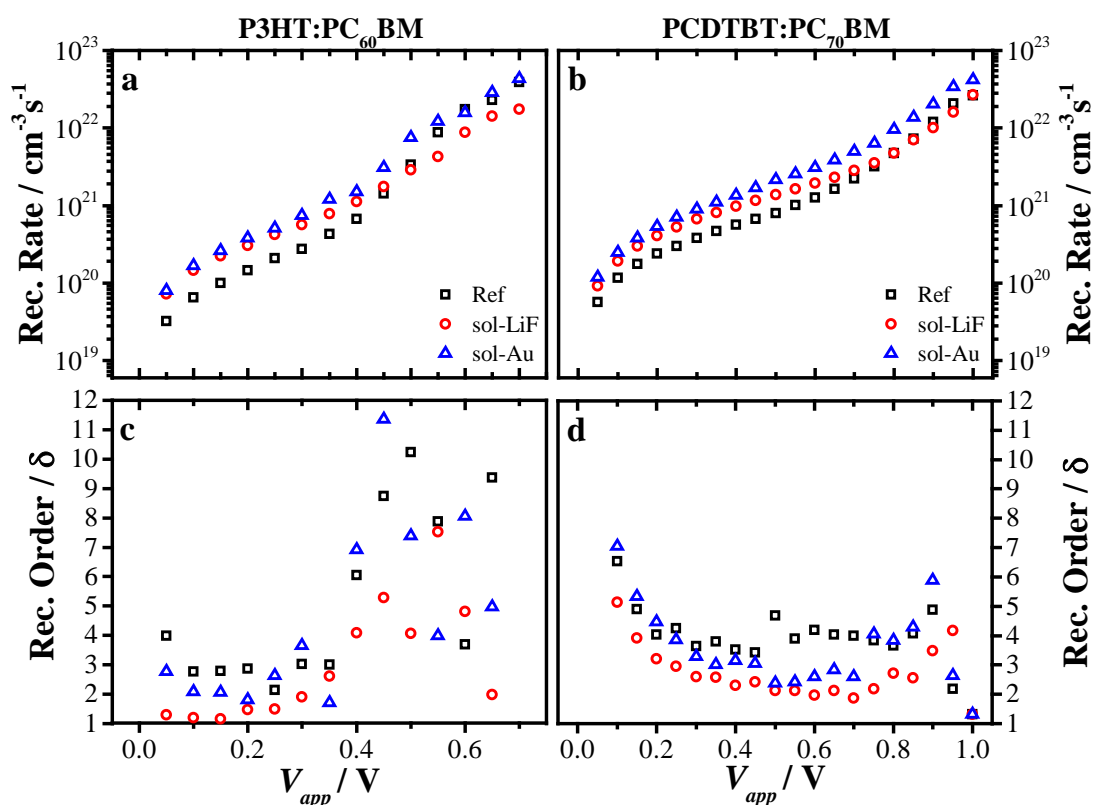


Figure 79. Recombination rate vs. applied bias for the a) P3HT:PC₆₀BM devices and b) PCDTBT:PC₇₀BM devices. Recombination order vs. applied bias for the c) P3HT:PC₆₀BM devices and d) PCDTBT:PC₇₀BM devices. H. Kurt & C.W. Ow-Yang, Impedance Spectroscopy Analysis of the photophysical dynamics due to the nanostructuring of anode interlayers in organic photovoltaics. *Physica Status Solidi A*. Copyright Wiley-VCH Verlag GmbH & Co. KGaA. Reproduced with permission.

4.3.4. Charge Transport Kinetics and Mobility

In order to analyze the charge transport kinetics, we evaluated the charge transport lifetime (τ_{tr}), which was extracted from the high-frequency arc of the impedance response of the OPVs. This average time between mobile charge generation and transport to the electrodes represents the mobility within the BHJ and the charge extraction rate. The transit time can be decomposed into two components—transport resistance and transport capacitance.

The transport resistance indicates the ease of charge collection through the electrodes, *i.e.* hindrances to mobility from all interfaces and layers. The reference and sol-Au modified devices showed comparable transport resistance over all applied biases (Figure 80a and Figure 80b), while devices with sol-LiF interlayers showed transport resistance of an order of magnitude lower. In P3HT:PC₆₀BM BHJ OPVs, improvement in the sol-LiF modified devices is consistent with more efficient hole extraction, due to work function modification of ITO by the sol-LiF interlayers, which facilitated an improved energy level alignment between HOMO level of the PEDOT:PSS HTL and ITO anode.^[37] However, in PCDTBT:PC₇₀BM devices, the dominant mobile charge carriers were electrons, owing to a lower (1:4 vs 1:0.6) donor:acceptor ratio. As the anode interlayers determined improvements in PCE, the hole carrier dynamics would be more strongly affected, with limited impact on the electron behavior, in the P3HT:PC₆₀BM OPVs.^[42]

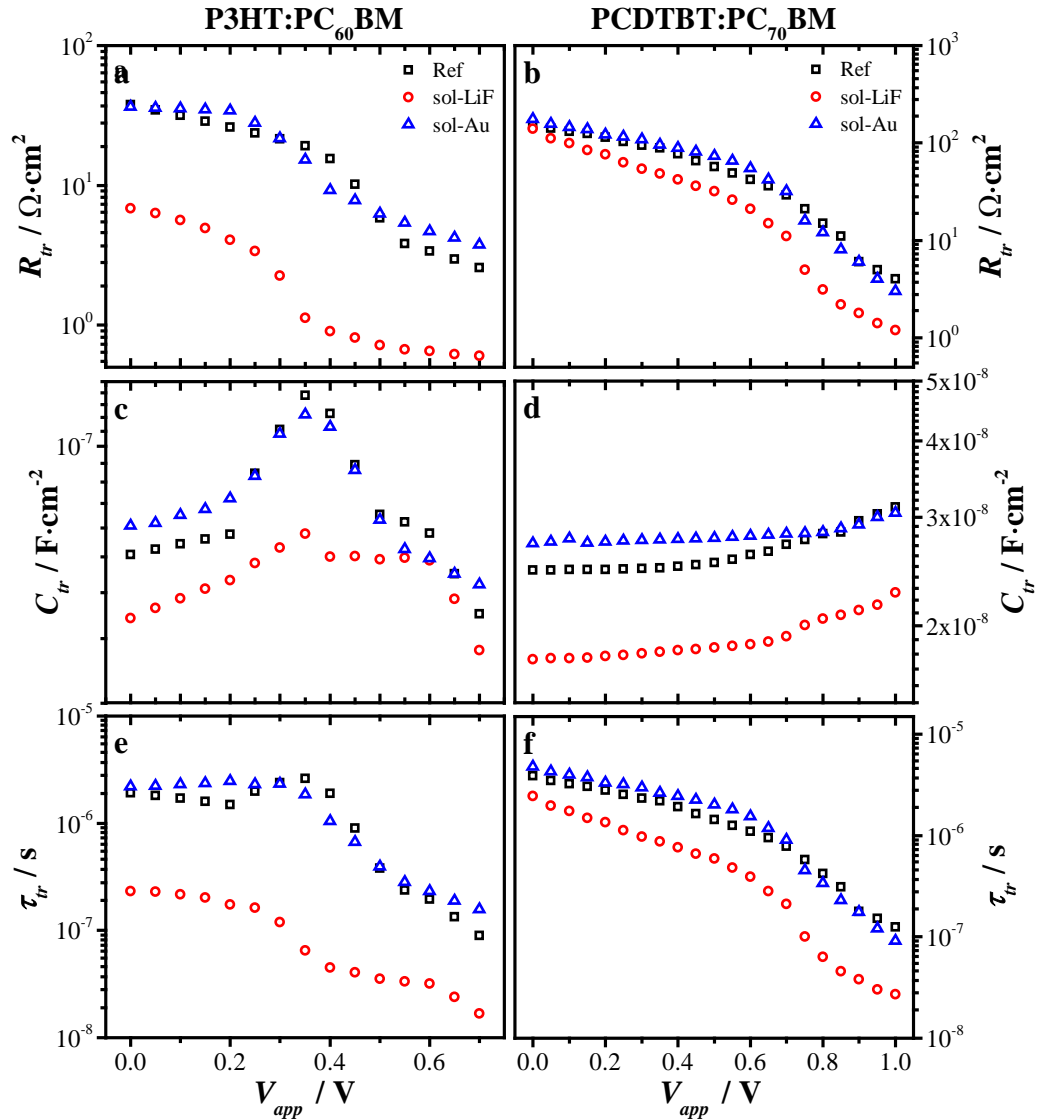


Figure 80. Transport resistance (R_{tr}), transport capacitance (C_{tr}) and transport lifetime (τ_{tr}) vs. applied bias (V_{app}) for the P3HT:PC₆₀BM devices (a, c, and e respectively) and PCDTBT:PC₇₀BM devices (b, d, and f respectively). H. Kurt & C.W. Ow-Yang, Impedance Spectroscopy Analysis of the photophysical dynamics due to the nanostructuring of anode interlayers in organic photovoltaics. *Physica Status Solidi A*. Copyright Wiley-VCH Verlag GmbH & Co. KGaA. Reproduced with permission.

On the other hand, the transport capacitance originates from the polarization of mobile charge carriers at interfaces and interlayers, prior to being extracted through their respective electrodes. In parallel with transport resistances, the sol-Au modified and reference P3HT:PC₆₀BM devices showed similar characteristics, except at low applied voltages. Here the polarization levels were slightly higher at low voltages, while the oxygen-filled mid-gap

states perturbed the charge polarization around 0.3-0.5 V.^[60] In contrast, the sol-LiF modified P3HT:PC₆₀BM devices did not show the effects of significant mid-gap trap filling, possibly due to the traps already having been oxidized. The PCDTBT:PC₇₀BM devices showed similar characteristics for both types of interlayers. The transport capacitance values were significantly smaller, suggesting faster charge extraction through the sol-LiF interlayers. The lowered transport capacitance of sol-LiF interlayers is consistent with lateral depolarization between sol-LiF particles, which lead to a lowered interfacial dipole and better electron blocking.^[31,43]

Table 8. The estimated mobility of interlayer-modified and reference devices at open circuit condition under AM1.5G illumination from Equation (8). H. Kurt & C.W. Ow-Yang, Impedance Spectroscopy Analysis of the photophysical dynamics due to the nanostructuring of anode interlayers in organic photovoltaics. *Physica Status Solidi A*. Copyright Wiley-VCH Verlag GmbH & Co. KGaA. Reproduced with permission.

BHJ Type	Interlayer	Transport Lifetime [μ s]	Estimated Mobility [$\text{cm}^2\text{V}^{-1}\text{s}^{-1}$]
P3HT:PC ₆₀ BM	-	1.91	8.54×10^{-5}
	sol-LiF	0.23	7.02×10^{-4}
	sol-Au	2.21	7.23×10^{-5}
PCDTBT:PC ₇₀ BM	-	3.87	1.54×10^{-5}
	sol-LiF	2.45	2.43×10^{-5}
	sol-Au	4.79	1.24×10^{-5}

Combining the insights revealed by the transport resistance and capacitance, we can now evaluate the influences of the nanostructured interlayers on τ_{tr} , which represents the average time between extraction losses and is directly related to the extraction rate, collection

efficiency, and mobility. Since the transport capacitance values were considerably smaller, τ_{tr} was mostly dominated by the transport resistance. Sol-LiF interlayers provided an order of magnitude lower τ_{tr} , compared to sol-Au interlayers and the control P3HT:PC₆₀BM devices (Figure 80e). On the other hand, τ_{tr} was improved to a more limited degree in PCDTBT: PC₇₀BM (Figure 80f). We attribute this difference to a mismatch of ~0.23 eV between HOMO level of PCDTBT donor polymer and work-function of sol-LiF modified ITO anode. We summarize the estimated level of global charge mobility in interlayer-modified and reference devices for both BHJ types in Table 8.

4.3.5. Charge Recombination Probability

The competition between recombination and charge transport kinetics ultimately determines the probability for charge carrier collection, prior to recombination. The probability of charge recombination, γ , can be extracted from the ratio between the recombination rate (k_{rec}), and extraction (k_{ext})^[70] and represents the number of charge carriers expected to recombine between each charge collection event:

$$k_{rec} \propto \frac{1}{\tau_{rec}}; k_{ext} \propto \frac{1}{\tau_{tr}} \quad (9)$$

$$\gamma \propto \frac{k_{rec}}{k_{ext}} \propto \frac{\tau_{tr}}{\tau_{rec}} \quad (10)$$

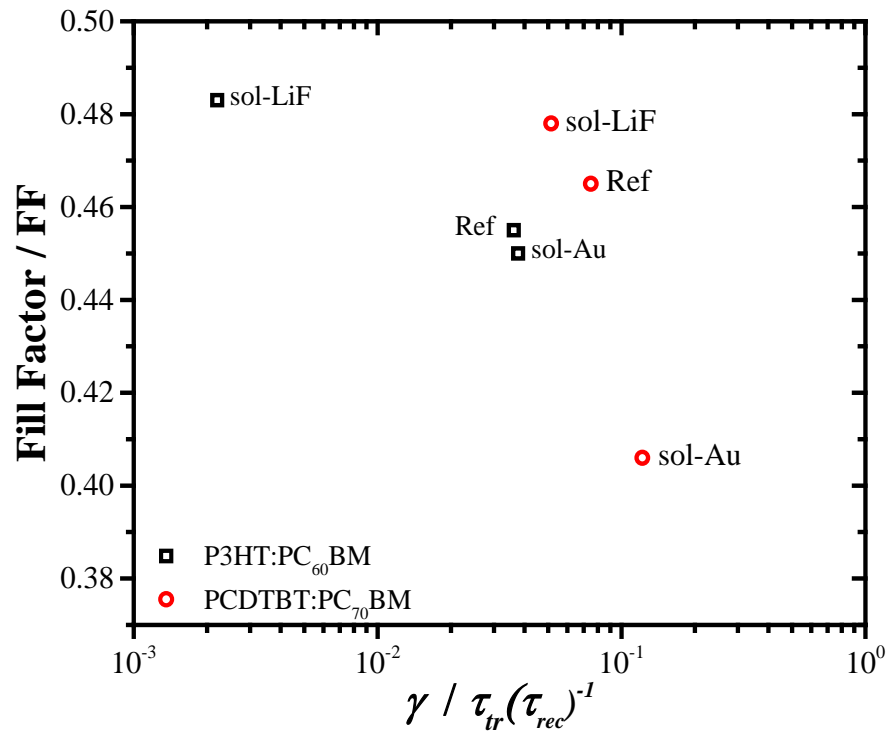


Figure 81. Fill factor (FF) of the photovoltaic cells vs. the estimated probability of charge recombination, γ , for each reference and interlayer-modified device. H. Kurt & C.W. Ow-Yang, Impedance Spectroscopy Analysis of the photophysical dynamics due to the nanostructuring of anode interlayers in organic photovoltaics. *Physica Status Solidi A*. Copyright Wiley-VCH Verlag GmbH & Co. KGaA. Reproduced with permission.

The improved charge transport kinetics of BHJ OPV devices with sol-LiF interlayer modification enabled lowering of the recombination probability between each transport process. The lowered γ strongly correlated with the fill factor of sol-LiF modified devices in Figure 81. In the P3HT:PC₆₀BM OPV devices, the fill factor had increased to 48.3%, whereas it remained at 45% for reference devices. For sol-LiF interlayers, an order of magnitude drop in the recombination probability contributed to the improvement in fill factor. On the other hand, sol-Au interlayers had increased the recombination probability through increased charge carrier density within the device, particularly in PCDTBT:PC₇₀BM devices. The increased recombination probability lowered the fill factor from 46.5% to 40.6%.

The surface dipole induced by the sol-LiF interlayers appeared to have facilitated exciton separation and increased the density of mobile charge carriers within the devices. The induced dipole field of sol-LiF increased the electric field gradient from the BHJ and improved charge separation for the bias applied, leading to increased fill factor values. Moreover, the induced dipole effectively repelled the mobile electrons and provided more efficient electron blocking than the generic PEDOT:PSS HTL at the ITO anode. As a consequence, the improved hole extraction efficiency and increased global transport rates of mobile charges contributed to the substantially increased J_{sc} .

On the other hand, the plasmonic enhancement of sol-Au interlayers boosted the charge generation considerably through increased field density within the BHJ. However, sol-Au interlayers contributed to poorer transport kinetics and sub-par electron blocking properties. The trade-off between the improved generation rate and the poorer transport properties led to a significantly diminished fill factor, particularly in the case of PCDTBT:PC₇₀BM BHJ OPVs. Even though the EQE profile of PCDTBT:PC₇₀BM BHJ was highly compatible with the LSPR of the sol-Au interlayers, the work function of gold (5.1 eV) mismatched with the HOMO level of PCDTBT donor polymer.

This work has clearly shown that IS is a powerful technique that enables one to elucidate the correlations between recombination and extraction events separately, rather than tracking multivariate device characteristics such as fill factor.

4.4. Conclusion

We have evaluated two distinct nanostructured anode interlayers in two BHJ type OPVs *in-operando* using impedance spectroscopy.

The sol-LiF interlayers tuning the work function of the ITO anode in P3HT:PC₆₀BM and PCDTBT:PC₇₀BM BHJ OPV devices were shown to have improved the energy alignment of the modified ITO with the HOMO level of the HTL polymer. This improvement in efficiency was uniform across the entire visible spectral range. By analyzing the impedance response, we have established that the more favorable energy alignment facilitated charge transport and extraction through decreased charge carrier transit lifetime, *i.e.* through improvement of charge collection efficiency.

The sol-Au interlayers evaluated in BHJ OPV devices with different spectral absorption profiles, enabled comparison of the different degrees of overlap between the plasmonic response of the sol-Au interlayer and the spectrum-dependent sensitivity of BHJ absorption. The sol-Au interlayers improved J_{sc} for P3HT:PC₆₀BM and PCDTBT:PC₇₀BM by 10% and 14% respectively, consistent with a corresponding increase in charge carrier density revealed by IS analysis. Such an increase was a consequence of plasmonic field enhancement within the active layers, supported by FDTD simulation studies showing that the absorption was improved due to the field enhancement within BHJ active layer. IS analysis also revealed that the increase in mobile charge carriers did not change charge transit dynamics significantly, in comparison to the reference devices.

The competition between recombination and charge transport kinetics was revealed to be the determining factor for changes in FF in the BHJ OPVs studied. The ratio of recombination and charge transport rates showed a good correlation with the fill factors achieved. IS revealed that the improved charge transport kinetics in the BHJ device can be correlated to the location of the maximum power point (MPP) in device characteristics and compensate for the increased recombination rate from increased charge generation. These results show that IS can be an essential and unique tool to probe the functional anode interlayers by decoupling their individual contributions to OPV performance. By analyzing the charge carrier dynamics of nanostructured anode interlayers using IS, we have demonstrated that the dominant improvement mechanisms can be distinguished.

Chapter 5: Summary

We had begun the overall study described in this dissertation motivated by a hypothesis that nanostructuring the interface between the ITO anode and the organics in BHJ OPVs enable tuning device performance. Work function tuning could remediate the problem of low hole collection efficiency in organic photovoltaics, which are hampered by the energy mismatch at the anode interface. Meanwhile, tuning the photophysical response spectrum of the interlayer can improve charge generation efficiency.

First, by using a diblock copolymer-based self-assembly technique, we had produced sol-LiF and sol-Au nanoparticle dispersions on various surfaces to enable tunability of surface properties of the anode. We had characterized the surface structure and physicochemical properties of sol-LiF and sol-Au modified surfaces thoroughly. We had contributed to the improvement of uniformity of sol-LiF dispersion at higher deposition cycles, while limiting the surface roughness to below 8 nm, and demonstrated that a higher number of sol-LiF depositions enabled achieving a surface work function of -5.30 eV.

Additionally, we had observed that sol-Au nanoparticles can induce incoming electric field enhancement in the close vicinity of their surfaces. Especially in thin film photovoltaics, the improvement in absorption of sub-100 nm active layers is a compelling imperative. Sol-Au nanostructure arrays on ITO surfaces could improve the absorption of these thin layers of organic donor polymers in pursuit of the improved photovoltaic device efficiencies.

Secondly, we had also demonstrated that dielectric sol-LiF interlayers improved the OPV device performance through improving the energy level alignment. Evidently, different levels of sol-LiF surface coverage show optimized device performance due to the different HOMO levels of the donor polymers in spite of the using identical hole transport layer (PEDOT:PSS). In parallel, sol-Au interlayers significantly improved the device performance through increased short circuit density in the expense of loss in the fill factor implying increased charge generation rate. However, a more detailed characterization was in need for identifying the underlying improvement mechanisms.

Thirdly, we established the use of IS analysis to elucidate the mechanisms by which the nanostructured ITO anode interlayers improved BHJ OPV performance. The sol-LiF interlayers tuning the work function of the ITO anode in P3HT:PC₆₀BM and PCDTBT:PC₇₀BM BHJ OPV devices were shown to have improved the energy alignment of the modified ITO with the HOMO level of the HTL polymer. This improvement in efficiency was uniform across the entire visible spectral range. By analyzing the impedance response, we have established that the more favorable energy alignment facilitated charge transport and extraction through decreased charge carrier transit lifetime, *i.e.* through improvement of charge collection efficiency.

The sol-Au interlayers evaluated in BHJ OPV devices with different spectral absorption profiles, enabled comparison of the different degrees of overlap between the plasmonic response of the sol-Au interlayer and the spectrum-dependent sensitivity of BHJ absorption. The sol-Au interlayers improved J_{sc} for P3HT:PC₆₀BM and PCDTBT:PC₇₀BM by 10% and 14% respectively, consistent with a corresponding increase in charge carrier density revealed by IS analysis. Such an increase was a consequence of plasmonic field enhancement within the active layers, supported by FDTD simulation studies showing that the absorption was improved due to the field enhancement within BHJ active layer. IS analysis also revealed that the increase in mobile charge carriers did not change charge transit dynamics significantly, in comparison to the reference devices.

Thus by these three sub-studies, we have proven that by nanostructuring the ITO anode interlayer, the performance of BHJ OPVs can be engineered via tuning of the surface work function and of the photoabsorption and emission behavior of the interlayer.

References

- [1] B. Kippelen, J.-L. Brédas, *Energy Environ. Sci.* **2009**, *2*, 251.
- [2] F. C. Krebs, T. Tromholt, M. Jørgensen, *Nanoscale* **2010**, *2*, 873.
- [3] Y. Liu, J. Zhao, Z. Li, C. Mu, W. Ma, H. Hu, K. Jiang, H. Lin, H. Ade, H. Yan, *Nat. Commun.* **2014**, *5*, 5293.
- [4] M. A. Green, K. Emery, Y. Hishikawa, W. Warta, E. D. Dunlop, *Prog. Photovoltaics Res. Appl.* **2015**, *23*, 1.
- [5] B. Xu, Z. Zheng, K. Zhao, J. Hou, *Adv. Mater.* **2015**, n/a.
- [6] H. Ma, H.-L. Yip, F. Huang, A. K.-Y. Jen, *Adv. Funct. Mater.* **2010**, *20*, 1371.
- [7] H. A. Atwater, A. Polman, *Nat. Mater.* **2010**, *9*, 205.
- [8] G. Li, V. Shrotriya, J. Huang, Y. Yao, T. Moriarty, K. Emery, Y. Yang, *Nat. Mater.* **2005**, *4*, 864.
- [9] E. Ratcliff, B. Zacher, N. Armstrong, *J. Phys. ...* **2011**, 1337.
- [10] J. S. Kim, J. H. Park, J. H. Lee, J. Jo, D.-Y. Kim, K. Cho, *Appl. Phys. Lett.* **2007**, *91*, 112111.
- [11] M. Gliboff, H. Li, K. M. Knesting, A. J. Giordano, D. Nordlund, G. T. Seidler, J.-L. Brédas, S. R. Marder, D. S. Ginger, *J. Phys. Chem. C* **2013**, *117*, 15139.
- [12] M. Gliboff, L. Sang, K. M. Knesting, M. C. Schalnatt, A. Mudalige, E. L. Ratcliff, H. Li, A. K. Sigdel, A. J. Giordano, J. J. Berry, D. Nordlund, G. T. Seidler, J.-L. Brédas, S. R. Marder, J. E. Pemberton, D. S. Ginger, *Langmuir* **2013**, *29*, 2166.
- [13] M. G. Helander, Z. B. Wang, J. Qiu, M. T. Greiner, D. P. Puzzo, Z. W. Liu, Z. H. Lu, *Science* **2011**, *332*, 944.
- [14] C.-Y. Li, T.-C. Wen, T.-F. Guo, *J. Mater. Chem.* **2008**, *18*, 4478.
- [15] B. Kang, L. W. Tan, S. R. P. Silva, *Appl. Phys. Lett.* **2008**, *93*, 133302.
- [16] Y. Zhou, C. Fuentes-Hernandez, J. Shim, J. Meyer, A. J. Giordano, H. Li, P. Winget,

- T. Papadopoulos, H. Cheun, J. Kim, M. Fenoll, A. Dindar, W. Haske, E. Najafabadi, T. M. Khan, H. Sojoudi, S. Barlow, S. Graham, J.-L. Brédas, S. R. Marder, A. Kahn, B. Kippelen, *Science* **2012**, *336*, 327.
- [17] I. P. Murray, S. J. Lou, L. J. Cote, S. Loser, C. J. Kadleck, T. Xu, J. M. Szarko, B. S. Rolczynski, J. E. Johns, J. Huang, L. Yu, L. X. Chen, T. J. Marks, M. C. Hersam, *J. Phys. Chem. Lett.* **2011**, *2*, 3006.
- [18] S. Chaudhary, H. Lu, A. M. Müller, C. J. Bardeen, M. Ozkan, *Nano Lett.* **2007**, *7*, 1973.
- [19] V. Shrotriya, G. Li, Y. Yao, C.-W. Chu, Y. Yang, *Appl. Phys. Lett.* **2006**, *88*, 073508.
- [20] M. D. Irwin, D. B. Buchholz, A. W. Hains, R. P. H. Chang, T. J. Marks, *Proc. Natl. Acad. Sci.* **2008**, *105*, 2783.
- [21] K. X. Steirer, P. F. Ndione, N. E. Widjonarko, M. T. Lloyd, J. Meyer, E. L. Ratcliff, A. Kahn, N. R. Armstrong, C. J. Curtis, D. S. Ginley, J. J. Berry, D. C. Olson, *Adv. Energy Mater.* **2011**, *1*, 813.
- [22] W.-J. Yoon, P. R. Berger, *Appl. Phys. Lett.* **2008**, *92*, 013306.
- [23] H.-L. Yip, S. K. Hau, N. S. Baek, A. K.-Y. Jen, *Appl. Phys. Lett.* **2008**, *92*, 193313.
- [24] A. Turak, *RSC Adv.* **2013**, *3*, 6188.
- [25] L. S. C. Pingree, B. A. MacLeod, D. S. Ginger, *J. Phys. Chem. C* **2008**, *112*, 7922.
- [26] H. Yan, P. Lee, N. R. Armstrong, A. Graham, G. A. Evmenenko, P. Dutta, T. J. Marks, *J. Am. Chem. Soc.* **2005**, *127*, 3172.
- [27] K. W. Wong, H. L. Yip, Y. Luo, K. Y. Wong, W. M. Lau, K. H. Low, H. F. Chow, Z. Q. Gao, W. L. Yeung, C. C. Chang, *Appl. Phys. Lett.* **2002**, *80*, 2788.
- [28] E. Stratakis, E. Kymakis, *Mater. Today* **2013**, *16*, 133.
- [29] T. Aytun, A. Turak, I. Baikie, G. Halek, C. W. Ow-Yang, *Nano Lett.* **2012**, *12*, 39.
- [30] H. Kurt, J. Jia, Y. Shigesato, C. W. Ow-Yang, *J. Mater. Sci. Mater. Electron.* **2015**,

- 26, 9205.
- [31] C. W. Ow-Yang, J. Jia, T. Aytun, M. Zamboni, A. Turak, K. Saritas, Y. Shigesato, *Thin Solid Films* **2014**, 559, 58.
- [32] M. Rubin, *Sol. Energy Mater.* **1985**, 12, 275.
- [33] T. A. F. König, P. A. Ledin, J. Kerszulis, M. A. Mahmoud, M. A. El-Sayed, J. R. Reynolds, V. V Tsukruk, *ACS Nano* **2014**, 8, 6182.
- [34] H. H. Li, *J. Phys. Chem. Ref. Data* **1976**, 5, 329.
- [35] A. D. Rakic, A. B. Djurišić, J. M. Elazar, M. L. Majewski, *Appl. Opt.* **1998**, 37, 5271.
- [36] P. B. Johnson, R. W. Christy, *Phys. Rev. B* **1972**, 6, 4370.
- [37] H. Kurt, J. Jia, Y. Shigesato, C. W. Ow-Yang, *J. Mater. Sci. Mater. Electron.* **2015**, 26, 9205.
- [38] Y. Sato, T. Ashida, N. Oka, Y. Shigesato, *Appl. Phys. Express* **2010**, 3, 061101.
- [39] V. Klimov, G.-Y. Guo, M. Pikhota, **2014**.
- [40] R. U. Tok, C. Ow-Yang, K. Sendur, *Opt. Express* **2011**, 19, 22731.
- [41] M. Campoy-Quiles, J. Nelson, D. D. C. Bradley, P. G. Etchegoin, *Phys. Rev. B* **2007**, 76, 235206.
- [42] A. Guerrero, B. Dörling, T. Ripolles-Sanchis, M. Aghamohammadi, E. Barrena, M. Campoy-Quiles, G. Garcia-Belmonte, *ACS Nano* **2013**, 7, 4637.
- [43] A. Turak, T. Aytun, C. W. Ow-Yang, *Appl. Phys. Lett.* **2012**, 100, 253303.
- [44] S. Suckow, T. M. Pletzer, H. Kurz, *Prog. Photovoltaics Res. Appl.* **2014**, 22, 494.
- [45] E. L. Ratcliff, J. Meyer, K. X. Steirer, N. R. Armstrong, D. Olson, A. Kahn, *Org. Electron.* **2012**, 13, 744.
- [46] O. Bubnova, Z. U. Khan, H. Wang, S. Braun, D. R. Evans, M. Fabretto, P. Hojati-Talemi, D. Dagnelund, J.-B. Arlin, Y. H. Geerts, S. Desbief, D. W. Breiby, J. W.

- Andreasen, R. Lazzaroni, W. M. Chen, I. Zozoulenko, M. Fahlman, P. J. Murphy, M. Berggren, X. Crispin, *Nat. Mater.* **2014**, *13*, 190.
- [47] G. Garcia-Belmonte, A. Guerrero, J. Bisquert, *J. Phys. Chem. Lett.* **2013**, *4*, 877.
- [48] T. Aernouts, W. Geens, J. Poortmans, P. Heremans, S. Borghs, R. Mertens, *Thin Solid Films* **2002**, *403-404*, 297.
- [49] C. Waldauf, M. C. Scharber, P. Schilinsky, J. A. Hauch, C. J. Brabec, *J. Appl. Phys.* **2006**, *99*, 104503.
- [50] T. Strobel, C. Deibel, V. Dyakonov, *Phys. Rev. Lett.* **2010**, *105*, 266602.
- [51] A. Wagenpfahl, C. Deibel, V. Dyakonov, *IEEE J. Sel. Top. Quantum Electron.* **2010**, *16*, 1759.
- [52] G. Garcia-Belmonte, A. Munar, E. M. Barea, J. Bisquert, I. Ugarte, R. Pacios, *Org. Electron.* **2008**, *9*, 847.
- [53] M. Möller, J. P. Spatz, A. Roescher, *Adv. Mater.* **1996**, *8*, 337.
- [54] T. Lohmueller, E. Bock, J. P. Spatz, *Adv. Mater.* **2008**, *20*, 2297.
- [55] R. Glass, M. Möller, J. P. Spatz, *Nanotechnology* **2003**, *14*, 1153.
- [56] M. Al-Ibrahim, *Sol. Energy Mater. Sol. Cells* **2004**, *85*, 13.
- [57] L. Huo, J. Hou, S. Zhang, H.-Y. Chen, Y. Yang, *Angew. Chemie Int. Ed.* **2010**, *49*, 1500.
- [58] T. Ripolles-Sanchis, A. Guerrero, J. Bisquert, G. Garcia-Belmonte, *J. Phys. Chem. C* **2012**, *116*, 16925.
- [59] J. Bisquert, L. Bertoluzzi, I. Mora-sero, G. Garcia-belmonte, *J. Phys. Chem. C* **2014**, *118*, 18983.
- [60] J. a. Carr, S. Chaudhary, *Energy Environ. Sci.* **2013**, *6*, 3414.
- [61] A. Guerrero, S. Loser, G. Garcia-Belmonte, C. J. Bruns, J. Smith, H. Miyauchi, S. I. Stupp, J. Bisquert, T. J. Marks, *Phys. Chem. Chem. Phys.* **2013**, *15*, 16456.

- [62] B. J. Leever, C. A. Bailey, T. J. Marks, M. C. Hersam, M. F. Durstock, *Adv. Energy Mater.* **2012**, *2*, 120.
- [63] M. Heo, H. Cho, J.-W. Jung, J.-R. Jeong, S. Park, J. Y. Kim, *Adv. Mater.* **2011**, *23*, 5689.
- [64] T. K. Mullenbach, Y. Zou, J. Holst, R. J. Holmes, *J. Appl. Phys.* **2014**, *116*, 124513.
- [65] R. Pandey, R. J. Holmes, *Appl. Phys. Lett.* **2012**, *100*, 083303.
- [66] J. I. Basham, T. N. Jackson, D. J. Gundlach, *Adv. Energy Mater.* **2014**, *4*, 1400499.
- [67] J.-L. Wu, F.-C. Chen, Y.-S. Hsiao, F.-C. Chien, P. Chen, C.-H. Kuo, M. H. Huang, C.-S. Hsu, *ACS Nano* **2011**, *5*, 959.
- [68] T. Kirchartz, W. Gong, S. A. Hawks, T. Agostinelli, R. C. I. MacKenzie, Y. Yang, J. Nelson, *J. Phys. Chem. C* **2012**, *116*, 7672.
- [69] L. Lu, Z. Luo, T. Xu, L. Yu, *Nano Lett.* **2013**, *13*, 59.
- [70] D. Bartesaghi, I. D. C. Pérez, J. Kniepert, S. Roland, M. Turbiez, D. Neher, L. J. A. Koster, *Nat. Commun.* **2015**, *6*, 7083.
- [71] T. Kirchartz, J. Nelson, *Phys. Rev. B* **2012**, *86*, 165201.
- [72] P. Lipowsky, N. Hedin, J. Bill, R. C. Hoffmann, A. Ahniyaz, F. Aldinger, L. Bergström, *J. Phys. Chem. C* **2008**, *112*, 5373.

Appendix

Impact of Polyvinylpyrrolidone on the photophysics of ZnO nanocolloids

Hasan Kurt, Ece Alpaslan, Burçin Yıldız, Alpay Taralp and Cleva W. Ow-Yang

Introduction

Zinc oxide remains to be a promising optoelectronic material due to its large direct band gap and high exciton binding energy under ambient conditions. Currently, ZnO nanostructures are utilized in wide range of application fields such as optical waveguides, ultraviolet-visible emitting diodes, gas sensors and solar cells owing to their unique quantum confinement properties.¹ The photophysics of ZnO nanostructures heavily depend on their surface defect chemistry. The surface defects induce ionic oxygen and zinc vacancies depending on the synthesis and processing conditions. Polyvinylpyrrolidone is a wide used homopolymer in various colloidal ZnO nanostructures synthesis such as nanoparticles, nanorods, nanostars, nanoplatelets for shape-directed synthesis and surface passivation. To limit the particle size in order to yield nanoparticle light emitters, ZnO colloids can be synthesized in a polyvinylpyrrolidone (PVP)-containing polar solvent.^{2,3} Because the emission characteristics, such as the relative density of photoactive surface states,⁴ have been shown to vary with the size of the particles and with PVP content,² PVP appears to influence the nucleation and growth of ZnO colloids, and its conformation when adsorbed on the ZnO surface may vary with polymer concentration.

The photophysics of ZnO/PVP nanocolloids was investigated thoroughly in the last two decades. Research efforts were mainly focused on the blue emission from the ZnO colloids coinciding with the auto-fluorescence of PVP around wavelength of 400 nm. The degree of PVP stabilization can quench the trap-state emission and enhance near band-edge emission in ZnO colloids. In this study, we investigate the conformation behavior of PVP chains on the surface of ZnO nanocrystals. Thus, we have applied dynamic NMR techniques to analyze solutions of PVP-modified ZnO colloidal nanoparticles, in order to monitor the interaction between PVP, the ZnO particles, and the solvent molecules; and we interpreted

the results in parallel with complementary investigations using dynamic light scattering, ultraviolet (UV)-visible absorption spectroscopy, and fluorescence spectroscopy. Our study revealed that high-density train conformation of PVP can significantly enhance UV emission of ZnO nanoparticles at wavelength of 310 nm by passivating the surface trap states.

Materials and Methods

Polyvinylpyrrolidone with an average molecular weight of 40,000 were obtained from Sigma Aldrich. PVP-capped ZnO colloidal nanoparticles were synthesized using 4.6 mM zinc acetate dehydrate ($\text{Zn}(\text{CH}_3\text{COO})\cdot 2\text{H}_2\text{O}$, Merck, >99%) and 0.02 M sodium hydroxide in 1-propanol in the presence of 0.05, 0.07 and 0.11 $\text{g}\cdot\text{mL}^{-1}$ PVP. Zinc acetate dissolved in PVP containing 1-propanol solution vigorous stirring at 70°C. After the addition of sodium hydroxide solution, mixture was stirred for 2 minutes at 70°C and quenched in an ice bath. In order to remove the excess polymer from the solution, the mixtures were centrifuged at 125,216 \times g at 18°C for 90 mins (Beckman Coulter Optima Max TL, Indianapolis, IN, USA).

Absorption profile of ZnO colloids were measured in the range of 200-700 nm with a bandwidth of 0.5 nm using UV-Visible absorption spectroscopy (Shimadzu, UV-3150, Kyoto, Japan). The absorption onsets were utilized to extrapolate the band gap energy of ZnO colloids.

The fluorescence spectra were collected with Cary Eclipse Fluorescence Spectrophotometer equipped with xenon flash lamp (Agilent, Santa Clara, CA, USA). Fluorescence contour maps were measured with an excitation range of 230-520 and an emission range of 240-800 nm using Hellma Suprasil quartz cells. The near-band gap emissions and trap-state emissions were identified from fluorescence contour maps with respect to PVP-only samples.

To determine the conformations of the adsorbed polymer on surface of ZnO nanoparticles, dynamic nuclear magnetic resonance (NMR) methods were utilized. The PVP-capped nanoparticle samples (100 μL) were dissolved in 0.5 mL of deuterium oxide (D_2O , 99.9%). NMR spectra were collected using Varian Unity Inova 500 MHz spectrometer (Varian Unity Inova, Palo Alto, CA USA). The spectra were recorded at room temperature with a

500 MHz, 1H-19F (15N-31P), 5 mm PFG, Switchable Probe. Proton NMR spectra were acquired using custom solid and spin-echo sequences (32k data points, acquisition time 1.892 s, 90° pulse of 13.2 μ s width, 10 s repetition delay (τ), and integrated over 16 scans). The first pulse sequence used was 90°_x- τ -90°_y-2 τ , followed by another sequence 90°_y-2 τ -180°_y-2 τ -180°_y-2 τ . 1D C NMR spectra were acquired using S2PUL sequence with proton decoupling spectral width 32 kHz, acquisition time 1.3s, 90° pulse width of 10 μ s, pulse delay time of 5 s.

Chemical shifts were adjusted with respect to the resonance of water at 4.8 ppm. T_1 and T_2 characteristics were recorded. Another set of experiments was designed to deduce the contribution of PVP into the nucleation and growth of colloidal ZnO nanoparticles. This experiment was repeated for two different polymer concentrations: 0.11 g/mL and 0.05 g/mL. In the first group, only PVP in the given two concentrations was dissolved in the propanol solvent. In the second group, again the same amount of PVP was dissolved in 4.6 mM zinc acetate in propanol solution.

In order to verify coordination of PVP with Zn²⁺, Fourier Transform Infrared Spectroscopy (FT-IR) measurements were made (Thermo Scientific, Nicolet IS 10).

The hydrodynamic radii of the PVP-capped ZnO nanoparticles were determined by dynamic light scattering (DLS) using Malvern Zetasizer Nano ZS (Malvern Instruments, ZEN3600, UK) which was equipped with a 633 nm He-Ne laser and operated at an angle of 173° at temperature of 23 \pm 0.10°C. For DLS measurements, samples were diluted with pure 1-propanol by ten fold and adjusted to 1 mL to eliminate multiple scattering events. Data processing is performed by NNLS algorithm using 45 measurement cycles for each samples.

In order to evaluate the polymer-nanoparticle interaction, Fourier transform infrared spectroscopy (Nicolet iS10, Thermo Scientific) was utilized. FTIR spectra were recorded in attenuated total reflection (ATR) mode between 550 and 4000 cm⁻¹ by averaging 64 scans with a resolution of 0.5 cm⁻¹.

Results

In order to estimate the PVP-capped ZnO nanoparticle size, we used two complementary techniques, UV-visible absorption spectroscopy and dynamic light scattering. From absorption spectra, the relative shift in band gap due to quantum confinement can be correlated to the particle radius, r . By extrapolating the linear part of the absorption onset to baseline absorption,¹⁴ the band gap of the colloidal nanoparticles, E_g^* , was determined and compared to the band gap of bulk ZnO, E_g^{bulk} . The change in the band gap energy due to quantum confinement was calculated using Equation 1.¹⁴

$$E_g^* = E_g^{bulk} + \frac{\hbar^2 \pi^2}{2r^2} \left(\frac{1}{m_0 m_e^*} + \frac{1}{m_0 m_h^*} \right) - \frac{1.8e^2}{4\pi \epsilon_r \epsilon_0 r} - \frac{0.124e^4}{\hbar^2 (4\pi \epsilon_r \epsilon_0)^2} \left(\frac{1}{m_0 m_e^*} + \frac{1}{m_0 m_h^*} \right)^{-1} \quad (\text{Equation 1})$$

Where m_0 is mass of an electron, ϵ_0 is permittivity of vacuum, \hbar is reduced Planck constant, m_e^* is effective mass of a conduction band electron ($m_e^* = 0.26$), m_h^* is the effective mass of a valence band hole ($m_h^* = 0.59$), and ϵ_r is the dielectric constant of ZnO ($\epsilon_r = 8.5$).¹⁵

Table 1 summarizes the average hydrodynamic radius of the particle population and estimated nanoparticles size by absorption onset. Analysis of dynamic light scattering of PVP-capped ZnO nanoparticles revealed that increasing PVP concentration actually significantly reduced the hydrodynamic radii of ZnO nanoparticles. In fact, the difference between ZnO nanoparticle size estimated from absorption spectra and hydration shell of ZnO nanoparticles converged at $0.11 \text{ g}\cdot\text{mL}^{-1}$. ZnO nanoparticle batches devoid of PVP presence showed slightly larger estimated radius however hydrodynamic radius of bare ZnO nanoparticles showed dramatically larger hydration shell radius.

Table 1. PVP-capped ZnO nanoparticle size and hydrodynamic radius at different polymer concentrations.

Polymer Concentration [$\text{g}\cdot\text{mL}^{-1}$]	Estimated Radius [nm]	Hydrodynamic Radius [nm]
0	2.74	91
0.05	2.09	2.93
0.07	2.06	2.49
0.11	1.84	2.08

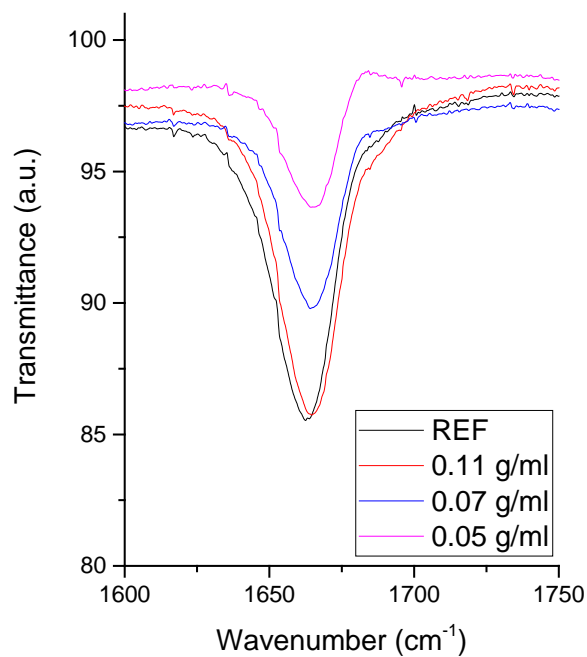


Figure 1. FTIR of C=O bond stretch in different PVP concentrations and without ZnO nanoparticles.

As shown in **Figure 1**, the carbonyl bonds of PVP (C=O) has a resonance at 1662 cm^{-1} which was observed by FT-IR. When ZnO was synthesized in the presence of PVP, the resonance of the C=O in PVP shifted to 1665 cm^{-1} .

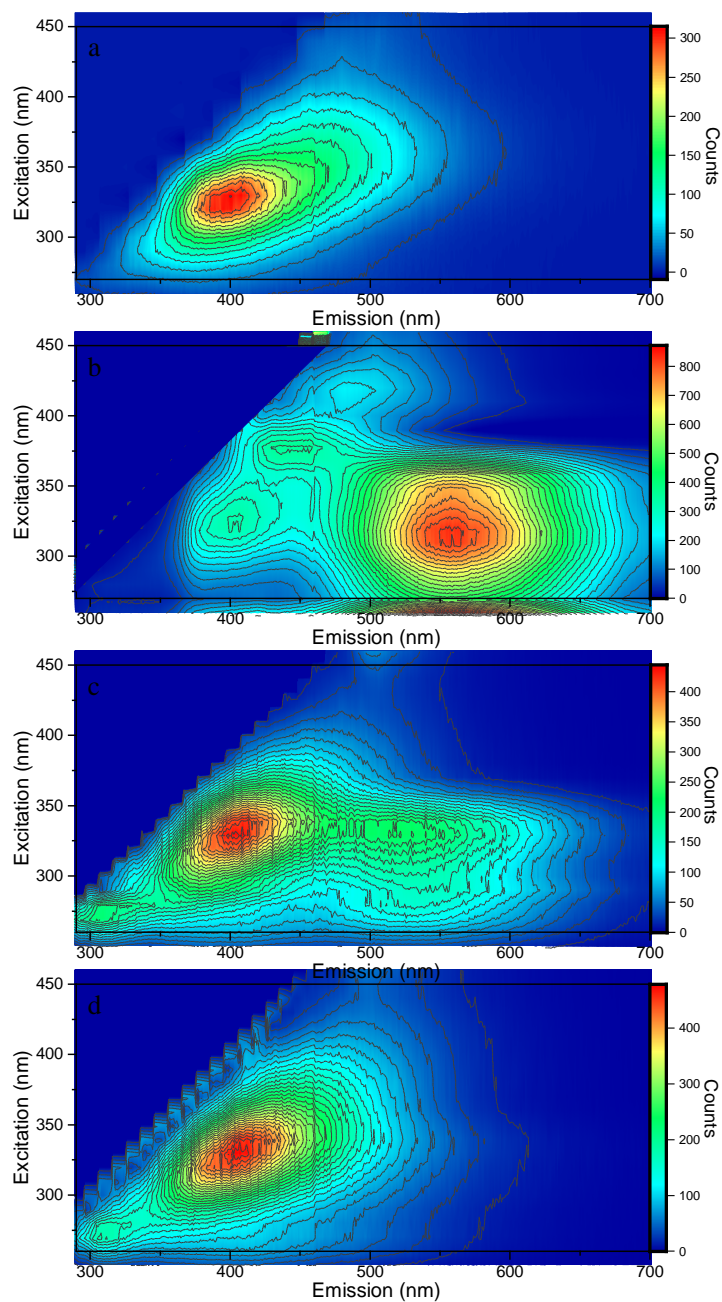


Figure 2. Contour Diagrams of Excitation and Emission Profiles of PVP only (a), PVP-ZnO colloidal solutions with PVP concentration of $0.05 \text{ g}\cdot\text{mL}^{-1}$ (b), $0.07 \text{ g}\cdot\text{mL}^{-1}$ (c) and $0.11 \text{ g}\cdot\text{mL}^{-1}$ (d).

The excitation-emission profile of pure PVP solution show a single dominant peak of emission at wavelength of 400 nm upon an excitation at wavelength of 325 nm. PVP polymer showed similar contour profile over all PVP concentration in the presence of ZnO

nanoparticles. ZnO nanoparticles showed distinctly diverse excitation-emission profiles depending on the concentration of PVP in the solution. At 0.05 g·mL⁻¹ concentration of PVP, ZnO nanoparticles emitted a strong yellow luminescence at the peak wavelength of 560 nm upon an excitation at wavelength of 316 nm. Also, two minor emission centers were recorded at wavelength of 446 nm under excitation of 378 nm and at wavelength of 488 nm under excitation of 418 nm. These emission readouts were discarded from the analysis due to their resemblance to Xenon flash lamp emissions. At 0.07 g·mL⁻¹ concentration of PVP, ZnO nanoparticles emitted a green luminescence at the peak wavelength of 518 nm upon an excitation at 331 nm. The green emission at 0.07 g·mL⁻¹ was lower in intensity in comparison to yellow emission at 0.05 g·mL⁻¹ concentration of PVP. However, a distinct UV emission was observed at emission peak of 310 nm under excitation of 274 nm. UV emission of 310 nm was also observed in 0.05 g·mL⁻¹ PVP-ZnO colloidal solution with complete disappearance of green and yellow emissions. In the presence of ZnO nanoparticles, excitation-emission profile of PVP was also shifted toward lower excitation wavelengths in relation to emergence of UV emission at wavelength of 310 nm.

In order to evaluate the chemistry of the PVP-ZnO colloidal solution, proton (¹H) and carbon (¹³C) NMR analysis was performed. Figure 3 shows the ¹H-NMR spectra of the 0.11g/mL PVP-functionalized ZnO nanoparticles dissolved in D₂O (the full spectrum can be seen in Figure S2 of the Supporting Information). Each carbon atom in the pyrrolidone ring is associated with a unique hydrogen atom, which is labeled according to their position in Figure 5. As shown in Figure 3, each pyrrolidone hydrogen nucleus reaches resonance at chemical shifts consistent with the previous results of Sesta, *et al.*,¹⁶ with the ¹H-NMR (PVP-functionalized ZnO nanoparticles in D₂O) peaks at δ_{α} = 3.64, δ_4 = 3.30, δ_2 = 2.31, δ_3 =2.01, δ_{β} = 1.73. Figure 4 shows the ¹³C-NMR spectrum of the same sample. Each carbon of the pyrrolidone (Fig.4) reaches resonance at chemical shifts consistent with the previous results of Lipowsky, *et al.*^[72] with the ¹³C-NMR peaks at δ_1 =176.5, δ_{α} = 45, δ_4 = 43, δ_3 =18, δ_{β} = 35, δ_2 = 32. In addition, the spectra also showed the -CH₂ and -CH₃ resonances of the 1-propanol solvent (in which the colloidal particles were synthesized) and -OH resonance of the residual H₂O of D₂O (which is the NMR solvent). Table 2 summarizes the identity

and location of each resonance peak for the solvent in both the proton and the ^{13}C -NMR spectrum.

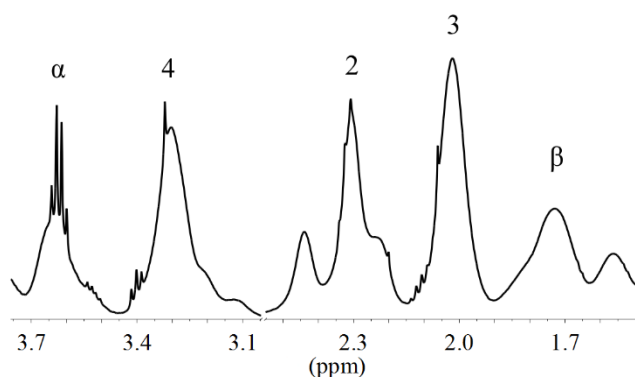


Figure 3. Proton NMR spectra of ZnO particles precipitated in PVP of the concentration 0.11g/mL in D_2O . Peak labels correspond to the H associated with distinct locations in the vinylpyrrolidone mer.

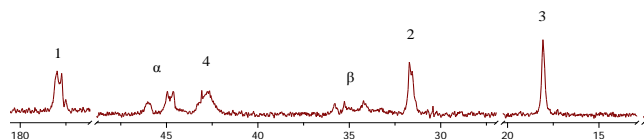


Figure 4. Carbon NMR spectra of ZnO particles precipitated in PVP of the concentration 0.11g/mL in D_2O . Peak labels correspond to specific carbon atoms in the vinylpyrrolidone mer.

Table 2. Chemical shifts of resonance peaks correlated to the solvent structure in the solution of ZnO particles precipitated in PVP at a concentration 0.11 g/mL in H_2O .

Chemical Species	^1H Chemical Shift [ppm]	^{13}C Chemical Shift [ppm]
-OH	4.80	-
-CH ₂ (A)	3.58	64.25
-CH ₂ (C)	1.57	25.89
-CH ₂ (D)	0.88	9.98

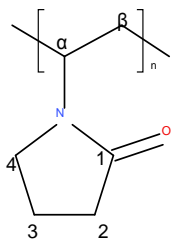


Figure 5. The structure of a vinylpyrrolidone mer

Both the spin-lattice interaction dynamics (represented by the T_1 value) and the spin-spin coupling dynamics (represented by T_2) of the solvent were also monitored for the PVP-functionalized nanoparticles that had precipitated in each different polymer concentration. For each of the ^1H resonance shifts of solvent molecules identified in the Supporting Information, a decreasing trend for T_1 relaxation response to the pulsed NMR field correlating with polymer concentration is observed with the increasing polymer concentration. In the case of the T_2 response, only the $-\text{CH}_2$ and $-\text{CH}_3$ showed a discernible increasing trend with varying functionalizing polymer concentration. Full tabulated values for T_1 and T_2 relaxation data is provided in Supporting Information Table S1 and Table S2.

The ^{13}C -resonance shifts were identified for each C in the propanol molecule, in addition to both spin-lattice and spin-spin relaxation characteristics. For both T_1 and T_2 relaxation times, we observed an increasing trend with increasing polymer concentration (Supporting Information Table S3 and Table S4).

Discussion

PVP-capped ZnO nanoparticles showed higher colloidal stability than the bare ZnO nanoparticles. Bare ZnO particles exhibited a strong tendency to agglomerate and their hydrodynamic radius remained significantly larger than the absorbance-estimated radius. The difference between absorbance-estimated and hydrodynamic radii lowered as the PVP concentration increases suggesting PVP chains have varying levels of adsorption on surface of ZnO nanoparticle. At $0.05 \text{ g}\cdot\text{mL}^{-1}$ of PVP concentration, hydrodynamic radius exhibited almost a nanometer larger values suggesting dangling polymer chains on the nanoparticles surface and effectively increasing solvent hydration shell. Higher concentrations of PVP

concentrations led to more strongly adsorbed polymer layers on nanoparticle surface suggesting loops and train formations and higher level of passivation.

Time domain NMR spectroscopy enabled us to elucidate the influence of polymer concentration on particle growth, by distinguishing the responses of individual ^1H nuclei to an applied magnetic field. As sample preparation for probing the NMR response necessitated combining the propanol solution of PVP-functionalized ZnO nanoparticles with deuterium oxide, the actual NMR sample consisted of PVP adsorbed onto ZnO nanoparticles, with the PVP molecules (and the exposed ZnO surface) well-solvated by propanol and some residual H_2O in the 99.9% pure deuterium oxide. The ^1H -NMR response thus comes from the hydrogen nuclei of PVP, of propanol, and of H_2O . As the relaxation time of the ^1H nuclear spin for the $-\text{CH}_2$ of propanol decreased with increasing polymer concentration, the loss of mobility in higher polymer concentrations suggests that propanol and water molecules become less trapped—*i.e.*, more mobile—in a denser polymer network.

Both the ^1H - and ^{13}C -NMR results showed that $-\text{CH}_3$ (D) resonance of propanol (See Supporting Information Figure S1) appeared at lower ppm values—at 0.88 and 9.98 ppm, respectively, in the case of the polymer-functionalized colloids—than the expected range of pure propanol, typically occurring at 0.96 ppm for ^1H -NMR and 10.28 ppm for ^{13}C -NMR [21]. The shift in resonance toward lower values suggest shielding of the nuclei of $-\text{CH}_3$ (*i.e.*, exposed to less magnetic field).

Further insight into the system dynamics can be gleaned from the fact that the T_2 -relaxation of propanol increased with increasing polymer concentration. Unlike T_1 , which represents the spin-lattice interaction, T_2 represents the strength of coupling between nuclear spins in spin-spin interaction. Such an increase in T_2 is consistent with the motion of propanol molecules becoming less restricted in higher polymer concentration, whereas at lower concentrations, their motion was much more restricted. In contrast, the T_2 -relaxation data of the H_2O molecules did not reveal a trend.

For particles in a PVP concentration of 0.07 g/mL, the T_2 value was the highest, indicating that water molecules were much more mobile within the system compared to denser environments—the residual H_2O molecules were not able to access the particle surface due

to exclusion by an adsorbed polymer layer, an effect that scaled with polymer concentration. Denser polymer adsorption onto ZnO particles entailed more limited access for water molecules to the particle surface.

From the perspective of the ^{13}C nuclei, the C of propanol displayed the strongest detectable response, as summarized in Fig. 6*a* and *b*. Although the spin-lattice (T_1) relaxation time increased with polymer concentration, the magnitude of change was very low, and possibly within the error bars. This result suggests that at low polymer concentrations, the propanol molecule has a preferred orientation for approaching the surface of particles; however, as the polymer concentration increased, the variation became so small that we did not observe any directionality on propanol interaction with ZnO surface. On the other hand, the spin-spin (T_2) characteristics showed a clear trend of increasing time with increasing concentration, consistent with the proton NMR data, and confirming the reduced mobility of propanol with polymer concentration.

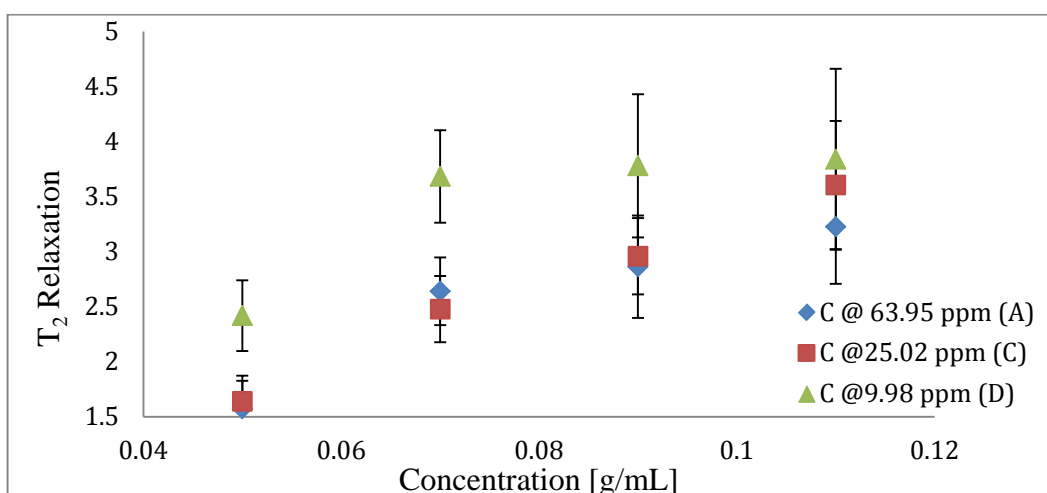
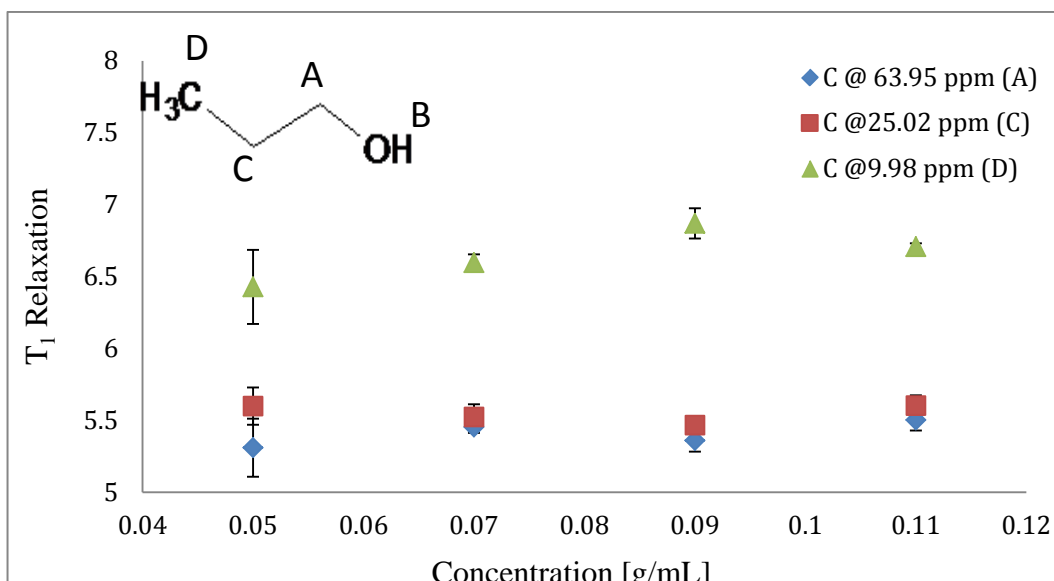


Figure 6. *a)* T_1 -relaxation characteristics for the PVP-functionalized ZnO, propanol, and deuterium oxide solution. The strongest detectable response came from the carbons of propanol, which are labeled in the inset figure; *b)* T_2 -relaxation characteristics for the PVP-functionalized ZnO, propanol, and deuterium oxide solution. The strongest detectable response came from the carbons of propanol, which are labeled in the inset figure.

Following the NMR-pulse sequence reported by Cosgrove, *et al.*, we estimated the polymer bound fraction, $\langle p \rangle$, from the maximum of first echo, A, and the maximum of the last echo, B, using Equation 2.^{13,20}

$$\langle p \rangle = 1 - B/A, \quad (\text{Eqn. 2})$$

The first pulse sequence, $90^\circ_x - \tau - 90^\circ_y - 2\tau$, where τ equals 10 microseconds, induced a response from protons throughout the entire system, *i.e.*, of both bound and non-bound polymers. This echo was followed by applying a second pulse sequence, $90^\circ_y - 2\tau - 180^\circ_y - 2\tau - 180^\circ_y - 2\tau$, to which only the protons of non-bound (*i.e.*, mobile) polymers respond. Polymer segments that were in close proximity to the surface of the nanoparticle were assumed to be bound polymers (*i.e.*, a partial bond between ZnO and pyrrolidone ring has formed). These segments exhibited the relatively low mobility of that in a solid, in contrast to freely solvated polymer chains.

The extracted $\langle p \rangle$ revealed that only the 5% of the polymer was adsorbed onto the surface of the ZnO nanoparticles, when synthesized in a PVP concentration of 0.05 g/mL. In a PVP concentration of 0.11 g/mL, 40% of the polymer had adsorbed onto the ZnO surface. However, when the ZnO particles were synthesized in a 0.07 g/mL PVP concentration, 80% of the PVP had adsorbed onto the ZnO surface. From the bound fraction experiment, we can conclude that PVP adsorbs with different conformation on the surface of nanoparticles, when solution polymer concentration is varied.

Different sizes of particles offered different amounts of available surface area in the system. So, the bound fraction itself may not be so informative, if it is not normalized to the available surface area in the system. Figure 7 shows the bound fractions per surface area. Again we observed that at 0.07 g/mL polymer concentration, more polymer had still adsorbed onto the unit surface area. At 0.05 g/mL polymer concentration, the lowest amount of adsorption had occurred at the unit surface.

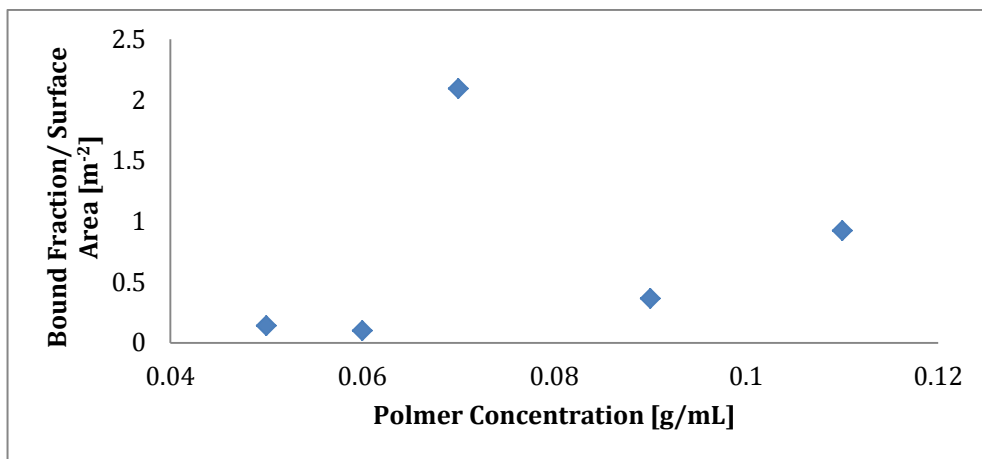


Figure 7. Bound fraction of functionalizing PVP per unit surface area

Time-domain NMR revealed that PVP was well-solvated by propanol at low PVP concentration, which is consistent with PVP adsorbing onto the ZnO surface in a tail-like conformation. In contrast, the poorer solvation by propanol at higher PVP concentrations correlated with more of the polymer adsorbing onto ZnO, indicating that the polymer conformation was more loop- or train-like.

Level of PVP passivation due to polymer conformation altered the photophysics of ZnO nanoparticles considerably and cause a higher level of near-band edge emissions at 0.07 and 0.11 g·mL⁻¹ PVP concentrations. The yellow luminescence at wavelength of 560 nm was associated with the deep trap states in ZnO band gap originating from the surface defects. The dangling head-to-tail conformation of bound PVP chains on ZnO surface led to a limited level of surface passivation and higher interaction of solvent molecules with surface defects. The UV emission was not observed since the emission centers were mostly on the surfaces of the nanoparticles. However, 0.07 and 0.11 g·mL⁻¹ PVP concentrations led to a more rigid PVP passivation layer on the surface and limiting the hydration shell radius. The loop and train conformation passivated coordinated with the defect states and reduced 1-propanol interaction with the emission centers. At 0.07 g·mL⁻¹ PVP concentration, the loop conformation could not completely quench the deep trap emissions however the defect state emission wavelength was shifted to 518 nm. 0.11 g·mL⁻¹ PVP concentration led to a complete quenching of the trap emissions.

Enhanced UV emission was obtained through higher levels of passivation due to polymer conformation on the nanoparticle surface however the proximity of polymer chain on the emission centers led to change in the excitation behavior of PVP as well. Since 310 nm UV emission of ZnO nanoparticles have a higher probability to excite the PVP chains, the excitation-emission contour of PVP shifted to lower excitation values.

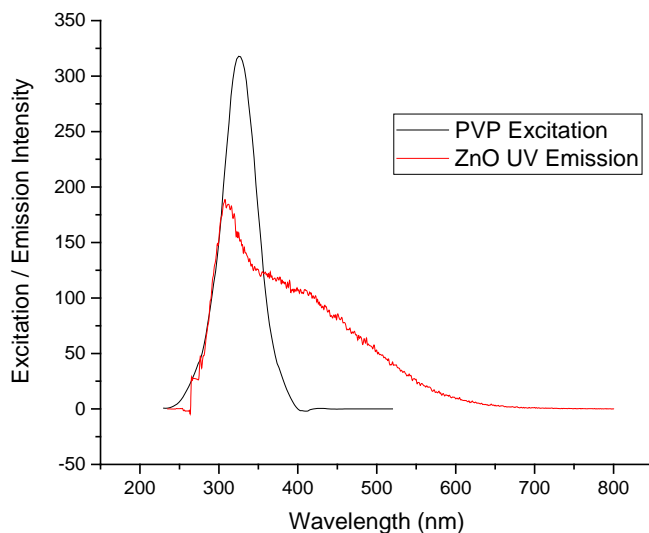


Figure 8. Excitation spectrum of PVP polymer and emission spectrum of ZnO nanoparticle with $0.11 \text{ g}\cdot\text{mL}^{-1}$

This occurrence partially diminished the UV emission of ZnO nanoparticles. The nature of energy transfer between PVP with train conformation on the surface and UV emission centers of ZnO nanoparticles remains to be elusive.

Conclusion

In this study, we have investigated the nature of PVP chain conformations on the surface of ZnO nanoparticles and their peculiar effects on the photophysics of ZnO nanoparticles. The strong UV emission of ZnO nanoparticles with PVP chains in train conformation revealed that the surface trap states are the main factor determining the photophysics of ZnO nanoparticles and can be engineered using different levels of PVP concentrations. Dynamic NMR was utilized to probe both bound polymer chains on the surface and complementarily

the solvent molecules interacting with the bound polymer chains and ZnO nanoparticle surface.

References

- (1) Hamad, I.; Al-Hanbali, O.; Hunter, A. C.; Rutt, K. J.; Andresen, T. L.; Moghimi, S. M., Distinct Polymer Architecture Mediates Switching of Complement Activation Pathways at the Nanosphere-Serum Interface: Implications for Stealth Nanoparticle Engineering. *ACS Nano* **2010**, *4*, 6629-6638.
- (2) Dutta, N.; Green, D., Nanoparticle Stability in Semidilute and Concentrated Polymer Solutions. *Langmuir* **2008**, *24*, 5260-5269.
- (3) Lupitskyy, R.; Motornov, M.; Minko, S., S, Single Nanoparticle Plasmonic Devices by the “Grafting to” Method. *Langmuir* **2008**, *24*, 8976-8980.
- (4) Tjong, S. C., Structural and Mechanical Properties of Polymer Nanocomposites. *Mater Sci Eng.* **2006**, *53*, 73-197.
- (5) Balazs, A. C.; Emrick T.; Russell T. P., Nanoparticle Polymer Composites: Where Two Small Worlds Meet. *Science* **2006**, *134*, 1107-1110.
- (6) Liu, J.; Gao, Y.; Cao, D.; Zhang, L.; Guo, Z., Nanoparticle Dispersion and Aggregation in Polymer Nanocomposites: Insights from Molecular Dynamics Simulation. *Langmuir* **2011**, *27*, 7926-7933.
- (7) Gacitua, W. A.; Ballerini, A. ; Zhang, J., Polymer Nanocomposites: Synthesis and Natural Fillers A Review. *Clencia y tecnologia* **2005**, *7*, 159-178.
- (8) Ibbett, R. N., NMR Spectroscopy of Polymers. In Ibbett, R. N., Ed. Chapman and Hall: Glasgow, Scotland, 1993.
- (9) van der Beek, G. P.; Cohen Stuart, M. A.; Cosgrove, T., Polymer Adsorption and Desorption Studies via ¹H-NMR Relaxation of the Solvent. *Langmuir* **1991**, *7*, 327-334.
- (10) Esumi, K.; Takamine, K.; Ono, M.; Osada, T.; Ichikawa, S., The Interaction of Poly(vinylpyrrolidone) and Solid Particles in Ethanol. *J. Colloid Interface Sci.* **1993**, *161*, 321-324.
- (11) Magritek, L., Introductory NMR and MRI: Video 07: Measuring T₁ and T₂ Relaxation. In YouTube: 2009.
- (12) Barnett, K. G.; Cosgrove, T.; Vincent, B.; Sissons, D. S.; Cohen Stuart, M. A., Measurement of the Polymer-Bound Fraction at the Solid-Liquid Interface by Pulsed Nuclear Magnetic Resonance. *Macromolecules* **1981**, *14*, (4), 1018-1020.
- (13) Cosgrove, T.; Barnett, K. G., Driven Equilibrium Solid and Liquid Spin-Echo NMR Sequences. *J. Mag. Reson.* **1981**, *43*, 15-20

- (14) Lin, K.-F.; Cheng, H.-M.; Hsu, H.-C.; Lin, L.-J.; Hsieh, W.-F., Band gap variation of size-controlled ZnO quantum dots synthesized by sol-gel method. *Chem. Phys. Lett.* **2005**, *409*, 208-211.
- (15) Pesika, N. S.; Hu, Z.; Stebe, K. J.; Searson, P. C., Quenching of Growth of ZnO Nanoparticles by Adsorption of Octanethiol. *J. Phys. Chem.* **2002**, *106*, 6985-6990.
- (16) Sesta, B.; Segre A. L.; D'Aprano A.; Proietti N., ¹H NMR, Surface Tension, Viscosity, and Volume Evidence of Micelle-Polymer Hydrophobic Interactions: LiPFN-PVP System. *J. Phys. Chem.* **1997**, *101*, 198-204.
- (17) Lipowsky, P.; Hedin, N.; Bill, J.; Hoffmann, R. C.; Ahniyaz, A.; Aldinger, F.; Bergstrom, L.; Controlling the Assembly of Nanocrystalline ZnO Films by a Transient Amorphous Phase in Solution, *J. Phys. Chem. C*, 2008, *112*, 5373-5383.
- (18) van Dijken, A.; Meulenkaamp, E. A.; Vanmaekelbergh, D.; Meijerink, A.; The luminescence of nanocrystalline ZnO particles: the mechanism of the ultraviolet and visible emission, *J. Lumin.*, **2000**, *87-89*, 454-456.
- (19) Guo, L.; Yang, S.; Synthesis and Characterization of Poly(vinylpyrrolidone)-Modified Zinc Oxide Nanoparticles, *Chem. Matter.*, **2000**, *12*, 2268-2274.
- (20) Barnett, K. G.; Cosgrove, T.; Vincent, B.; Sissons D. S.; Measurement of the Polymer-Bound Fraction at the Solid-Liquid Interface by Pulsed Nuclear Magnetic Resonance. *Macromolecules.* **1981**, *14*, 1018-1020.
- (21) SDBSWeb: <http://riodb01.ibase.aist.go.jp/sdbs/> (National Institute of Advanced Industrial Science and Technology, accessed on December 3, 2012).

VITA

Hasan Kurt was born on the 3rd of April, 1983 in Istanbul, Turkey. He graduated from Bayrampaşa Anatolian High School (Suat Terimer Anatolian High School) in 2001. He received his Bachelor of Science degree (major in Materials Science and Engineering and minor in Physics) in 2006 from Sabancı University, Istanbul. During his undergraduate studies, he was not restricted to core courses of Materials Science and Engineering. He also enrolled in various courses including Quantum Mechanics, Semiconductor Physics, Optoelectronics and Integrated Optics. He continued his education in Sabancı University and served as teaching assistant in various courses including Electrical, Optical and Magnetic Properties of Materials, Thermodynamics, Introduction to Probability.

He continued his PhD studies in Sabancı University, Istanbul starting from Fall 2010. He was awarded with TUBITAK BİDEB scholarship during his PhD studies. In parallel to the core courses, he also enrolled in courses including Nano-Optics, Organic Electronics, Surface Science and Advanced Electron Microscopy to further improve his research skills. Main research interests covered self-assembly of nanostructures, optically active nanomaterials, plasmonics, biosensors and photovoltaics.

He published and presented his research work in several journals and conferences, listed in the following pages.

List of Publications and Proceedings

1. H. Kurt, E. Alpaslan, B. Yildiz, C. W. Ow-Yang, "Impact of polyvinylpyrrolidone on the photophysics of ZnO nanocolloids", *manuscript in preparation*.
2. H. Kurt, M. Yuce, B. Hussain, H. Budak, "Upconverting and Downconverting Nanoparticle-based Aptasensor Model for Multiplex Detection", *manuscript in preparation*.
3. M. Yuce, H. Kurt, N. Ullah, H. Budak, "Surface Plasmon Resonance based aptamer selection against FGFR protein family", *manuscript in preparation*.
4. S. Khabbaz Abkenar, A. Tufani, G. Ince, H. Kurt, A. Turak, C.W. Ow-Yang, "Transfer Printing Gold Nanoparticle Arrays with Thermo-Sensitive Poly N-isopropylacrylamide (pNIPAAm)," *manuscript in preparation*.
5. H. Kurt & C. W. Ow-Yang, "Impedance Spectroscopy Analysis of the Photophysical Dynamics due to the Nanostructuring of Anode Interlayers in Organic Photovoltaic", *Physica Status Solidi A*, doi:10.1002/pssa.201600314, 2016
6. H. Kurt, M. Yuce, B. Hussain, H. Budak, "Dual-Excitation Upconverting Nanoparticle and Quantum Dot Aptasensor for Multiplexed Food Pathogen Detection", *Biosensors and Bioelectronics*, 81, 280-286, 2016
7. H. Kurt, J. Jia, Y. Shigesato, C. W. Ow-Yang, "Tuning Hole Charge Collection Efficiency in Polymer Photovoltaics by Optimizing the Work function of Indium Tin Oxide Electrodes with Solution-processed LiF Nanoparticles", *Journal of Materials Science: Materials in Electronics*, 26 (11), 9205-9212, 2015
8. M.Yuce, H. Kurt, VRRS. Mokkaapati, H. Budak, "Employment of nanomaterials in polymerase chain reaction: insight into the impacts and putative operating mechanisms of nano-addives in PCR", *RSC Advances*, 4 (69), 36800-36814, 2014
9. M. Yuce, H. Kurt, and H. Budak, "Characterization of a dual biotin tag for improved single stranded DNA production", *Analytical Methods*, 6 (2), 548-557, 2014
10. M.G. Eskin, H. Kurt, M.A. Gulgun, C.W. Ow-Yang," Effect of boron on processing and phosphorescence behavior of SrAl₄O₇ (SA₂) co-doped with Eu²⁺ and Dy³⁺ ", *Materials Research Society Fall 2010 Meeting*, Pittsburgh, Pennsylvania, USA: Materials Research Society, April 2011.

List of Conference Presentations

1. S. Khabbaz Abkenar, G. Ince, A. Tufani, H. Kurt, H.E. Baysal, C.W. Ow-Yang, "Transfer Printing Arrays of Gold Plasmonic Nanoparticles by Thermo-Sensitive pNIPAAm for Integration into Organic Photovoltaics", Materials Research Society Spring 2016 Meeting, Phoenix, Arizona, USA: Materials Research Society, March 28-April 1, 2016.
2. B. Hussain, H. Kurt, H. Budak, M. Yuce, "Novel Aptamer Coupled Fluorescent Nanoparticle Assay for Multiplexed Food Pathogen Detection", International Conference of Biochemistry, Biotechnology and Biomaterials (ICBBB-2016), Faisalabad, Pakistan, February 22-24, 2016.
3. M. Yuce, H. Kurt, B. Hussain, H. Budak, "Surface Functionalization of Up-converting Nanoparticles with Aptamers for Sensing Purposes", 1st Conference and Spring School on Properties, Design and Applications of Up-converting Nanomaterials, Wroclaw, Poland, May 23-27, 2016.
4. C. W. Ow-Yang, H. Kurt, J. Jia, Y. Shigesato, "Engineering the ITO anode interface in organic photovoltaics for improving charge carrier extraction", 9th International Symposium on Transparent Oxide and Related Materials for Electronics and Optics (TOEO-9), Tskubua, Japan, October 19-21, 2015.
5. M. Yuce, N. Ullah, H. Kurt, H. Budak, "Generation of Aptamers for Structurally Similar Protein Markers", International Conference on Chemical and Biochemical Engineering, Paris, France, July 20-22, 2015.
6. C. W. Ow-Yang, H. Kurt, J. Jia, Y. Shigesato, "Tuning Charge Collection Efficiency at the Transparent Conductive Electrode in Polymer Photovoltaics with Solution-Processed LiF", Solid State Ionics (SSI-20) conference, Keystone, Colorado, USA, June 14-19, 2015.
7. M. Yuce, N. Ullah, H. Kurt, H. Budak, "Surface Plasmon Resonance based Real Time Aptamer Selection", 2nd International Congress on Biosensors, Izmir, Turkey June 10-12, 2015.
8. N. Ullah, H. Kurt, M. Yuce, H. Budak, "Generation of Aptamers for Disease Biomarkers using Different Selection Strategies", Antalya, Turkey, February 22-26, 2015.
9. C. W. Ow-Yang, H. Kurt, J. Jia, Y. Shigesato, "Solution Processed Interlayers for Tunable Organic Photovoltaics Performance", Molecular Chemistry International Symposium, Istanbul, Turkey, December 19, 2014.
10. C. W. Ow-Yang, H. Kurt, J. Jia, Y. Shigesato, "Work function engineering of transparent conductive electrodes at the nanoscale", TCM 2014, 5th International Symposium on Transparent Conductive Materials on in Chania, Crete, Greece, October 12-17, 2014.

11. E. Uysal, M. Yuce, H. Kurt, "Impacts of carbon nanotubes on biochemical reactions: insight into interaction between carbon nanotubes and DNA polymerase enzyme", 16th European Congress on Biotechnology, Edinburgh, United Kingdom, July 13-16, 2014.
12. E. Uysal, M. Yuce, H. Kurt, H. Budak, "Impact of Carbon Nanotubes on Biochemical Reactions: Insight into interaction between Carbon Nanotubes and DNA polymerase enzyme", 10th Nanoscience and Nanotechnology Conference (Nano-TR10), Istanbul, Turkey, June 17-21, 2014.
13. E. Alpaslan, H. Kurt, B. Yildiz, C.W. Ow-Yang, "Deducing the Role of Functionalizing Macromolecules in the Nucleation of Colloidal Nanoparticles, MACAN CapStone_meeting; Kibbutz HaGoshrim, Israel, March 24-26, 2013.
14. H. Kurt, E. Alpaslan, C. Ow-Yang, "PVP as the Director of PVP-Functionalized ZnO Colloidal Nanoparticle Formation", Nano-TR8 conference, Ankara, Turkey, June 25-29, 2012.
15. E. Alpaslan, H. Kurt, B. Yildiz, C. W. Ow-Yang, "Deducing Polymer Functionalization of ZnO Colloidal Nanoparticles by Dynamic NMR Spectroscopy", Nano-TR8 conference, Ankara, Turkey; June 25-29, 2012.
16. E. Alpaslan, H. Kurt, B. Yildiz, C.W. Ow-Yang, "¹H NMR relaxation study of poly-vinyl pyrrolidone adsorption in zinc oxide colloidal dispersions", American Chemical Society 2012 Spring Meeting; San Diego, California, USA, March 25-29, 2012.
17. M.G. Eskin, H. Kurt, M.A. Gulgun, C. W. Ow-Yang, "The Effect of Boron on Processing and Phosphorescence Behavior of SrAl₄O₇ (SA₂) Co-doped with Eu²⁺ and Dy³⁺", Materials Research Society 2010 Fall Meeting; Boston, Massachusetts, USA; November 29-December 2, 2010.
18. H. Kurt, Y. Fatoğlu, H. Cıngıl, C. Öztürk, and C.W. Ow-Yang, "Synthesis and Characterization of PVP-capped ZnO nanocrystals," 4th National Nanoscience and Nanotechnology Conference, Istanbul, Turkey, 9-13th June 2008.
19. F. Uyar, A. Kamer, E.B. Gülsöy, H. Kurt, C. Öztürk, C.W. Ow-Yang, "Morphology of Colloidal ZnO Nanoparticles," Materials Research Society 2006 Spring Meeting, in San Francisco, California, USA, April 2006.